Delft University of Technology

MSc Biomedical Engineering
Master Thesis

Soft-tissue deformation and the potential of skin markers to facilitate accurate navigation in percutaneous renal ablation

---

MARLEIN VOGELS *(4532090)*

Supervisors TU Delft:
PROF. DR. J. DANKELMAN
PROF. DR. B. HENDRIKS

Supervisors Philips:
MSC R. WEIJERS
MSC T. VUURBERG

To be defended publicly: July 3, 2023 at 10:45

Final version: June 16, 2022

PREFACE

Hereby I present to you my master's thesis, the final chapter of my MSc program in Biomedical Engineering and of my time as a student at Delft University of Technology (TU Delft).

Over the past decades, the incidence of small Renall Cell Carcinomas (RCCs) has increased steadily, leading to a growing demand for less invasive nephron sparing treatments with suitable navigation strategies. Therefore, this thesis focuses on the soft-tissue deformation of both the kidney and the skin during needle insertion to explore the potential of skin markers to be used in combination with a cone-beam computational tomography (CBCT)-based navigation system in percutaneous renal ablation (PRA).

This graduation research was conducted in collaboration with the Biomedical Engineering department at TU Delft and the Mobile Surgery Advanced Development (MoS AD) group, part of the Image-Guided Therapy Systems department at Philips Healthcare in Best, The Netherlands.

I would like to sincerely thank my supervisors Prof. dr. J. Dankelman and Prof. dr. B. Hendriks for their superb guidance and insightful feedback during my project. The circumstances of the second half of my internship were unusual and challenging at times, on both a professional and personal level. Your support helped me to keep confidence in the successful completion of my project. Thank you!

Secondly, I especially want to thank to MSc. R. Weijers for giving me the opportunity to perform my graduation internship in Philips' innovative MoS AD group, her daily supervision and eagerness to support me wherever possible. Rozemarijn, I truly enjoyed our meetings and coffee chats and your feedback has helped me tremendously. Of course, special thanks go to MSc. T. Vuurberg for taking over Rozemarijn's role as daily supervisor so effortlessly in such a challenging time and his amazing assistance before, during and after my experiment. Also, I would like to express my gratitude to dr. B. Feddes for our weekly meetings and his feedback on my literature research.

Thirdly, I would like to express my gratitude to all medical experts who have participated in the brainstorms and have contributed to the development and validation of my porcine kidney model. And of course, I would like to thank the technical experts who have contributed to the foundation, preparation and execution of my experiment.

I would also like to thank my family and friends for their unwavering support, not only during my master thesis, but during my entire time in Delft. Especially Floor, Koen, Saskia, Joost and Sebas, I could not have done this without you.

And last but not least, I want to thank my grandmother for letting me be her "kamerbewoner" during my days in Best.

Enjoy reading!

Marlein Vogels
Delft, June 5, 2023

Abstract

Purpose: In percutaneous renal ablation (PRA), reaching the target accurately is challenging due to target motion and limited real-time visualization of the target, requiring a suitable navigation strategy. In the context of this thesis research, skin markers are used in combination with an the Azurion C-arm system (Philips Healthcare, Best, The Netherlands), an image-guided therapy system, equipped with ClarifEye (Philips Healthcare, Best, The Netherlands), an Augmented Reality (AR) surgical navigation system. The skin markers are tracked by ClarifEye, virtually representing the position of the patient. This thesis aims to explore if skin markers can facilitate sufficiently accurate navigation in PRA by investigating the skin marker motion (SMM) and kidney tumor marker motion (TMM) during needle insertion, considering the insertion speed (IS) and level of perirenal fat (LPF).
Methods: An ex-vivo porcine kidney model, with simulated skin, tumors and perirenal fat was developed and validated. A skin marker model was constructed on the model. Consequently, 60 robotic-assisted needle insertions were planned with ClarifEye (Philips Healthcare, Best, The Netherlands) navigation and performed on 8 kidney models (4 with low LPF (LLPF), 4 with high LPF (HLPF)), targeting 20 tumors at varying ISs: continuous insertions of 2.5 mm/s, 75 mm/s and consecutive 5 mm increments of 10 mm/s. Cone beam computed tomography (CBCT)-scans were made before and after insertion to analyze SMM and TMM.
Results: The SMM (overall mean SMM = 0.16 mm, standard deviation (SD) = 0.14 mm) was smaller than the voxel-size (1D) of dViewX (dicom-viewer software, Philips Healthcare, Best, The Netherlands) (voxel-size 1D = 0.2425 mm), regardless of the direction of the SMM and regardless of the IS and LPF. The TMM values in the z-direction were predominantly negative. The IS and LPF did not impact the amount and direction of TMM.
Conclusion: Any local skin deformation caused by needle insertion resulted in negligible SMM. Although the skin markers do not account for the TMM caused by needle insertions, the median TMM values (1.2-1.9 mm) are still smaller than the minimally required clinical insertion accuracy of 3-5 mm. The acceptable TMM values, in combination with the negligible SMM values, imply that skin markers can be used to facilitate navigation in PRA.

Index Terms

Ablation, fiducial markers, interventional oncology, navigation, optical tracking, renal cell carcinoma, skin markers

CONTENTS

List of Figures

List of Tables

ABBREVIATIONS

AR	Augmented Reality
C	Centroid
CBCT	Cone Beam Computed Tomography
CT	Computed Tomography
EC	Experimental condition
ED	Euclidian distance
EU	Experimental unit
HLPF	High level of perirenal fat
HS	High speed
IC	Increments
IGT	Image-guided therapy
IO	Interventional oncology
IR	Interventional radiologist
IS	Insertion speed
LESS	Laparoendoscopic single site
LLPF	Low level of perirenal fat
LPF	Level of perirenal fat
LS	Low speed
MoS AD	Mobile Surgery Advanced Development
M/O	Mechanical/Optical
MRI	Magnetic Resonance Imaging
NTD	Needle-to-target disatance
PCNL	Percutaneous Nephrolithotomy
PNP	Percutaneous needle procedure
PRA	Percutaneous renal ablation
RCC	Renal cell carcinoma
RE	Registration error
RSS	Root sum of squares
SD	Standard deviation
SE	Standard error
SMM	Skin marker motion
TM	Tumor motion
TMM	Tumor marker motion
US	Ultrasound
VMZ	Voxel measurement in zoomed-in mode

I. Introduction

A. Rationale

Renal Cell Carcinoma (RCC) accounts for over 80% of all renal malignancies with a worldwide incidence of 431288 (Worldwide cancer statistics, 2020) [6, 19, 44, 46, 57] and is the most lethal urological malignancy with a mortality rate of 35-50% [13, 41, 42, 57]. Due to the increased detection of small, localised, early-stage RCCs [14, 19, 26, 28, 37, 44, 56, 57] (over 50% of the RCC detections are incidental [19, 57]), which can be curable [19, 46, 57], and recurrence rate of RCC [19, 44, 46, 57, 69], more resource efficient and less invasive (nephron sparing) treatments are required. Therefore, percutaneous renal ablation[1] (PRA) is applied more and more, as the best clinical outcomes of PRA are reported in tumors with a diameter smaller than 30 to 40 mm [18, 41, 46, 51]. Compared to open and invasive surgery, minimally invasive procedures such as PRA[2] are known to lead to less post-operative pain, fewer (post-)operative major complications, shorter hospital stay, faster recovery times, less scarring, and sometimes to reduced operating time and saving costs [34]. However, a percutaneous needle procedure (PNP) such as PRA is not without challenges. First, it is essential that the needle is inserted so that the tumor is reached successfully, while preventing complications such as bleeding or touching critical structures. Consequently, ablating too much healthy tissue and missing any tumor tissue should be avoided [17]. However, target motion is known to be a dominant factor of disturbance in accurate targeting and successful PRA [35], especially since the target is not directly visible to the technician, as opposed to open surgical procedures such as an open radical nephrectomy. Although the general causes of target motion and motion management strategies are known and elaborated in Vogels [62], it was found that no (quantitative) research has been done investigating the tissue (both target and skin) motion due to needle insertion forces. To achieve accurate needle placement, accurate (real-time) visualization of the target is desired. However, no existing imaging modality (combination) overcomes all the challenges in PRA [49, 50, 58]. On the one hand, C-arm, Computed Tomography (CT) and Magnetic Resonance Imaging (MRI) provide high resolution images [22], but are limited in real-time visualization possibilities. Ultrasound (US), on the other hand, provides real-time visualization, but lacks image quality and is observer-dependent [60]. The limited high resolution real-time visualization possibilities of the target (and surrounding critical structures) in combination with the target motion require a suitable navigation strategy[3], overcoming the challenges in PRA[4]. Multiple navigation strategies (for PRA) have potential to be implemented in clinical practice [62]. However, it was found that, in order to determine the suitability of a navigation method for PRA, fundamental research about the tissue motion due to needle insertion is desired [62]. Furthermore, if an external marker model is used to track the position of the patient, the relation between the target motion and motion of the marker model is desired [62].

Several studies have used external (skin) markers to track patient and/or probe motion. Hata et al. [24] and Tokuda et al. [55] used external markers to track motion of a patient-mounted needle guide in PRA. Abhilash and Chauhan [7] used optical skin markers to track the patient's motion caused by breathing. However, no insertions were performed in this study. Li et al. [31] used external optical trackers to track the motion of the US probe. Müller et al. [36] used optical trackers to facilitate CT- and iPad- image fusion in Percutaneous Nephrolithotomy (PCNL). One commercially available navigation system (CAS-One IR: CAScination AG, Bern, Switserland) uses skin markers to track patient motion in percutaneous tumor ablation and has shown to increase the lateral insertion accuracy in liver tumors in a liver phantom [21, 63]. However, no studies have been published about the usage of this/similar navigation system(s) and the usage of skin markers in PRA. Furthermore, needle insertions are known to cause skin deformation [43], which may result in displacement of the skin markers without changes in the position of the patient. However, none of the studies have investigated the relation between needle insertions and the skin marker motion (SMM). It is known that multiple variables impact skin deformation during needle insertion, which may lead to SMM, and tumor motion (TM), of which an example is demonstrated in Figure 1. Although breathing motion is known to be the dominant factor of target motion [40], the breathing condition of the patient can be controlled by the physician by inducing an apnea or performing insertions at a fixed point in the breathing cycle [10, 40, 62, 68]. Furthermore, needle insertion speed (IS) is known to be related to the needle insertion forces and insertion accuracy [65] and can be controlled by the physician. Although the relation between needle IS and soft-tissue deformation has been identified [61, 64] and Dedong et al. [17] showed that a higher IS generally leads to less soft-tissue deformation, no research specifically exploring the relationship between needle IS and renal TM has been performed. Furthermore, perirenal fat is assumed to have a mobilizing effect on the kidney, causing TM in patients with a greater amount of perirenal fat. However, no research exploring this relationship has been performed.

[1] Please refer to Vogels (2023) [62] for an elaborated overview of the working mechanisms and types of thermal ablation

[2] Ablation is usually applied percutaneously [46]

[3] In this thesis, *navigation strategy* is defined as: "any method used to assist/aid in safely reaching the target(s) and/or remaining the needle/probe in place, thus contributing to the accuracy of the performed procedure"

[4] An overview of the currently used navigation methods in renal PNPs (also specifically PRA) is provided by Vogels (2023) [62]

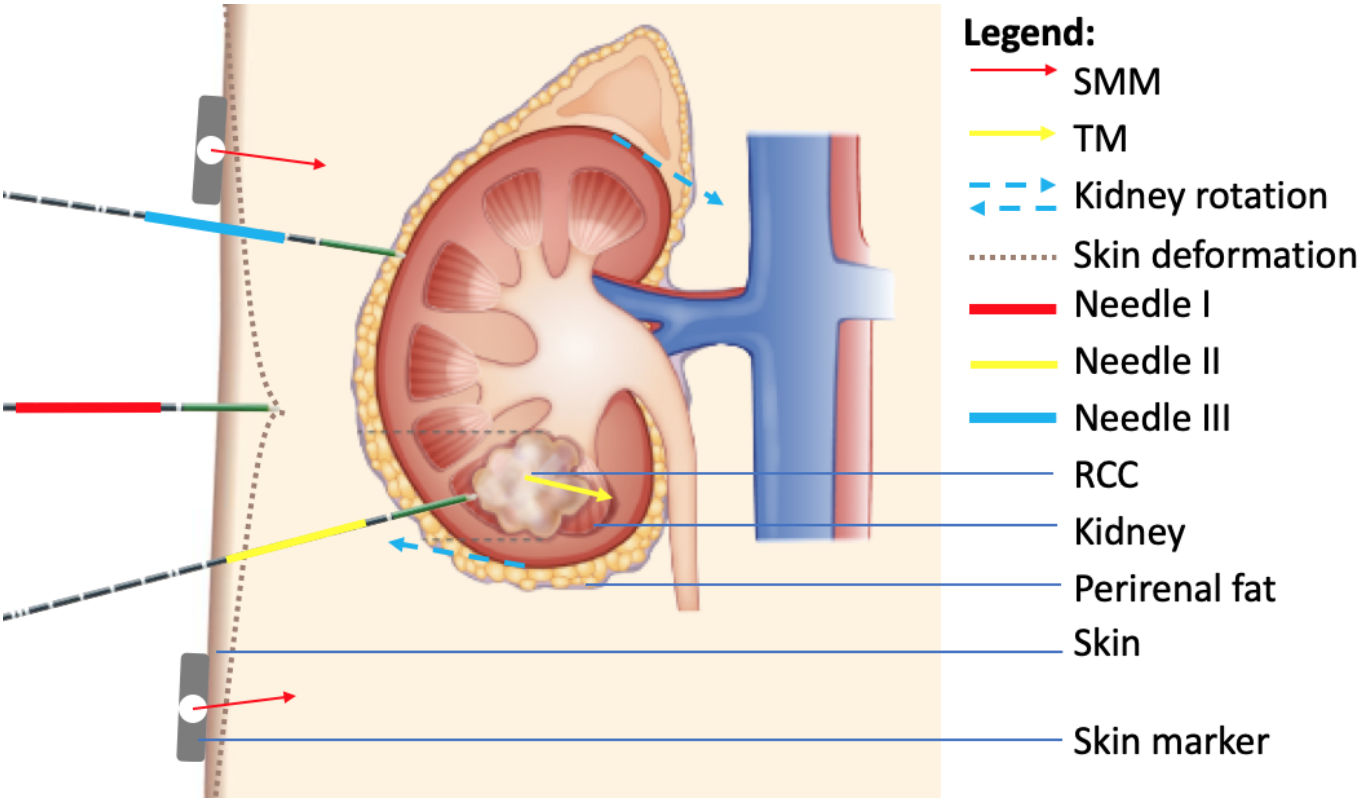

Fig. 1: A schematic example of how needle insertions may cause SMM, caused by the skin deformation, and TM. The shape of the skin deformation is based on the cone model for tissue deformation [17]. The color of the probes corresponds with the resulting motion and, if applicable, rotation. Furthermore, the possible TM caused by Needle I and II, as well as the possible SMM caused by Needle II and III is disregarded in this sketch.

B. Research questions

This thesis is aimed at exploring the motion of both the skin marker model and kidney tumor during needle insertion, considering the IS and amount of perirenal fat, to evaluate the potential of skin markers to be used in combination with a navigation system in PRA. Therefore, the overarching research question of this thesis is: *Can skin markers be used to facilitate accurate navigation in percutaneous renal ablation?*

To answer this research question three sets of sub-questions were defined:

1) Soft-tissue deformation during needle insertion:
   a) How does the kidney tumor move due to needle insertion?
   b) Is there an effect of needle insertion speed and amount of perirenal fat on the kidney tumor motion?
2) Skin marker model displacement during needle insertion:
   a) How does the centroid of the marker model move due to needle insertion?
   b) Is there an effect of needle insertion speed and amount of perirenal fat on the skin marker motion?
3) Relation between the displacement of the skin marker model and the displacement of the kidney tumor:
   a) Is there a relation between the displacement of the centroid of the skin marker model and the displacement of the kidney tumor, considering the insertion speed and amount of perirenal fat?

II. Navigation system with skin markers

As elaborated in Vogels [62], external (skin) markers can can be used to facilitate navigation in multiple ways. This section elaborates on how skin markers are used in combination with the image-guided therapy (IGT) system, of which two C-arm systems are explained, to facilitate navigation. This thesis research was performed on the Azurion C-arm system (Philips Healthcare, Best, The Netherlands) (see Figure 2). This is an IGT system with a fixed C-arm, facilitating two types of X-ray-imaging: fluoroscopy (a dynamic 2D X-ray image) and Cone Beam Computed Tomography (CBCT) (3D) [1]. Four cameras have been integrated in the detector of the Azurion C-arm system to facilitate navigation, which will be discussed in the next section [1]. Those cameras facilitate optical tracking and allow the image-to-image registration of real-time optical images to pre- and intra-operative CBCT-scans. As the cameras are integrated in the detector, the relation between the cameras and the detector is fixed. Therefore, the registration mechanism does not require any landmarks such as hybrid skin markers, which are visible in both the optical images and the CBCT-images. In the Zenition C-arm system (Philips Healthcare, Best, The Netherlands) (see Figure 2), on the other hand, no cameras are integrated in the detector to make a smaller, mobile C-arm [5]. A separate (mobile) unit with four cameras is required to register optical images to a pre-operative CBCT-image. As both the C-arm and the cameras are mobile, the relation between the detector in the C-arm and the cameras is not fixed, requiring hybrid skin markers[5] to perform the registration of the optical images to the CBCT-images.

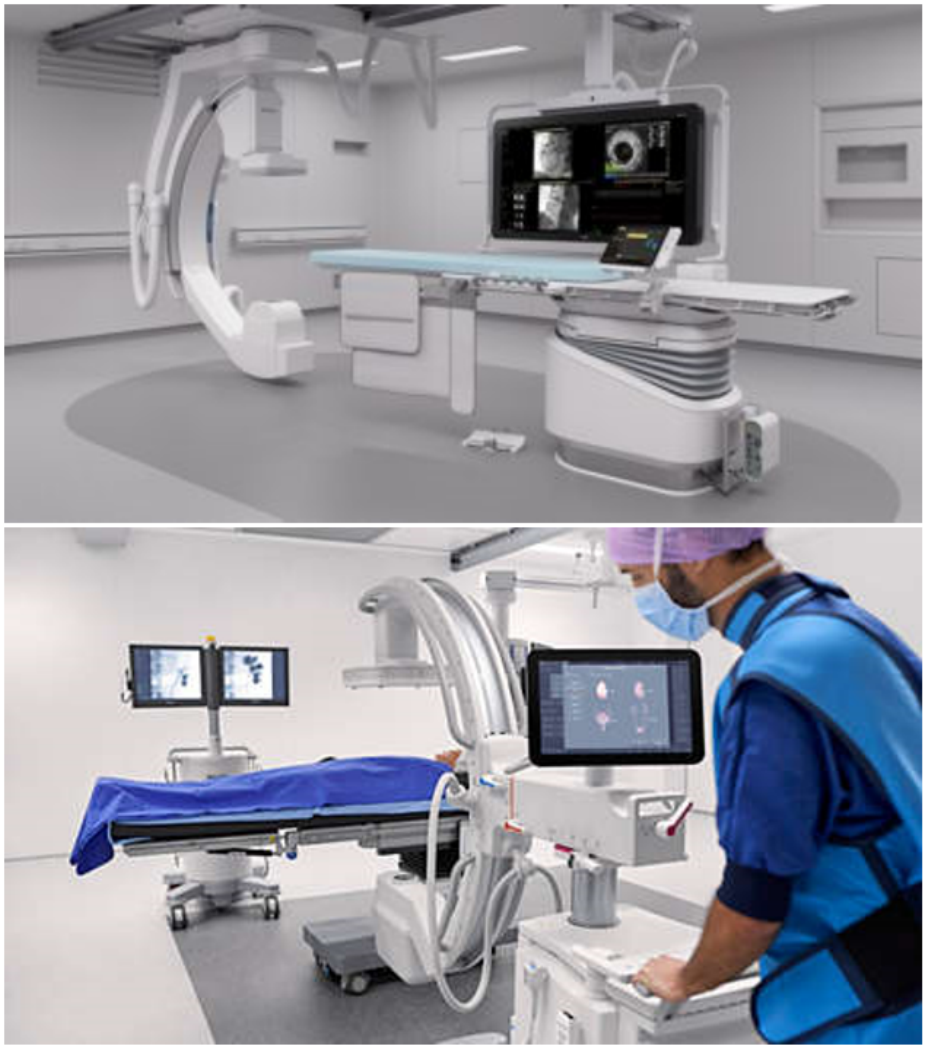

Fig. 2: Image-therapy systems: Top: the fixed Azurion C-arm system [1]. Four cameras are integrated in the detector. Bottom: the mobile Zenition C-arm system (on wheels that are not visible in the picture), which can be moved from room to room [5]. The camera unit is not displayed in the picture.

[5]the characteristics of skin markers are explained at the end of the section

The Azurion C-arm system is equipped with ClarifEye technology (Philips Healthcare, Best, The Netherlands): an Augmented Reality (AR) 3D surgical navigation application, which has been developed to facilitate navigation in spine procedures, such as spinal fusion [3]. By placing non-invasive, adhesive optical skin markers on a patient's skin, which are visible on the cameras and can be recognized by ClarifEye as skin markers, ClarifEye can construct a marker model, of which an example is presented in the close-up in Figure 3. This marker model virtually represents the position of the patient. Therefore, by optically tracking the position of the skin markers, ClarifEye can track the position and detect changes in the position of the patient. Consequently, ClarifEye can adjust the recommended navigation steps accordingly. Similarly, by making trackable instruments, for instance by applying a marker on a needle, which is recognized by ClarifEye and linked to the specific needle, the position of the needle can be tracked and the position of the needle in relation to the target can be determined and projected. Figure 3 presents a schematic application of skin markers used in combination with ClarifEye in a spinal fusion procedure.

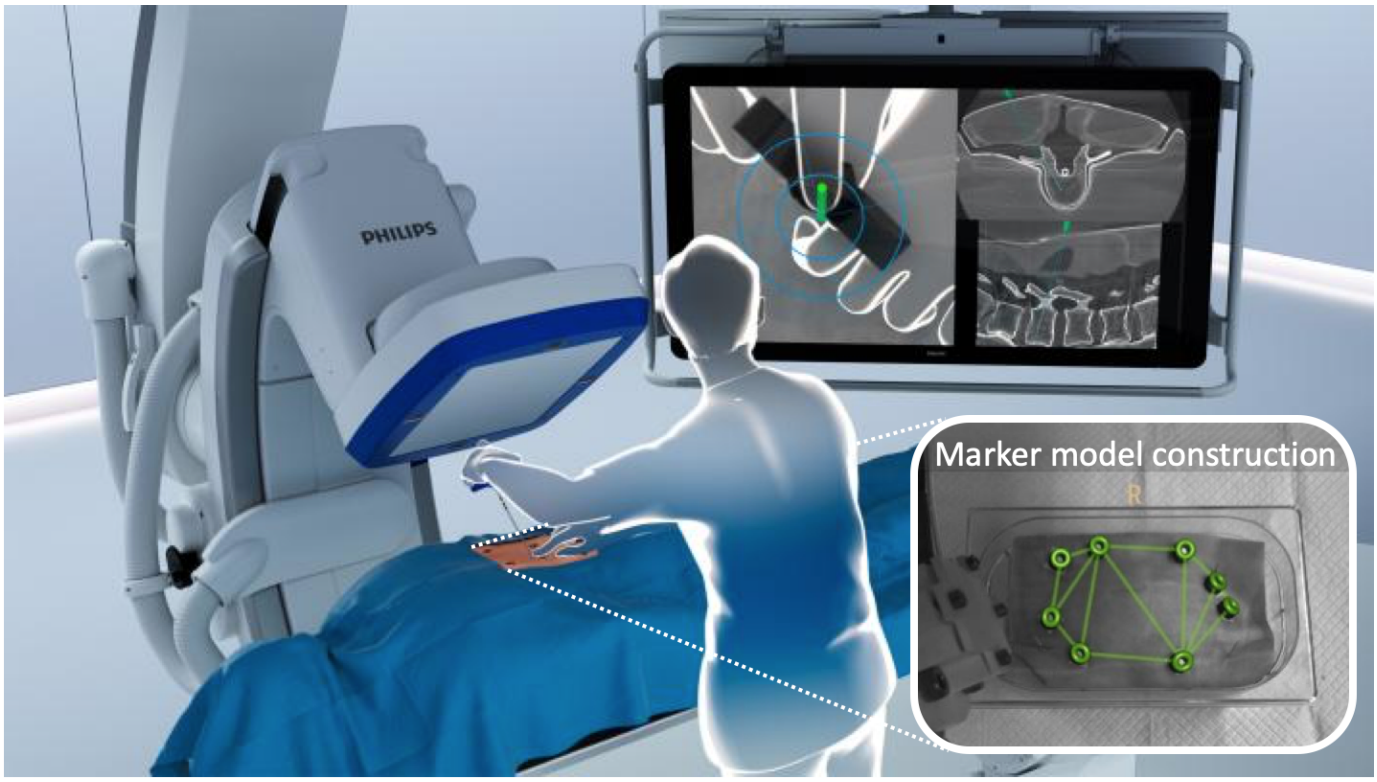

Fig. 3: A schematic example of the skin markers, the black fiducials attached on the patient's skin, used in combination with ClarifEye AR navigation [3]. The four cameras are visible on the blue edges of the flat detector. The needle is trackable and projected on the screen. The bulls eye assists the physician to position and align the needle in accordance with the planned needle path. The close-up presents a real example of a constructed marker model in ClarifEye, in the view of one of the four cameras.

There are multiple causes of patient motion or displacement, which are all recognized by ClarifEye as a change in the position of the marker model such as breathing and pronation/supination. During needle insertion, the patient's position does not change. However, local deformation of the skin occurs [43]. If this local deformation is detected by (one or multiple) skin markers, the local deformation will be falsely recognized by ClarifEye as a change in the patient's position, leading to less accurate and less reliable consequent navigation. In this study, hybrid skin markers are used, which are both trackable in ClarifEye and, due to their spherical radio-opaque center (diameter: 3.16 *mm*), visible on X-ray images, as the position of the skin markers will be obtained from Azurion's CBCT-scans. Furthermore, although the needle insertion phases of the experiment are elaborated in Section V-A4, it should be mentioned that in this study, the skin markers are only used to deduce the SMM from the CBCT-images and not to navigate.

III. Variables impacting SMM and TM

A. Sources of SMM and TM: idenfitication and hypotheses

This section elaborates on the factors impacting SMM and TM during needle insertion. Table II provides an overview of all identified variables hypothesized to impact either the SMM or the TM.

TABLE II: The identified variables impacting the SMM and TM during needle insertion, categorized per tissue type and aspect of the insertion.

SMM Factors		**TM Factors**	
Skin	- Elasticity - Thickness	**Tumor**	- Overall stiffness - Stiffness of capsule - Homogeneity - Size - Shape
Subcutaneous tissue layers	- Elasticity	**Tissue surrounding tumor**	- Elasticity - Level of perirenal fat (LPF)
Needle properties	- Tip shape - Thickness - Stiffness	**Needle properties**	- Tip shape - Thickness - Stiffness
Insertion characteristics	- Insertion speed - Insertion depth - Insertion angle - Insertion force - Continuous vs. increments	**Insertion characteristics**	- Insertion speed - Insertion depth - Insertion angle - Insertion force - Continuous vs. increments
Other	- Breathing condition - Gastrointestinal motion - Relaxing effect of anesthetics: sagging of abdomen - Distance between individual skin marker and insertion point	**Other**	- Breathing condition - Gastrointestinal motion - Relaxing effect of anesthetics: sagging of abdomen

Variables impacting SMM regard the properties of the skin, subcutaneous tissue layers, needle properties, insertion characteristics and motion of organs surrounding the kidney. Logically, a more elastic skin is expected to cause more local skin deformation, increasing the SMM. Similarly, more elastic subcutaneous tissue is expected to allow for more skin deformation during insertion, increasing the SMM. Additionally, attention must be drawn to the IS, as this speed can be controlled by the physician. Variables impacting TM regard the properties of the tumor, tissue surrounding the tumor, needle properties, insertion characteristics and motion of organs surrounding the kidney. A higher LPF is assumed to allow for more kidney mobilization, increasing the TM. Furthermore, attention must be drawn to the IS and tumor elasticity, as both variables impact the tumor's puncturing difficulty. However, when hypothetically linking the variables listed in Table II to the SMM or TM, it must be stressed that logical hypotheses cannot be formulated for all variables.

B. Variable identification: Brainstorms with experts

1) Introduction: As mentioned in Section I and Vogels (2023) [62], no studies have quantified the contribution of the factors identified in Section III-A to the SMM and TM during needle insertion. Furthermore, the exploratory pilot experiments conducted (see Appendix F) did not provide this information either. Therefore, additional sources of information about the factors impacting SMM and TM were desired to scope the experiment.

2) Method: Therefore, informative semi-structured brainstorms were performed with 10 experts: 3 interventional radiologists (IR), 2 urologists & 1 urology PhD candidate, 2 scientists in surgical navigation, 1 senior clinical scientist in interventional oncology (IO) and 1 biomedical engineer with IO experience. Additionally, a semi-structured brainstorm with the entire Mobile Surgery Advanced Development (MoS AD) team at Philips was conducted. All brainstorms were focused on the question: *Based on your experience, which variables are the main contributors to SMM and TM during needle insertion in PRA?* Prior to each brainstorm, the author (MV) gave a brief presentation about the aim of this thesis and provided the newest draft version of the kidney model, which will be elaborated in the next chapter, at the time of the brainstorm. After each brainstorm, the variables mentioned in the top three contributing factors impacting either SMM or TM were listed. Consequently, a ranking of the variables was made, considering the variable's "mention frequency" and "position in expert's top three". The value judgement of the top three of IRs was valued twice as high, because IRs have physically experienced the impact of the variables in clinical practice.

3) Results: Combining the results of the brainstorm according to the methodology described in Section III-B2 resulted in the following ranking of factors assumed to impact the SMM and/or TM:

1) **Breathing: known to induce both TM and SMM**
2) **IS: impacting TM, possibly impacting SMM**, and
   LPF: impacting TM
3) **Gastrointestinal motion**
4) **Other:** Insertion angle, insertion type (continuous vs. increments), needle type (tip, stiffness, size)

4) Discussion: Although the breathing induced SMM and TM was mentioned most frequently as dominant factor, IRs also mentioned that this factor is usually eliminated by inducing an apnea or timing the insertion at a certain point in the patient's breathing cycle. Consequently, based on this ranking, it is recommended to focus on the IS and LPF in the final experiment. Initially, four experts argued that an increase in the patient's BMI increases the TM. However, in a second brainstorm with two IRs, it appeared that this TM increase is related to the patient's LPF rather than the patient's BMI, which is assumed to act as a mobilizer for the kidney, causing TM due to kidney rotation. Therefore, the term BMI was not included in the ranking. When comparing the ranking to the variables identified in the literature research by Vogels (2023) [62], it was observed that the relation between the patient's LPF and TM was not mentioned in previous studies. Furthermore, although gastrointestinal motion causing kidney motion was mentioned in literature, gastrointestinal motion was only mentioned by non-medical experts. Lastly, no studies have been found comparing continuous insertion to insertion in increments, even though this factor is included in the expert's ranking. In several brainstorms, variables were identified, but the relationship with the SMM and/or TM remained unidentified or unknown, limiting the value of the variable identification. The brainstorms with IRs, on the other hand, resulted in more detailed variable identification and corresponding relations with SMM and/or TM, supporting the choice for higher judgement value for IR brainstorms. Second, although the ranking method is reproducible, the brainstorms were lead by one researcher, the author of this review (MV), which may have lead to bias in the conduction of the brainstorms. An additional independent researcher performing brainstorms with the same experts would increase the reliability of the ranking.

IV. KIDNEY PHANTOMS

This section presents the development and validation of the porcine kidney model used in the experiment.

A. Requirements & guidelines

The kidney model should be comprised of four main components, representing the:

- *Kidney:* the tumor motion is assumed to depend on the elasticity of the surrounding tissue;
- *Kidney tumor:* this is the target in a renal ablation procedure;
- *Perirenal fat:* this is the surrounding the kidney, providing space for the kidney to manoeuvre within the renal fascia;
- *Skin:* the skin deforms locally due to needle insertion and markers are positioned on the skin in the testing model.

In general, the main guideline to consider when designing the model is that the model must be suitable to target renal lesions while varying the IS and amount of LPF. The requirements and guidelines per component of the model are elaborated below. The skin markers and possible implantable fiducials are also components of the model. However, the model requirements and guidelines below are only focused on the organic components of the model. Furthermore, have already been designed. The requirements to satisfy and guidelines to consider are elaborated per model component. The mechanical, geometrical and anatomical requirements and guidelines are indicated in bold, because those requirements and guidelines are related to the occurrence and amount soft-tissue deformation, possibly impacting the SMM and/or TM.

1) Kidney: requirements & guidelines: The kidney in the model must satisfy the following requirements:

- ***Volume:*** The volume of the used kidney must be between 75% and 125% of the volume of the average human adult kidney.
- ***Collecting system:*** The collecting system of the kidney must be included in the kidney.
- *Practicality:* The kidney should be prepared within 3 hours, so that the entire model can be made within one day.
- *Costs:* The price of the kidney must be less than €10.

Additionally, the following guidelines must be considered:

- ***Geometry:*** The kidney in the model must resemble the geometry of a human adult kidney as much as possible.
- ***Elasticity:*** The Young's Modulus of the kidney must approach the Young's Modulus of a human adult kidney[6]. This guideline is included, because the stiffness of the tissue negatively correlates with the deformation of tissue under pressure.
- ***Securing:*** If possible, the ureter of the system must be secured to the edge of the model. According to Van Strijen (2023) [61], the kidney tends to rotate around the vascular pedicle when force is exerted on the kidney.
- If animal tissue is used, the tissue must be used within five days after purchase at the butcher.

2) Kidney tumor: requirements & guidelines: The kidney tumors in the model must satisfy the following requirements:

- ***Elasticity:*** The average stiffness of the tumor must be higher than the average stiffness of the kidney, because the average stiffness of RCCs is higher than the average stiffness of healthy kidney tissue [66][7].
- ***Hardness capsule:*** The ablation needle must be able to puncture the tumor capsule.
- *Marker insertion:* The tumor must allow the insertion of one metal fiducial marker without rupturing.
- *Tumor insertion:* The tumor must be insertable in the kidney through an insertion of 5 *mm*, because damage to the kidney must be avoided.
- *Costs:* The tumors must cost less than €1 per kidney model.

Additionally, the following guidelines must be considered:

- ***Size:*** The tumor should be smaller than 40 *mm* in diameter, because the best clinical outcomes of PRA are reported for lesions smaller than 40 *mm* in diameter.
- *Feeling:* The tumor must feel similar to an actual tumor in terms of hardness, because haptic feedback is essential during needle insertion in PNPs [53, 61].

3) Perirenal fat: requirements & guidelines: The perirenal fat in the model must satisfy the following requirements:

- *Costs:* The perirenal fat must cost less than €20 per model.
- *Time:* The perirenal fat must be preparable within one day (12 hours).

Additionally, the following guidelines must be considered:

- ***Elasticity:*** The stiffness of the tissue must approach the stiffness of acutal perirenal fat as much as possible, because the kidney displacement and therefore tumor motion depends on the elasticity of the perirenal fat. The average Young's Modulus of perirenal fat is unknown. Therefore, no quantitative requirement could be formulated.

[6]The average Young's modulus of the human kidney varies, depending on the health of the kidney tissue [45]. Therefore, no quantitative requirement is provided.

[7]No quantitative values are provided, because the stiffness of kidney tumors varies greatly, depending on the type (of RCC) and the patient [53, 66]

- ***Perirenal fat simulation:*** The material must be variable in volume or stiffness to simulate different BMI levels, to explore the hypothesized mobilizing effect of perirenal fat on the kidney.

4) Skin: requirements & guidelines: The skin in the model must satisfy the following requirements:

- *Costs:* The price of the skin must be less than €20 per procedure.
- *Time:* The skin must be producible within 1 day (12 hours).
- *Sustainability:* The skin must be reusable for at least 20 punctures.

Additionally, the following guidelines must be considered:

- ***Elasticity:*** The elasticity of the skin must resemble the elasticity of the human skin (from the back of the patient, right on top of the perirenal fat), because the skin motion due to the needle insertion forces must be representative for human skin motion caused by needle insertion forces.

B. Literature research: existing kidney models

Previously, kidney models have been developed for two purposes. First, kidney models are used in surgical training of surgeons. Second, kidney models are used for research purposes, for instance to test navigation tools to be used in renal PNPs or to test medical devices such as an ablation probe. In both applications, depending on the task or research question, materials are searched that mimic either the mechanical or optical properties of desired tissue. As this thesis is focused on the deformation and motion of both the skin and the tumor in the kidney, the mechanical properties of the model should approach the mechanical properties, such as elasticity, of each component of the model as much as possible. In this research, metal fiducials are used to visualize the target and track the position of points on the skin, which are visible on CBCT-scans. Therefore, the optical properties of the materials representing the tumor itself and skin are of secondary importance.

Table 4 provides a schematic overview of the models developed and/or used in previous studies. From this table, it can be seen that no model was comprised of each required component of the testing model for this study. Furthermore, only three studies [12, 27, 47] attempt to actually implement a lesion in their kidney model, of which no studies have validated the use of such simulated lesions. Therefore, it cannot be concluded from this literature review which material would be best suitable to represent kidney tumors in this thesis' kidney model. Four studies [16, 29, 47, 67] have incorporated a skin component in their phantom: a foam layer [16], porcine skin flap(s) [29, 67] and a silicone flap [47]. However, no studies have validated the elasticity of this skin flap, which is the most important criterion to consider in this thesis' kidney model. Although novel 3D printing techniques are emerging to produce soft-tissue phantoms like kidney phantoms, 3D printed phantoms (for instance proposed by Adams et al. (2016) [8] and Ristolainen et al. (2014) [47]) still have limited tissue mimicking properties [23]. Besides the small-scale produced phantoms, several commercially available kidney phantoms have been discussed by Hunt et al. (2013) [27]. Six commercially available phantoms (manufacturing companies: CIRS, Kyoto Kagaku, Blue Phantom) which can be used for renal biopsy training are presented, varying between $375 and $9500 in price per phantom. For percutaneous neprholithotomy (PCNL) procedures, the PCNL box (Encoris PCNL Kidney Training System Model with Case, Anatomy Warehouse, Evanston, IL, USA) can be used, which costs $1957 per box. To the author's (MV) knowledge, there are no commercially available phantoms for percutaneous renal ablation procedures with simulated kidney lesions.

Study	Priority: M/O*	Application	Kidney	Tissue surrounding kidney	Kidney tumor	Skin
Adams et al. (2016)	• M: E, σ_{UTS} • O: US attenuation	• Test medical devices • Simulate urological endoscopic procedures	1. Silicone elastomer **2. Agarose (4%)** 3. PDMS	X	X	X
Baumhauer (2008)	Not specified	Training model for percutaneous renal surgery	Porcine kidney in laparoscopic training unit	X	Agar nodules	X
Earp (2003)	Not specified	Training model for percutaneous renal surgery	Porcine kidney	Some perirenal fat was preserved	X	Foam layer + tape
Gomes-Fonseca et al. (2018)	O: US and radiographic visibility	Validate image-guided frameworks	Porcine kidney	Agar-based TMM (agar, glycerol, distilled water, flour, bleach)	X	X
Hunt et al. (2013)	• M: E • O: US attenuation, radiodensity	Renal biopsy phantom to train interventional radiology trainees	Gelatin phantom (with added formaldehyde and graphite powder)	Gelatin and formaldehyde	Cysts (not tumors): gelatin and formaldehyde	X
Jutzi et al. (2014)	• O: US visibility • Extra: performance trainee	PCNL training model (model in trainer box for LESS**)	Porcine kidney (with artificial calculi)	Porcine kin flap on both sides of kidney	X	Porcine skin (incl. subcutaneous tissue and muscle)
Hata et al. (2016)	M: simulate body motion	Test instrument-guide for cryo-ablation	Gelatin (12%)	X	X	X
Müller et al. (2012)	Not specified	Test augmented reality application with iPad for PCNL	Two porcine kidneys (still connected to each other)	Ballistic gelatin	X	X
Öpik et al. (2014)	• M: E, stress-strain curve • O: US attenuation	Validate robotic surgical instruments	Gelatin phantom (samples were compared to porcine kidney samples)	X	X	X
Ristolainen et al. (2014)	• M: questionnaire O: questionnaire	Training in interventional urology and radiology	**1. Gelatin phantom (with added formaldehyde and graphite powder)** X	**1. Gelatin and formaldehyde + extra gelatin on outside** 2. Gelatin phantom	**1. Cysts (not tumors): gelatin and formaldehyde** 2. Grapes, cucumber, tomato	**1. Silicone (EcoFlex 0030)** 2. Opaque plastic sheet
Strohmaier and Giese (2005)	Not specified	Training model for percutaneous renal procedures	Porcine kidney	Silicone base and silicone poured over kidneys	X	X
Tejo-Otero et al. (2022)	M: hardness, viscoelastic properties	Training	Gelatin (4% weight GelMA)	X	X	X
Zhang et al. (2008)	• O: US and radiographic visibility • Trainee performance	Intrarenal procedures training model	Porcine kidney	Some perirenal fat was preserved	X	Porcine skin flap: wrapped around kidney

Fig. 4: An overview of previously developed kidney phantoms and porcine kidney models: the intended application of the phantom and the composition of each phantom is provided per component (kidney, tissue surrounding kidney, kidney tumor, skin). If multiple models are used in one article, the best evaluated model is displayed in bold. *: M/O = Mechanical/Optical properties; **: LESS = Laparoendoscopic Single Site. [8, 9, 12, 16, 23, 24, 27, 29, 36, 47, 52, 54, 67]

C. Model selection

Based on the literature research and the experiences from the pilot experiments (see Appendix F), the most feasible material options were defined per component (kidney, kidney tumor, perirenal fat, skin). Consequently, Harris profiles were constructed to systematically evaluate the material options per component. A Harris profile is a structured method to systematically evaluate concept solutions. Although it is debatable whether a material choice in itself fits within the definition of a concept solution, the Harris profile is still considered a suitable method for the model selection, because a Harris profile allows to systematically evaluate the requirements defined in section IV-A. In this thesis research, Harris profiles were constructed per component instead of for a complete model concept, facilitating an in depth analysis of the benefits and limitations of each component option of the model instead of a general impression of the model as a whole. The practicality, reusability and costs criteria are subjective for all components. For each Harris profile, the requirements were ranked by relevance and importance. As a result, the Harris profile demonstrates the link between the requirements and the material options. Consequently, scores can be assigned and an intuitive decision can be made per material component. The quantitative scores assigned in a Harris profile are: '– -, -, + and ++', denoting a bad (- -), moderate (-), good (+) and excellent (+ +) score. Eventually, the testing model is comprised of a combination of the selected component materials.

TABLE III: Harris profile for material options for simulating the human kidney: the porcine kidney, a 3D printed kidney from agar gel and a gelatin phantom with the average human kidney stiffness.

Material	**Porcine kidney**				**3D printed agar kidney**				**Gelatin phantom**			
Criteria	**--**	**-**	**+**	**++**	**--**	**-**	**+**	**++**	**--**	**-**	**+**	**++**
Elasticity			■				■				■	
Anatomy			■			■				■		
Practicality			■		■	■				■		
Costs			■	■		■				■		

TABLE IV: Harris profile for the material options to simulate the kidney tumor: agar gel injected in the kidney, grapes, wine gums and a metal fiducial. *: the tumor insertion criterion could only be speculatively evaluated.

Material	**Agar**				**Grapes**				**Wine gums**				**Only metal fiducial**			
Criteria	**--**	**-**	**+**	**++**	**--**	**-**	**+**	**++**	**--**	**-**	**+**	**++**	**--**	**-**	**+**	**++**
Elasticity			■				■				■		■	■		
Marker insertion			■			■					■				■	■
*Tumor insertion**	■	■			■	■				■				■		
Size		■					■			■			■	■		
Costs		■					■				■				■	■

TABLE V: Harris profile for the material options to simulate the perirenal fat: agar gel, gelatin, a porcine skin flap with subcutaneous fat layer and a silicon mold for the kidney. *: the elasticity criterion, perirenal fat simulation criterion and practicality criterion could only be evaluated speculatively.

Material	**Agar**				**Gelatin**				**Porcine skin flap with subcutaneous fat layer**				**Silicon**			
Criteria	**--**	**-**	**+**	**++**	**--**	**-**	**+**	**++**	**--**	**-**	**+**	**++**	**--**	**-**	**+**	**++**
*Elasticity**		■					■			■					■	
*Perirenal fat simulation**			■				■							■		
*Practicality**		■				■					■	■	■	■		
Costs		■					■				■	■	■	■		

TABLE VI: Harris profile for the material options to simulate the human skin: a porcine skin flap and a silicone skin flap. *: the practicality criterion could only be evaluated speculatively.

Material	**Porcine skin flap**				**Silicone skin flap**			
Criteria	**--**	**-**	**+**	**++**	**--**	**-**	**+**	**++**
Elasticity		■				■		
*Practicality**			■			■		
Reusability			■				■	
Costs			■	■	■	■		

1) Kidney selection: The Elasticity criterion was evaluated as good (+) when at least one article incorporated in Table 4 mentioned the material as a good tissue mimicking material (TMM) in terms of Young's Modulus. The Anatomy criterion (which consists of the volume and collecting system requirements and the geometry and securing guidelines) was evaluated as (-) moderate if two or less of the included requirements/guidelines were satisfied. The good (+) score was awarded when three or all of the included requirements/guidelines were satisfied. The Practicality criterion (which consists of the time and complexity criterion and the animal tissue guideline) was evaluated as (–) if the kidney component takes more than three hours to prepare. In the case of the 3D printed agar kidney, an additional motivation for the bad (–) score is the fact that special 3D printers are required to produce the kidney. A moderate (-) score was awarded when the kidney takes more than three hours to prepare, but can be made without complex or expensive equipment. The good (+) score was awarded if the component satisfies the criterion. The Costs criterion was evaluated as (-) if the component costs between €10 − €50. The excellent (++) score was awarded when the kidney was free. That would be the case in this thesis research, as the kidneys at the butcher are seen as a by-product of the consumption meat industry. When evaluating the Harris profile in Figure III, the *porcine kidney* is the most promising kidney material option. Therefore, the eventual model included a porcine kidney.

2) Kidney tumor selection: The Elasticity criterion consists of the elasticity and hardness criteria and was evaluated as bad (–) when the needle cannot puncture the tumor. The good (+) score was awarded when the average stiffness of the tumor is higher than the average stiffness of the kidney and the capsule can be punctured by the ablation needle. This criterion was evaluated in practice by comparing the tumor material options with the porcine kidney by applying the Hardness scale (see Appendix C). The feeling guideline was not possible to take into consideration in the scoring yet, as the model was not punctured by an expert at that time, so no conclusions could be drawn in terms of feeling yet. The Marker insertion criterion was evaluated as moderate (-) when 50-70% of the structure of the tumor remained intact during marker insertion. The good (+) score was awarded when a marker could be inserted while keeping 70-99% of the structure of the tumor intact when inserting the metal fiducial. The excellent (++) score was awarded if no simulated tumor was punctured. The Tumor insertion criterion was evaluated as bad (–) when the tumor did not stay in place in the kidney after insertion or the kidney cannot be closed up after insertion of the tumors. While inserting agar tumors in a porcine kidney during a pilot experiment (Appendix F), the agar gel immediately oozed out of the kidney after injection. In the case of grapes, the kidney cannot be sufficiently closed after insertion through an incision due to the volume of the grapes, disabling representative kidney deformation during needle insertion. The moderate (-) score was awarded when the kidney was only punctured or an incision was made which could be glued after tumor insertion. The Size criterion was evaluated as moderate (-) as the lesions were < 0.5 *cm* in diameter. The good (+) score was awarded to lesions $0.5 - 2.5$ *cm* in diameter. The metal fiducial option was classified as bad (–) in size, because no lesion is present at all. The Cost criterion was evaluated as moderate (-) if the price of the tumors per kidney model is €1 - €10, the good (+) score was awarded when the tumor was $<$ €1, the excellent (++) score was awarded when the tumor was free. When evaluating the Harris profile in Figure IV, the *wine gums* is most promising kidney tumor material option. Therefore, the eventual model incorporated wine gums to simulate kidney tumors.

3) Perirenal fat selection: The Elasticity criterion was evaluated as moderate (-) when the material was assumed to be either too elastic or too stiff compared to actual perirenal fat, causing non-representative kidney rotation. As no data were found considering the stiffness of perirenal fat, this criterion is evaluated subjectively. In the pilot experiments with agar gel, despite following the protocol, the agar gel did neither solidify enough and the eventual solution was not homogeneous. The subcutaneous fat attached to the porcine skin flap is assumed to be stiffer than the actual perirenal fat, allowing for less kidney displacement. The gelatin is expected to have similar effect as the agar gel. The good (+) score was awarded when it was assumed to mimic the elasticity of perirenal fat. The perirenal fat simulation criterion was evaluated as moderate (-) when the material cannot completely surround the kidney. The good (+) score was awarded when the stiffness or volume of the material can be varied. In the case of porcine skin, the volume of the material (thickness of the subcutaneous fat layer) can be varied. The Practicality criterion was evaluated as bad (–) when the protocol to prepare the material cannot completely surround the kidney. The moderate (-) score was awarded when the solidifying process demands accurate timing and temperature monitoring. The excellent (++) score was awarded when no preparation steps are required. The Costs criterion was evaluated as bad (–) when the perirenal fat material costs >€30 and moderate (-) when the perirenal fat material costs €30 - €10. The good (+) score was awarded when the material costs <€10 and the excellent (++) score was awarded when the material is free. Similarly to the porcine kidney, the porcine skin is seen as a by-product from the consumption meat industry and is therefore free. When evaluating the Harris profile in Figure V, the *gelatin* is a more promising material option for the perirenal fat than the *porcine skin flap*, because the *gelatin* has a higher score for the most important critera. Therefore, the eventual model fixated the kidney in gelatin.

4) Skin selection: The Elasticity criterion was evaluated as moderate (-) when the material was stiffer than human back skin, as was experienced in the pilot experiments (Appendix F). The practicality criterion was evaluated as moderate (-) when the skin takes more than one hour to produce. The good (+) score was awarded when the material was ready for use. The

Reusability criterion was evaluated as good (+) when 20-30 punctures can be made in one skin flap. The Costs criterion was evaluated as bad (–) when the price of the skin is >€20 per skin flap. The excellent (++) score was awarded when the material was free. When evaluating the Harris profile in Figure VI, the *porcine skin flap* has the greatest potential to be used as skin mimicking material. Therefore, the final porcine kidney model included a porcine skin flap.

D. Final design & assumptions

Based on the Harris profiles (Tables III, IV, V, VI), the final design of the porcine kidney model was made, of which a schematic side- and topview, including the marker model, are provided in Figures 5 and 6. Specifics about the used materials, such as gelatin volume and tumor size, are provided in Appendix A-A. As respiratory induced kidney motion is usually eliminated during insertion (see Section III-B), any form of simulated breathing induced motion is disregarded in the kidney model. Furthermore, normally, the rigid structure of the spine may limit kidney motion. In this test set-up, the spine is disregarded and the plastic box is assumed to cause similar kidney motion restriction. Lastly, it is assumed that any displacements caused by forces unrelated to the experiment will not impact the relation between SMM and the TM. Therefore, no reference markers are required to re-calibrate the data.

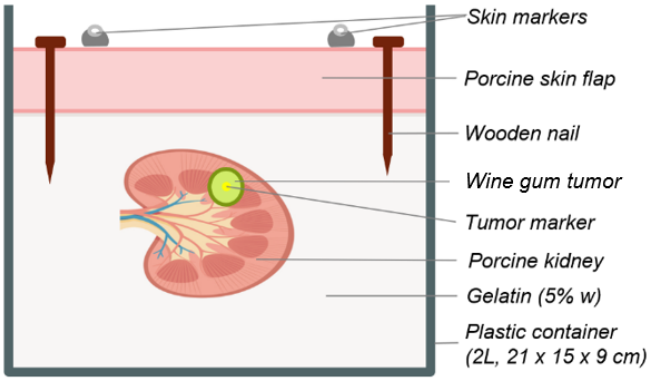

Fig. 5: Schematic sideview of the set-up. The amount and location of the simulated tumors in the experiments may differ from the test set-up figure.

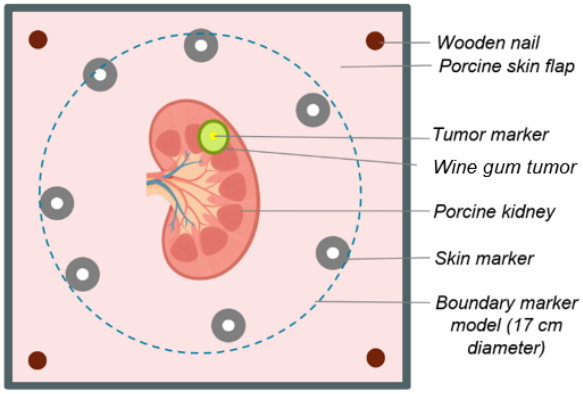

Fig. 6: Schematic topview of the set-up, including an example of the skin marker model. The amount and location of the simulated tumors and skin markers in the experiments may differ from the test set-up figure.

E. Model validation: questionnaire and physical validation

1) Method: First, a questionnaire was developed to evaluate the kidney model both per component (kidney, kidney tumor, perirenal fat, skin) and as a whole. The questions related to the usability of the model were based on the questionnaires from Hunt et al. (2013) [27] and Ristolainen et al. (2014) [47]. The statements 1-7 and 11-15 were evaluated on a 5-point Likert scale, where 5 was defined as the best possible approach to model the human kidney, including tumors, perirenal fat and skin. Statements 9-10 and 17 could be answered with 'yes' or 'no'. The questionnaire was evaluated by one urologist (physically), one fellow IR (via Teams video-call) and one IR (IR A, via e-mail). Prior to the theoretical validation, all experts received a brief presentation about the aim of this thesis and images with explanation of the model.

Second, one urologist and one IR (IR B)also physically validated the model by inserting a needle. Following the needle insertion, an additional semi-structured interview was conducted with the urologist to gain additional qualitative validation insight into the feeling and usability of the model. Furthermore, plain gelatin phantoms with gelatin concentrations of (with 2.5%, 5% and 10% weight, respectively) were presented to the urologist to determine the appropriate stiffness of the gelatin simulating the perirenal fat. The IR B also performed insertions on the model in a demonstration session. However, due to time restrictions, running the full questionnaire by the IR was not possible. As an alternative, an informative conversation with targeted questions focused on the tissue feeling during needle insertion was conducted during the demonstration.

2) Results: In Table VII, the results of the theoretical model validation are presented. The kidney model scores lowest on the perirenal fat simulation. All experts consider the model suitable for the experiment. The appropriate gelatin concentration was 5% weight. Therefore, the perirenal fat in the final kidney model was 5% weight. The urologist could distinguish all different tissue layers during needle insertion. The IR expert could only distinguish the kidney from the perirenal fat and the skin.

TABLE VII: Results of the model validation questionnaire, answered by one urologist, one fellow IR and one IR (IR A). Statements 1-8 and 11-16 were answered on a 5-point Likert scale, where 5 was defined as the best possible approach to model the human kidney. N.A.: not applicable

Question	**Results**			
General impression & Usability	**Urologist**	**Fellow IR**	**IR A**	**Average**
1. The size of the model is suitable for this experiment	5	4	4	4.3
2. The aesthetic features of the model are suitable for this experiment	5	N.A.	N.A.	-
3. The consistency of the model is similar to anatomical structures	4	N.A.	N.A.	-
4. The model is suitable for practicing gaining percutaneous renal access	4	4.5	5	4.5
Kidney: Porcine kidney				
5. The size of the kidney is similar to a human kidney	5	5	5	5
6. The stiffness of the kidney is similar to a human kidney	4	3.5	5	4.2
7. The anatomy of the kidney is similar to a human kidney	5	5	4	4.7
Kidney tumor: Wine gums				
8. The stiffness of the tumor sufficiently approaches the average stiffness of human kidney tumors	5	4	4	4.3
9. The stiffness of the tumor capsule is greater than the stiffness of the kidney	Yes	Yes	N.A.	-
10. Despite the wine gums being slightly smaller than the average abalated kidney tumor, the size of the tumor is sufficient for this experiment	Yes	Yes	Yes	Yes
Perirenal fat: Gelatin				
11. The stiffness of the gelatin is similar to the stiffness of perirenal fat	3	3.5	4	3.5
12. By varying the amount of gelatin underneath the kidney, a higher/lower level of perirenal fat can be simulated	3	4	4	3.7
13. The gelatin facilitates as a mobilizer for the kidney similar to perirenal fat	3	4	4	3.7
Skin: Porcine skin flap				
14. The stiffness of the skin approaches the stiffness of human skin	4	3	4	3.7
15. The preserved subcutaneous fat is of added value to simulate the tissue layers punctured by the ablation probe	4	4	5	4.3
Final statements				
16. The model is suitable for this experiment	4	4	5	4.3
17. The model can be reproduced	Yes	Yes	Yes	Yes

3) Discussion: First, the size and anatomy of the kidney are practically identical to a human kidney. Although the tissue properties of a porcine kidney are similar to the tissue properties of a human kidney [16, 67], according to both the urologist, fellow IR, and IR A, an ex-vivo porcine kidney is assumed to be slightly different in stiffness than an in-vivo kidney, explaining the scores of respectively 4 and 3.5. The urologist physically confirmed that the stiffness of the tumor approaches the average stiffness of human kidney tumors. However, according to both the urologist and IR B, it was challenging to feel the tumor in the model during insertion. However, the insertions were performed with a stiff bone marrow biopsy needle (Jamshidi) instead of an ablation needle, possibly explaining the limited haptic feedback. Furthermore, RCCs greatly differ in size, texture, shape, heterogeneity. However, only one type of tumor was simulated in the kidney model. The statements regarding the gelatin simulating the perirenal were awarded the lowest scores, because the homogeneity and stiffness greatly differ per patient [53]. Compared to the sometimes lumpy structure of perirenal fat, the gelatin solution is relatively homogeneous. The urologist argued that varying two extreme volumes of gelatin to simulate the LPF is feasible to proof the concept of the effect of the LPF on the TM, but it is challenging to directly translate the LPF in the model to the LPF of a patient. Similarly, according to the fellow IR, the stiffness of the human skin greatly differs per patient, making it challenging to find one suitable material to represent the average human skin. However, the IR A explained: "regarding the stiffness, porcine skin is the best approximation of human skin we can get so far". Generally, both the urologist, fellow IR and IR A acknowledge that this model is suitable for the intended experiment. The fellow IR explained: "Although the muscles are not incorporated in this model, all relevant anatomical components in the clinical situation of PRA were considered. All components have been combined in a well thought-out model, while considering the available resources, practicality and purpose of the model."

Due to time restrictions, only three participants were interviewed in for the validation of the model. Furthermore, the urologist is now employed by Philips. Therefore, any bias in the model validation cannot be excluded. Moreover, due to the fact that the fellow IR and IR A could only virtually validate the model, questions regarding the stiffness of each component were mostly based on previous experiences with kidney phantoms. Also, the interviews with the fellow IR and IR A were conducted after performing the experiment, making it impossible to incorporate any feedback to improve the model. Although IR B performed insertions on the kidney model, limited information on the validity of the model was obtained due to the limited time of the demonstration during which the insertions were performed.

V. Experiment: Methods

A. Study set-up:

To answer the research questions (see Section I-B), needle insertions were performed on an ex-vivo porcine kidney model in the Rami Nachabé lab (a non-clinical lab at Philips Medical Systems B.V., Best, The Netherlands) on the 19-20 of April 2023. In Section IV, the development and validation of the intended kidney model will be elaborated, including a schematic side- and topview of the kidney model (see Figure 5 and 6). In this section, the final design specifics related to the experiment will be discussed.

1) Porcine kidney model:: First, an ex-vivo porcine kidney was used (weighing approximately 200 grams, acquired at Ambachtelijke Slagerij Dennis van de Ven, Schijndel, The Netherlands) to simulate the human kidney, because porcine kidneys are most similar in size and texture, both elasticity and tissue feeling, to human tissue [16, 67]. The collecting system of the kidney was preserved to assure representative encapuslation of the to be inserted tumors. The renal capsule was also preserved, as puncturing the renal capsule is assumed to cause kidney displacement and therefore TM. Second, to simulate and explore tumor displacement during needle insertion, three approximately spherical wine gum tumors (average diameter: 8 *mm*) were inserted into the porcine kidney. Wine gum tumors are assumed suitable to simulate kidney tumors, as wine gums approximate the hardness of real tumor tissue, which is significantly harder than healthy kidney tissue [53, 61, 66]. The hardness superiority of the wine gums (from now on referred to as: tumors) was confirmed by a manual check, applying the Hardness scale, provided in Appendix C. To track the position of the tumor, a metal fiducial marker (1.6 *mm* in diameter) was inserted into the center of the tumor with a 16-G Jamshidi needle (ClarifEye Needle, Philips Healthcare, Best, The Netherlands), while avoiding tumor rupturing. As a result, the position of the tumor center can be deduced from X-ray/CBCT- images without using contrast fluid. The displacement of the tumor marker will be referred to as tumor marker motion (TMM). Each tumor was inserted through a lateral kidney incision (maximum width: 5 *mm*, depth: 10-20 *mm*) to preserve the kidney's ventral and dorsal surface. The three tumors were inserted in the superior, middle and inferior region of the renal cortex, as RCCs are cortical [39]. To enclose the tumors, the incisions were glued, while avoiding glue to stick to the tumors. Third, to represent the perirenal fat, the kidney was fixated in a gelatin gel (5% weight)[8], with a density of 1-1.5 on the hardness scale (Soft to normal tissue, Appendix C), approximating the hardness of the perirenal fat surrounding the kidney. Fourth, to simulate skin deformation and explore SMM during insertion, a porcine skin flap, including subcutaneous fat (acquired at Ambachtelijke Slagerij Dennis van de Ven, Schijndel, The Netherlands) of 3-4 *mm* in thickness and 21-16 *cm* in size was pressed over the fixated kidney and secured by wooden nails, resembling the human skin, serving as the basis for the skin marker model. The most elastic porcine skin flaps available were selected to best approximate the stiffness of in-vivo human skin. The porcine kidney model was tightly fitted in a plastic basket of 21x16x9 (length x width x height) *cm* in size. A detailed step by step preparation of the kidney model is provided in Appendix A.

2) Hybrid skin markers: To track the position of the kidney model and possibly detect skin deformations caused by the needle insertions, a marker model consisting of 8 spherical fiducial hybrid skin markers[9] (radio-opaque diameter of 3.16 mm) was constructed. A circular yet asymmetric configuration of the markers was pursued with a maximum diameter of 17 cm, defined as the maximal optimal resolution field of view in spine surgery in Nav4Mos study, fitting over the entire kidney surface (see Figure 6 and Figure 8).

3) Equipment: C-arm system, navigation software, KUKA robot and ablation probe: To gain information about the position of both the tumors and skin markers, the experiment was conducted in the Azurion C-arm system (Philips Healthcare, Best, The Netherlands). As elaborated in Section II, the Azurion C-arm system acquires 3D CBCT-images and is equipped with the desired ClarifEye navigation technology (Philips Healthcare, Best, The Netherlands): an AR surgical navigation system, which tracks the skin marker model to track the position of the patient [58]. The Azurion C-arm system was re-calibrated before the start of the experiment and the position[10] of the model in the system was validated by one supervisor. A robotic 7-degrees-of-freedom arm (LBR iiwa, KUKA GmbH, Germanny; referred to as KUKA) was used to perform insertions at predefined ISs, depths and direction and to position the ablation needle at the planned position and in the planned orientation. The used settings of KUKA will be elaborated below. Lastly, all insertions were performed with a 13-G ablation needle (Emprint™ Percutaneous, An- tennas - 25cm, Medtronic-Covidien, Minneapolis, United States). In Figure 7, an overview of the study set-up is provided. The experiment was performed at room temperature.

[8]Please refer to Appendix A for exact gelatin concentrations and volumes per model

[9]Minimally 6 markers are required to facilitate tracking, a safety margin of 2 markers was applied in case any marker had to be removed during

[10]The detector should be free to move around the model. The kidney model, including all skin markers, must be within the field of view of the detector.

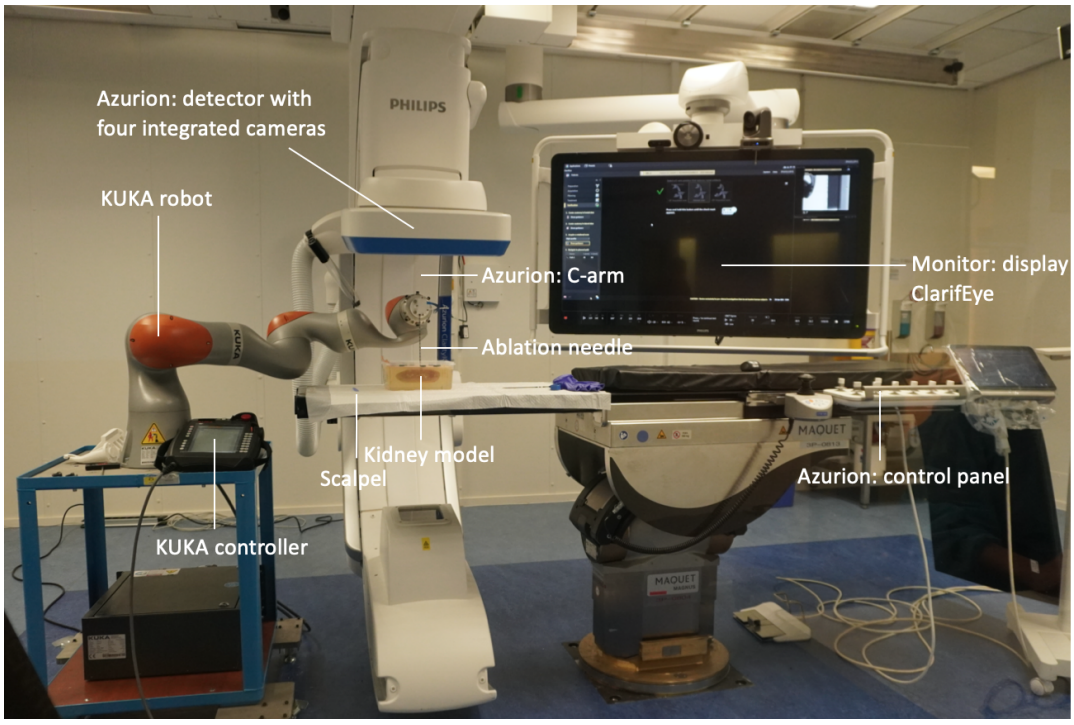

Fig. 7: An overview of the study set-up. The kidney model is taped onto an anti-slip cover, which is taped to the table of the Azurion system.

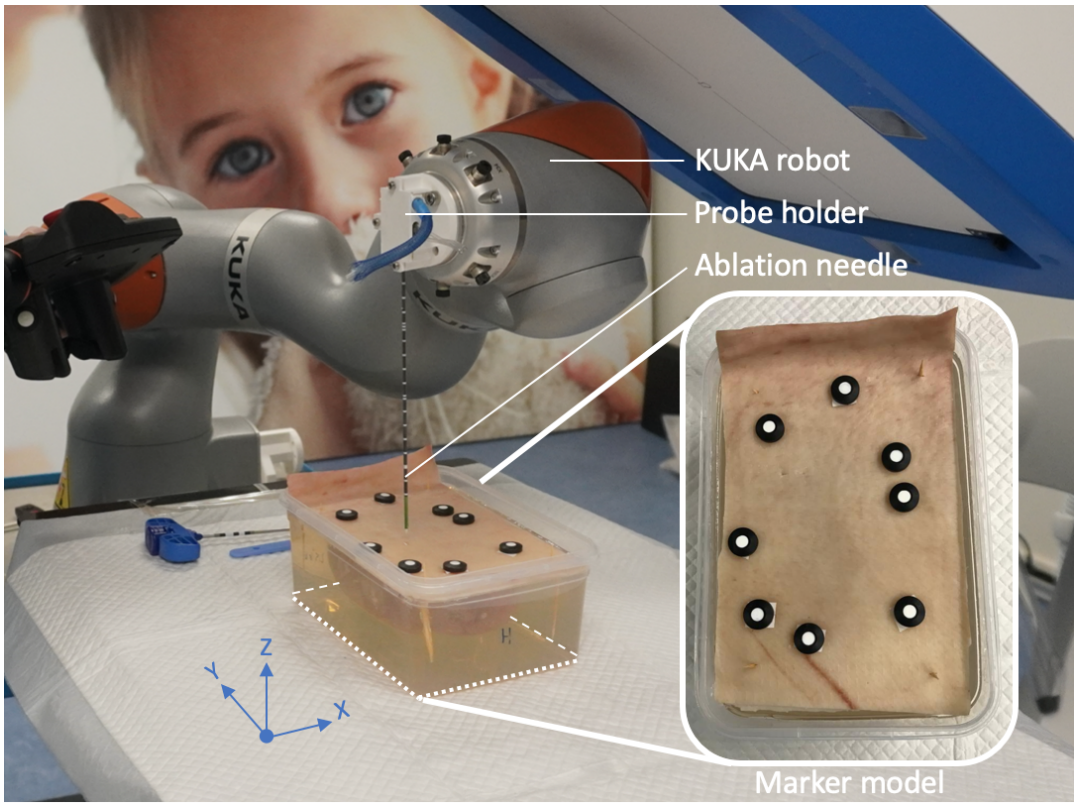

Fig. 8: A close-up of the study set-up, including a close-up picture of the marker model. The markers are taped to the porcine skin to prevent slipping. The coordinate system is based on the coordinate system from the y-plane of dViewX (the dicom-viewer software that was used for the CBCT-analysis).

4) Experimental design:

a) Experimental Conditions (ECs): This study is set-up to explore the SMM and TMM and to study the effect of IS and LPF, the two independent variables of the experiment, on the SMM and TMM. Therefore, respectively three and two levels per independent variable were defined, resulting in six ECs, displayed in Table VIII. To test the impact of IS on the SMM and TMM, insertions were performed at low speed (2.5 *mm/s*), high speed (75 *mm/s*) and 5 *mm* increments of 10 *mm/s*. The low IS level was defined based on Barua et al. [11], Van Dommele [58], Lin and Lan [32], Wang et al. [65], reporting ISs in PNPs in soft tissue of respectively (3 *mm/s*), (2.5 *mm/s*), (2 *mm/s*) and (1.5 *mm/s*). The high IS level was based on an estimation of the maximum feasible ISs that can be reached in clinical practice in especially manually performed PNPs. Insertion in increments was added as third IS level, because RCCs are often targeted in increments in clinical practice. Although the IS in the increment level was defined, this speed was never reached within the 5 *mm*, due to KUKA's limited acceleration. In all levels, the acceleration to reach the ISs was at KUKA's maximum level. To test the impact of the amount of perirenal fat on the SMM and TMM, insertions were performed in both low fat models, in which the kidney is fixated on a base of 100 *mL* of gelatin, and high fat models, in which the kidney is fixated on a base of 750 *mL* of gelatin, representing a professional athlete and an obese person [53] (see Figure 9 for a visual overview of the gelatin bases of a low level of perirenal fat (LLPF) and a high level of perirenal fat (HLPF) kidney model).

Fig. 9: Left: the gelatin base for an LLPF kidney model; right: the gelatin base for an HLPF kidney model. The gelatin fixating the sides and top of the kidney and the porcine skin are not displayed in this figure.

To estimate the experimental error (EE), a sample size of 10 was intended for each EC, resulting in a total of 60 experimental units (EU). Instead of randomly assigning the ECs to the 60 EUs, which was too labor-intensive and required an unworkable file-saving strategy, insertions were alternately (after targeting three lesions, the model was replaced) performed in the low fat and high fat models. Furthermore, each lesion was targeted once at low speed, at high speed and in increments in alternating order to cope with any possible SMM and/or TMM caused by previous insertions. Therefore, eight kidney models were prepared (four low fat models for EC_{11} - EC_{31} and four high fat models for EC_{12} - EC_{32}), each with three[11] tumors. Targeting multiple tumors per EC instead of performing many insertions on one lesion is assumed to increase the reliability of the results and prevent "over puncturing" of both the skin and the tumor. A list of the EUs is provided in Appendix B.

TABLE VIII: Condition Matrix displaying the six Experimental Conditions (ECs).

		LPF	
	$N_{total} = 60$	Low level of perirenal fat	High level of perirenal fat
Insertion speed	Low speed (2.5 *mm/s*)	EC_{11}	EC_{12}
	High speed (75 *mm/s*)	EC_{21}	EC_{22}
	Increments (5 *mm* at 10 *mm/s*)	EC_{31}	EC_{32}

b) Phases per EU: To identify the tumor's location, a CBCT-scan was made. Based on this CBCT-scan, the shortest possible needle trajectory was planned in ClarifEye (Philips Healthcare, Best, The Netherlands). Interference of the path with any previously performed insertions was avoided, as interference is assumed to influence the SMM and TMM due to a decrease in friction in previously formed paths. Furthermore, the insertion point was always within the area of the marker model, ensuring the insertion path is in the field of view. Lastly, the minimal distance between any skin marker and the insertion point was 2 *cm*, preventing obstruction of the insertion by the markers and allowing working space for making any incisions without touching the markers. For consequent insertions targeting the same lesion, the insertion depth must be: primary insertion depth $\pm$ 10 *mm*. The insertion angle was disregarded, as the KUKA robot limits the insertion angle range. After positioning the ablation needle at the planned entry point assisted by the bullseye view projected on the target in the ClarifEye application, an incision of 0-3 *mm* wide and 0-3 *mm* deep was made with a scalpel to prepare the insertion. Consequently, the ablation needle was aligned, matching the orientation with the planned path. A CBCT-scan was made to identify the initial position of both the skin markers and the tumor marker right before insertion. Consequently, the needle was inserted at the appropriate insertion depth and speed, considering the assigned EC. Lastly, a CBCT-scan was made after insertion/per increment to determine SMM

[11]A margin of two tumors was used in case a tumor insertion failed

and TMM. As mentioned in Section II, in this experiment, the skin markers are only used to determine the SMM based on the CBCT-scans.

B. Data collection and data exportation

The CBCT-scans were imported to dViewX (dicom-view software, Philips Healthcare, Best, The Netherlands). Consequently the center of the skin markers, tumor markers and the needle tip were manually selected in 'zoomed in mode'. The voxel measurement of the CBCT-scans is 0.485 *mm* (in the x-, y- and z-direction), the voxel measurement of the 'zoom in mode' (VMZ) of dViewX is 0.2425 *mm* (in the x-, y-, and z-direction), allowing selecting a position within the CBCT-voxel. dViewX provided Cartesian coordinates of the selected dViewX voxels with an accuracy of 0.01 *mm*. In most cases, the coordinates were obtained in the y-plane of dViewX. If the visibility of a tumor marker was limited, for instance due to overlap with the needle tip, an additional plane was used as a check. To account for any bias caused by manual selection, 5% of the scans were randomly selected using an online automated randomizer [4] to be re-analyzed in dViewX. Consequently, the difference in coordinates of the centroid of the marker model and the center of the tumor between the two analyses were compared. The maximal required difference was 0.2425 *mm* (corresponding with dViewX' VMZ) per dimension (x, y, z). All coordinates were inserted a run-table in Excel.

C. Data processing

As elaborated in Section I, the dependent variables in this experiment are the SMM and TM (in this study expressed in TMM). In this study, SMM was expressed in *the displacement vector of the centroid of the marker model*. For each CBCT-scan the centroid (C) of the obtained skin marker coordinates was calculated with:

$$C = \left(\frac{x_1 + ... + x_n}{n}, \frac{y_1 + ... + y_n}{n}, \frac{z_1 + ... + z_n}{n} \right),$$

where n stands for the total amount of segmented skin markers. Consequently, the SMM was calculated with:

$$SMM = [(x_{C_{end}} - x_{C_{start}}), (y_{C_{end}} - y_{C_{start}}), (z_{C_{end}} - z_{C_{start}})].$$

Lastly, the Euclidean distance (ED) of the SMM (SMM ED) was calculated. Similarly, the TMM and ED of the TMM (TMM ED) were calculated. To further explore the relationship between the SMM and TMM, the overlap (%) between the SMM and TMM were calculated in the x-, y- z-direction (and ED) via: $SMM_{direction(x/y/z/ED)}/TMM_{direction(x/y/z/ED)}$. Moreover, the offset, defined as the absolute discrepancy between the SMM and TMM was calculated via: $TMM_{direction(x/y/z/ED)} - SMM_{direction(x/y/z/ED)}$.

The following secondary outcomes were also obtained:

- the displacement of the needle tip in the x-, y-, and z-direction: $N = [(x_{N_{end}} - x_{N_{start}}), (y_{N_{end}} - y_{N_{start}}), (z_{N_{end}} - z_{N_{start}})]$. Although the insertion angle was disregarded while planning the needle trajectory, this needle tip displacement was still collected, as the insertion direction could influence the TMM
- the distance between the coordinates of the insertion point of the needle (in dViewX, the position of the needle tip before insertion is considered the insertion point) and the coordinates of the centroid before insertion: $d_{C-I} = \sqrt{(x_{Needle} - x_C)^2 + (y_{Needle} - y_C)^2 + (z_{Needle} - z_C)^2}$, was obtained, as the position of the marker model in relation to the insertion point may influence the sensitivity of the marker model to detect local skin deformation (see Section III)
- to examine the accuracy of the insertion, the needle to target distance (NTD) was obtained via: $NTD = \sqrt{(x_{Needle} - x_{tumor})^2 + (y_{Needle} - y_{tumor})^2 + (z_{Needle} - z_{tumor})^2}$
- the $\text{TMM}_{non-target}$ ED was obtained to compare the TMM ED and the $\text{TMM}_{non-target}$ ED.

All outcomes were calculated in the run-table in Excel.

D. Data analysis

The run-table was imported to SPSS for data-analysis. First, the mean, median, standard deviation (SD) and standard error (SE) were calculated for the SMM ED, TMM ED, TMM in the z-direction, and NTD per EC and combinations of ECs. Consequently, normality of the datasets was checked by plotting a histogram of the data and visually comparing the histogram with a standard bell curve. A two-way ANOVA (factorial design analysis of variance) was performed to assess the effect of each independent variable (IS and LPF) on one continuous dependent variable (SMM ED, TMM ED, TMM in the z-direction, and NTD) and to check possible interactions between the IS and LPF. The predetermined significance level was 0.05. To account for inequalities in sample size per EC, the two-way ANOVA in SPSS was set to add unweighted harmonic total averages to the ECs with smaller sample sizes. This option was pursued, as this is the most conservative way to cope with inequal sample sizes. Lastly, the correlations between the TMM ED and SMM ED, TMM ED and NTD, and TMM in the z-direction and NTD were obtained via bivariate correlation analysis. All figures displayed in this study were created in SPSS.

VI. Experiment: Results

A. Raw data

One sample (EU: 14) was excluded from data analysis, because the table of the Azurion system had moved during the insertion. Scatter plots of all measurements regarding SMM in the x-, y-, z-direction and ED (SMM_x, SMM_y, SMM_z, SMM ED) and TMM in the x-, y, z-direction and ED (TMM_x, TMM_y, TMM_z, TMM ED) are presented in Appendix D. A histogram of all measurements regarding SMM ED, TMM ED, TMM in the z-direction and NTD showed an almost normal distribution. By analyzing the manual selection control, of which the maximum difference in both the SMM ED and TMM ED was smaller than the VMZ, the manual selection was found sufficiently accurate.

B. Processed data

1) SMM: Figure 10 presents an overlay of a CBCT-slice in the z-plane (imported in dViewX) before and after insertion. The dominance of the overlap of both CBCT-slices is 50%. The calculated centroid of the skin marker model was selected, indicated at the green crossing, in both slices before overlaying the images. The displacement of the centroid is smaller than the VMD in all directions, resulting in the overlap of the green crossings and visually indistinguishable SMM. After overlaying, the skin markers were marked. In Figure 11, a boxplot of the SMM_x, SMM_y and SMM_z is provided for all ECs. The mean SMM in all directions is close to zero and all standard deviations (SD) values (except the LS, HLPF SD of 0.28 *mm*) are smaller than the VMZ. Visually, no dominant insertion direction can be distinguished. Furthermore, most SMM vales are smaller than the VMZ. One cross-over and no parallel lines can be seen in Figure 12, displaying the effect plot of the SMM ED for all ECs.

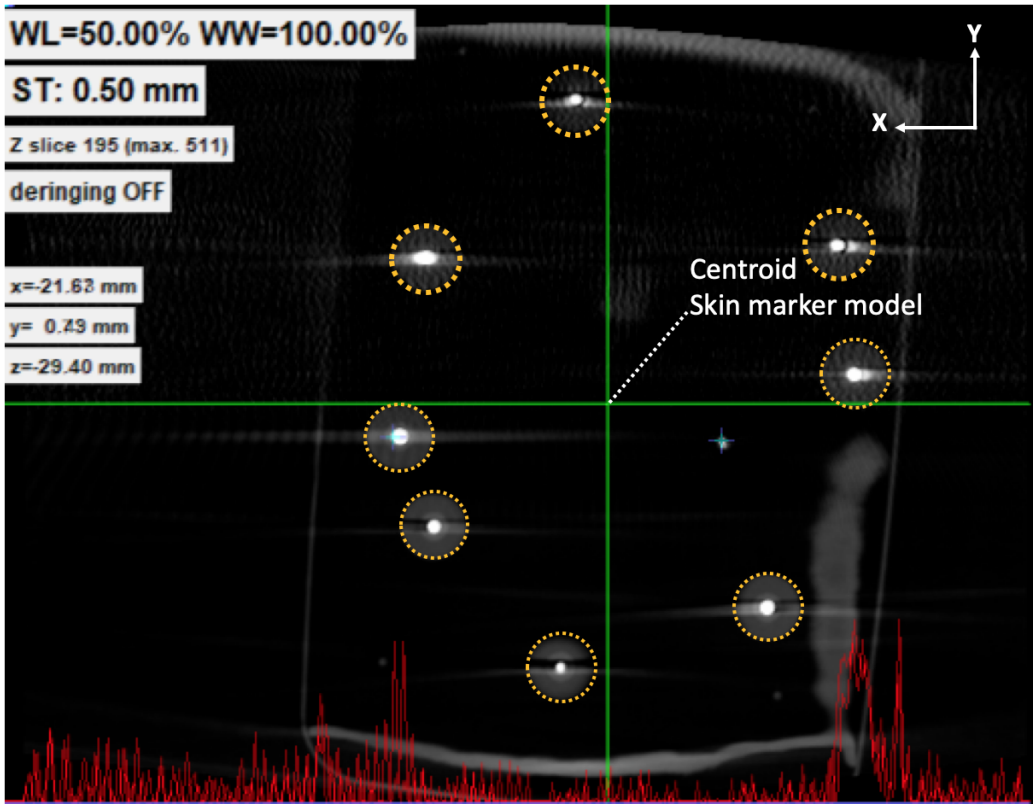

Fig. 10: An overlay of a CBCT-slice in the z-plane (in dViewX) before and after insertion. The dominance of the overlap of both CBCT-slices is 50%. The displacement of the green cross indicates the SMM. In this EU, the SMM_z was smaller then the slice thickness. Therefore, the same slice was used before and after insertion. When selecting the centroid of the marker model, the voxel closest to the corresponding calculated centroid was selected. The orange dotted lines indicate the edges of the skin markers and were applied manually after overlaying. The white dot in the bottom right quadrant, approximately 3 *cm* away from the centroid of the marker model, is the ablation needle.

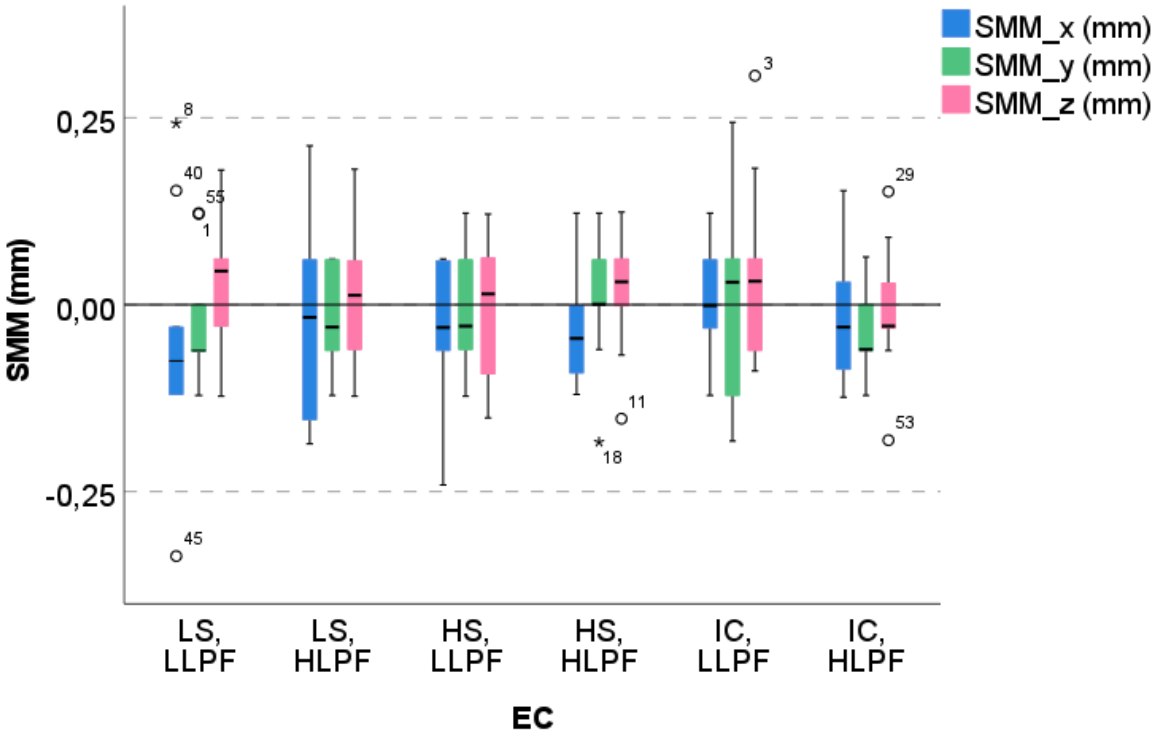

Fig. 11: Boxplot of the SMM in the x-, y- and z-direction *(mm)* (SMM_x, SMM_y and SMM_z) by EC. LS = low speed, HS = high speed, IC = increments, LLPF = low level of perirenal fat, HLPF = high level of perirenal fat. The dotted lines indicate the accuracy of the coordinate selection in dViewX (0.2425 *mm* rounded up to 0.25 *mm*).

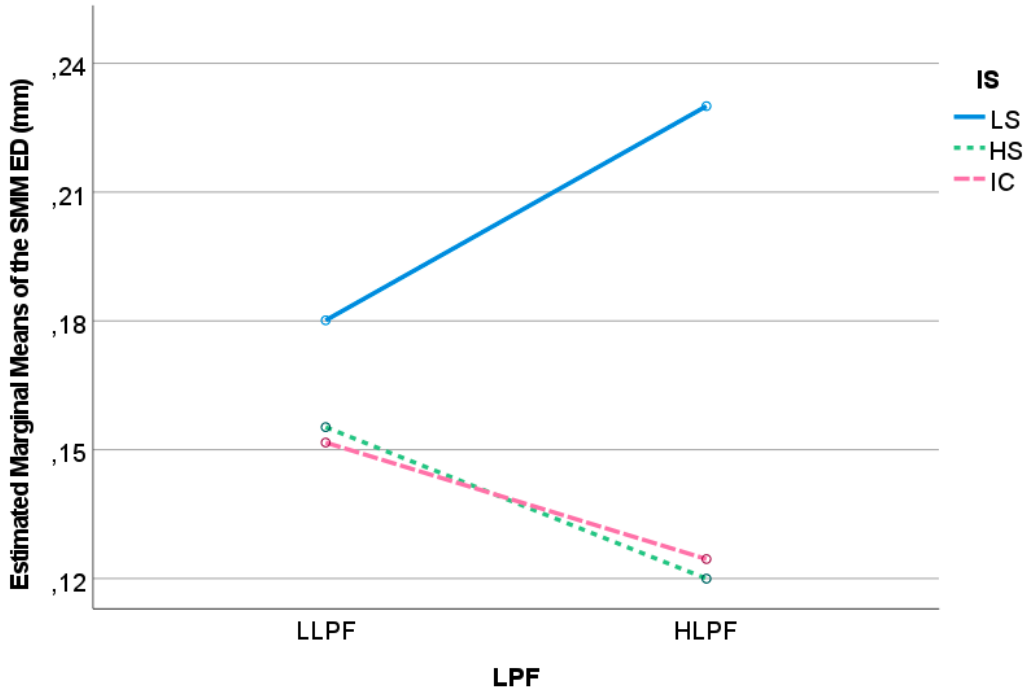

Fig. 12: Effect plot of the SMM ED (*mm*). LS = low speed, HS = high speed, IC = increments, LLPF = low level of perirenal fat, HLPF = high level of perirenal fat.

2) TMM: Figure 13 presents an overlay of a CBCT-slice in the x-plane (imported in dViewX) before and after insertion, showing typical TMM predominantly in the z-direction. The dominance of the overlay of both CBCT-slices is 50%. Additionally, the NTD (in the x-plane) is indicated. Figure 14 shows a boxplot of of the TMM_x, TMM_y and TMM_z for all ECs. In Figure 16, a boxplot of the TMM ED is presented for all ECs. Whereas the mean TMM_x and TMM_y are close to zero in all ECs, the mean TMM_z is predominantly negative (mean TMM_z = -0.96 *mm* $\pm$ 0.85 *mm*). Secondarily, the boxplot of the displacement of the needle tip in the x-, y- and z-direction (Tip_x, Tip_y and Tip_z) for all ECs shows that the dominant insertion direction is the z-direction and all Tip_z values are negative (see Figure 15). All Tip_y values are around zero, as all insertions were planned in the transversal plane. The boxplot of the SMM ED and TMM ED for all ECs shows that the mean TMM ED is larger than the mean SMM ED for all ECs (see Figure 16). Lastly, Figure 17 and 18 display the effect plots of TMM ED and and TMM_z for all ECs.

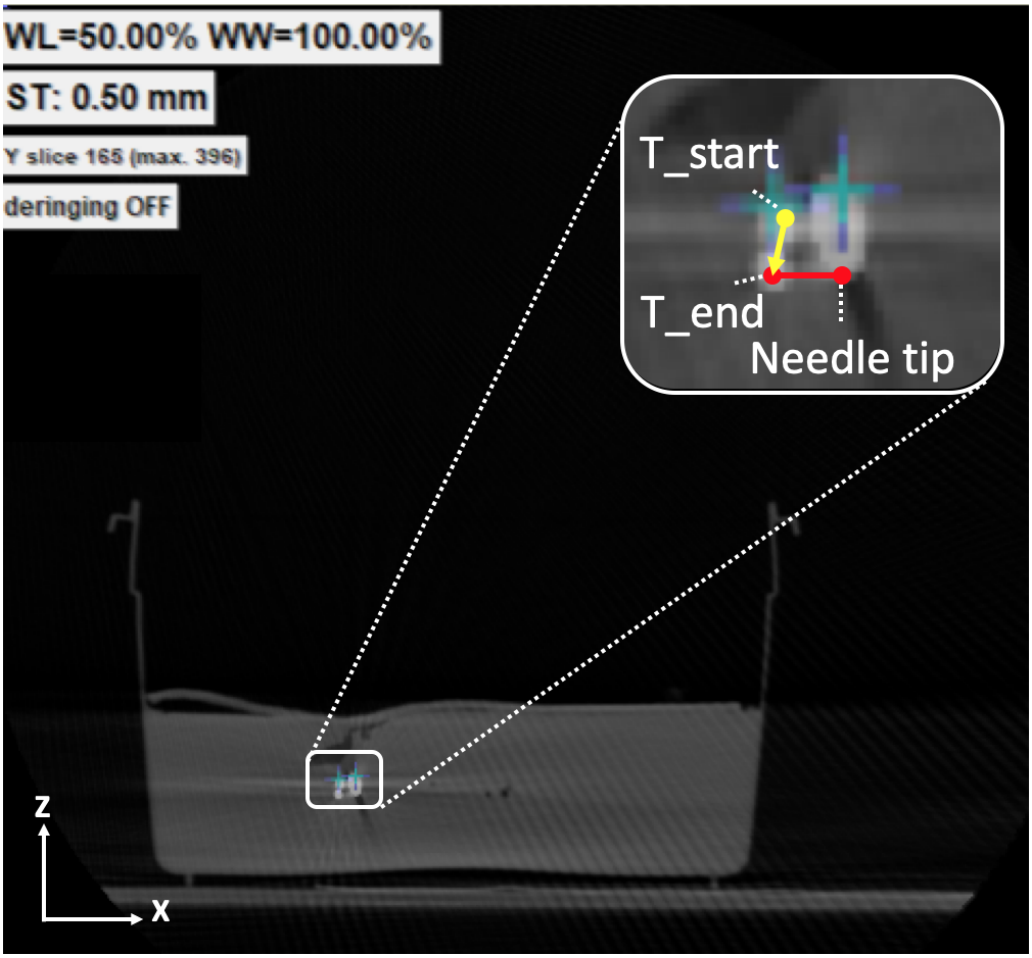

Fig. 13: An overlay of a CBCT-slice in the x-plane (in dViewX) before and after insertion. The dominance of the overlay of both CBCT-slices is 50%. The yellow arrow indicates the TMM. In this EU, the TMM in the y-direction was 0.00 *mm*. Therefore, in each CBCT, the same slice was used. The red line indicates the NTD in the x-plane.

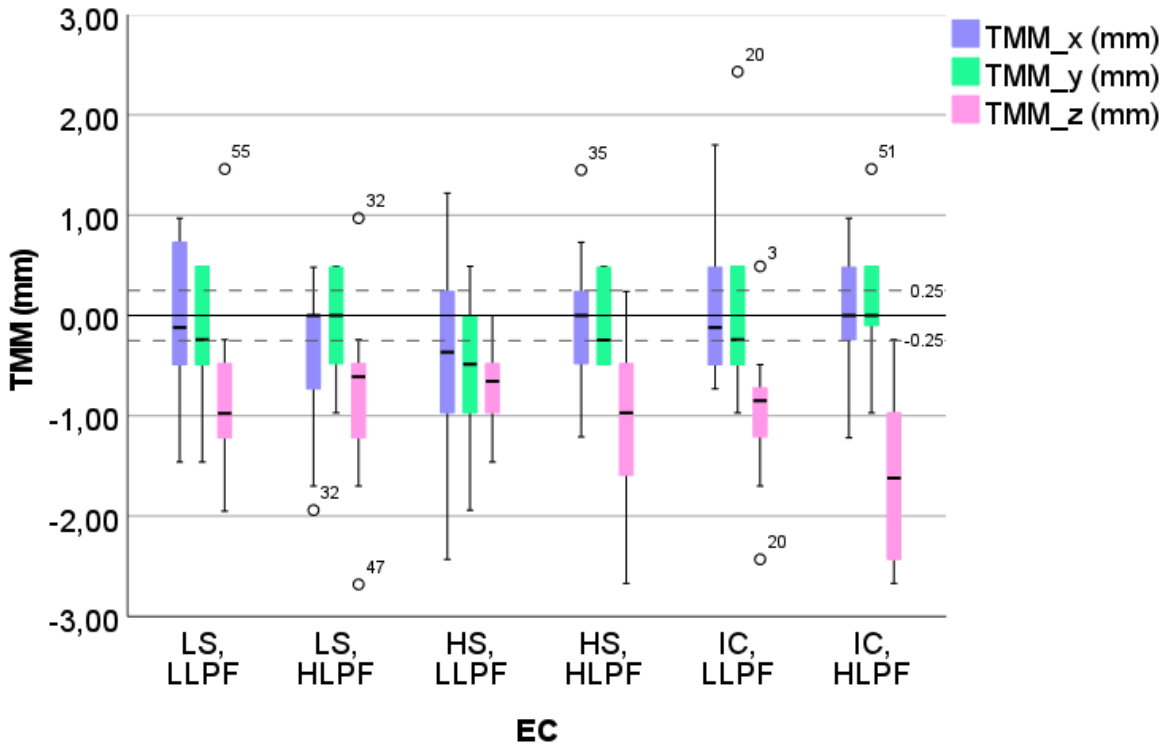

Fig. 14: Boxplot of the TMM in the x-, y- and z-direction *(mm)* (TMM_x, TMM_y, TMM_z, respectively) by EC. The dotted lines indicate the accuracy of the coordinate selection in dViewX (0.2425 *mm* rounded up to 0.25 *mm*). LS = low speed, HS = high speed, IC = increments, LLPF = low level of perirenal fat, HLPF = high level of perirenal fat.

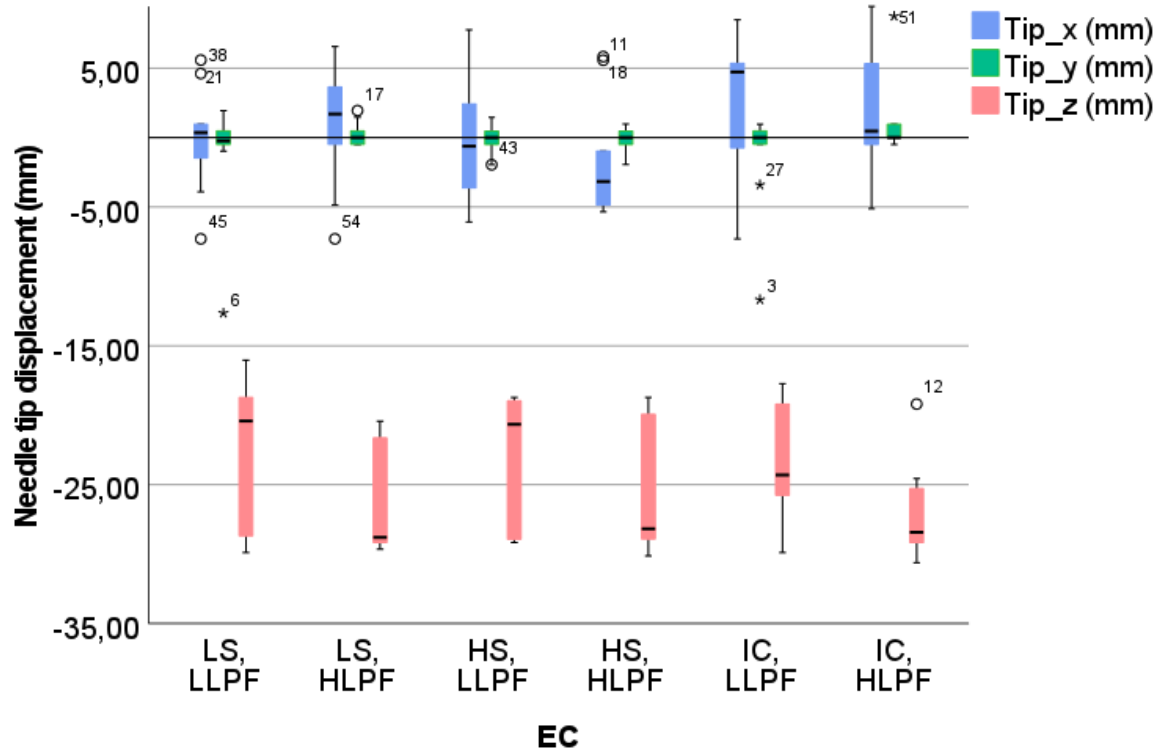

Fig. 15: Boxplot of the needle displacement in the x-, y- and z-direction (Tip_x, Tip_y, Tip_z, respectively) (*mm*) by EC. LS = low speed, HS = high speed, IC = increments, LLPF = low level of perirenal fat, HLPF = high level of perirenal fat.

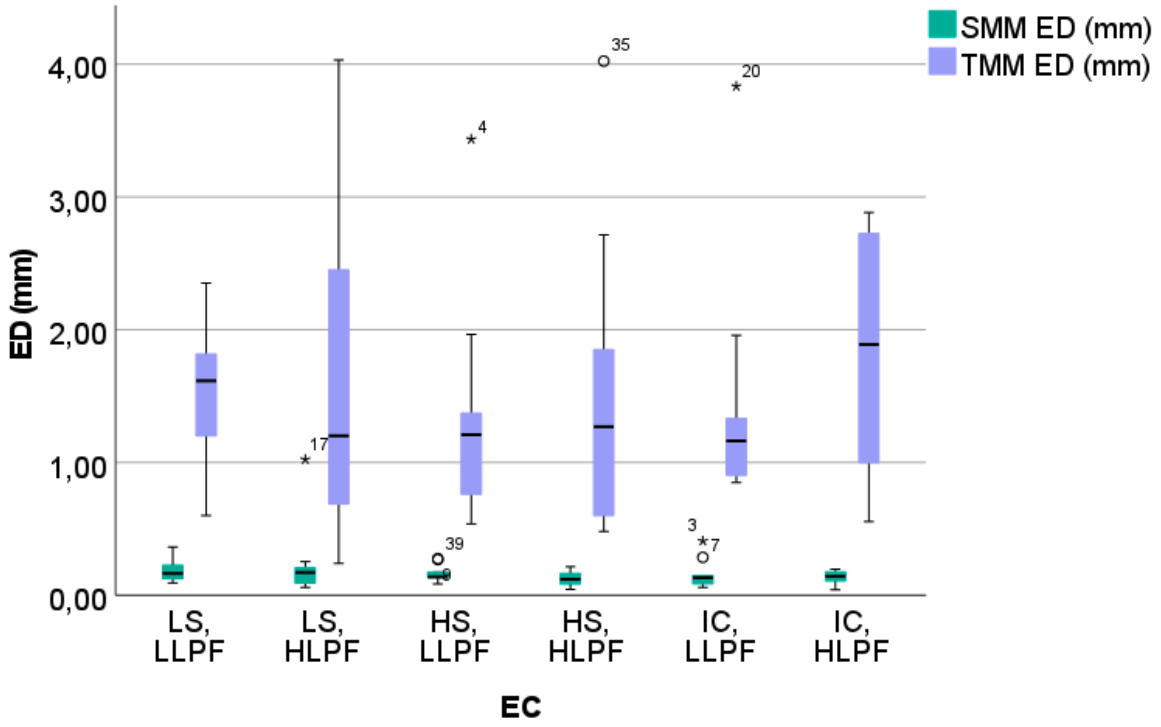

Fig. 16: Boxplot of the SMM ED (*mm*) and TMM ED (*mm*) by EC. LS = low speed, HS = high speed, IC = increments, LLPF = low level of perirenal fat, HLPF = high level of perirenal fat.

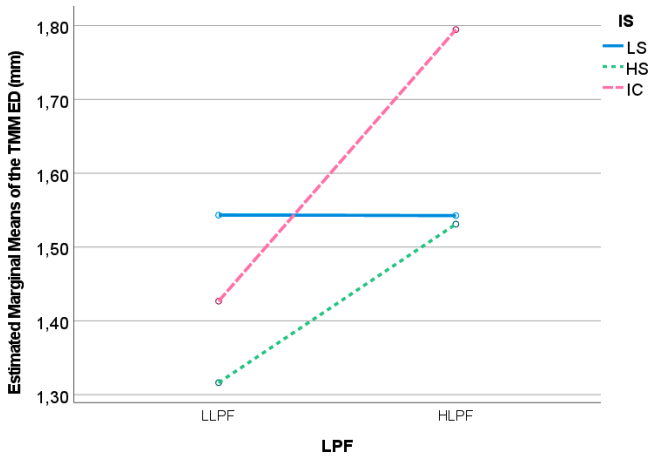

Fig. 17: Effect plot of the TMM ED (mm). LS = low speed, HS = high speed, IC = increments, LLPF = low level of perirenal fat, HLPF = high level of perirenal fat.

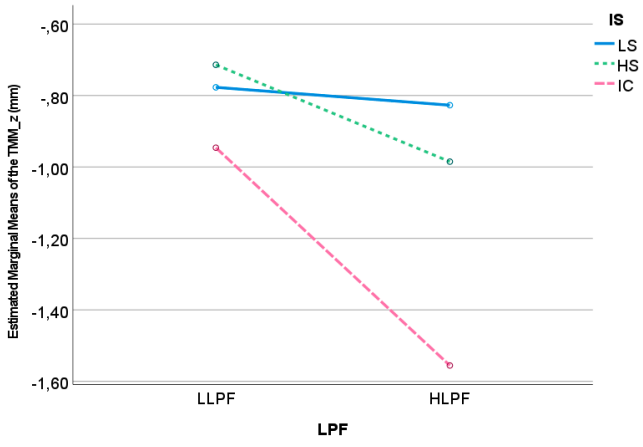

Fig. 18: Effect plot of the TMM in the z-direction (mm). LS = low speed, HS = high speed, IC = increments, LLPF = low level of perirenal fat, HLPF = high level of perirenal fat.

3) Overlap and offset: Table IX summarizes the results of the overlap and offset for the TMM and SMM in the x-, y- and z-diretion. All mean overlap values are close to zero% with SD values ranging from 16-36 %. In 10, 11 and 2 cases in the overlap in the x-, y- and z-direction, respectively, the overlap could not be calculated due to an SMM value of 0.

TABLE IX: The mean and standard deviation (SD) of the overlap (%) and offsett (*mm*) of the TMM and the SMM in the x-, y- and z-direction. n = sample size, varying per overlap direction due to varying SMM values that are equal to zero: in those EUs, the overlap could not be determined.

	Mean	SD	n
Overlap in x-direction (%)	3.4	22	49
Overlap in y-direction (%)	-4.1	36	48
Overlap in z-direction (%)	2.5	16	57
Offset in x-direction (mm)	-0.092	0.81	59
Offset in y-direction (mm)	-0.11	0.95	59
Offset in z-direction (mm)	-0.97	0.86	59

C. Statistical tests and correlations

No significant differences in mean SMM ED were observed regarding IS (p = 0.211) and LPF (p = 0.907). The two-way ANOVA showed that the observed interaction effects in Figure 12 is not significant (p = 0.559). Similarly, no significant differences in mean TMM ED regarding IS (p = 0.826) and the LPF (p = 0.440) and TMM in the z-direction regarding IS (p = 0.202) and LPF (p = 0.164) were observed. Furthermore, the two-way ANOVA showed that the observed interaction effects in Figure 17 and 18 are not significant (p = 0.833 and p = 0.585, respectively). Secondly, the mean TMM ED was significantly larger than the mean $\text{TMM}_{non-target}$ ED (1.5 *mm* vs. 0.35 *mm*, $p < 0.001$). Negligible, insignificant correlations were found between the SMM ED and TMM ED (r = -0.128), TMM ED and NTD (r = -0.203) and TMM in the z-direction and NTD (r = -0.029).

D. Remarkable observations

First, for the insertion in IC, most TMM was observed in in the last increment, approaching the tumor. Second, between most insertions targeting the same tumor (e.g. EU 43-45, 46-48, 49-52, 57-60) it was observed in the CBCT-analysis that the tumor returned to its position before insertion. In some insertions (e.g EU 28-30), on the other hand, the tumor systemically moved in the direction of the insertion and did not fully return to its initial position. Third, in insertions with an NTD smaller than approximately $two \cdot VMZ$, it was noticed that the needle tip and tumor could not be distinguished on the CBCT-scans. As a result, the NTD after 9 insertions (EU: 15, 20, 22, 29, 32, 35, 52, 55 and 57) is 0 *mm*. Lastly, the third and most inferior tumor was most challenging to reach for KUKA, requiring re-planning of the needle trajectory to a needle trajectory that was accessible for KUKA.

VII. Discussion

A. Findings

The experiment was conducted to determine whether skin markers can be used to facilitate accurate navigation in PRA. Although the limited SMM was observed, TMM occurred in the majority of the insertions.

1) Insertion accuracy: Although minimizing the NTD, for instance by re-manoeuvring the ablation needle, was not the objective of the insertions, clinically representative NTD values are desired for representative SMM and TMM values. Furthermore, the TMM may be influenced when the ablation needle punctures the tumor, corresponding with smaller NTD values. In this experiment, the insertion accuracy (NTD) in robotic insertions is influenced by: the accuracy of the planning of the needle path, the accuracy of the navigation towards the planned insertion point, the accuracy of the alignment with the planned needle orientation and the accuracy of the KUKA's insertion precision, and any possible needle deflection occurring during needle insertion (KUKA cannot control the needle deflection). The accumulation of all factors resulted in a mean NTD of 2.0 - 4.3 *mm* (SD = 1.7 - 2.6 *mm*), depending on the EC, and an overall mean NTD of 3.2 ± 2.1 *mm*. However, the two-way ANOVA results imply that neither the IS nor the LPF has had a significant impact on the NTD. The insertion accuracy reached in this experiment was comparable to reported insertion accuracy values in Maier-Hein et al. [33] (mean NTD = 2.8 - 4.5 *mm*, SD = 1.4 - 2.7 *mm*), in which both novices and experts performed manual CT-guided needle insertions in liver tumors. De Baere et al. [15] performed CT-guided robotic insertions on a fiducial in the kidney of an in-vivo swine, resulting in a mean NTD of 2.8 *mm* (SD = 1.8 *mm*). Hiraki et al. [25] reported a comparable mean NTD of 2.8 *mm* (SD = 0.8 *mm*) for a comparable experiment, targeting a fiducial in the kidney, performed with the same ablation needle as this thesis' ablation probe. Although the NTD values in this experiment resonate with the reported insertion accuracies above, no studies reporting insertion accuracy values in renal ablation were found. However, the majority of the NTD values in this experiment is within both the ablation zone margin of 5 *mm* around the tumor and the usual required clinical insertion accuracy margin of 3-5 *mm* [61], implying clinically representative NTD values.

2) SMM: The mean SMM_x, SMM_y and SMM_z are close to zero for all ECs, implying there is are no predominantly positive or negative directions of SMM. Furthermore, the results from the two-way ANOVA test imply that the IS and level of perirenal fat do not impact the SMM. However, as all SMM values, except three SMM values, are smaller than the measuring accuracy of one VMZ (0.24/0.25 *mm*, depending on the rounding), the results of the SMM must be interpreted with caution. On the other hand, as 98% of the SMM values are < 0.25 *mm*, it is plausible that the general SMM motion caused by needle insertion forces has been negligible in this experiment. Furthermore, it cannot be said whether this negligible amount of SMM is caused by the noise in the experiment or was actually caused by the needle insertion. This study observed the motion of the marker model based on the centroid displacement. Therefore, the fact that the calculated SMM in this study is close to 0 *mm* does not necessarily imply that none of the skin markers has displaced individually during needle insertion. However, even when observing the 8 exploratory fluoroscopy recordings, which will be briefly elaborated in the next section, visual individual SMM was only observed in 2/8 skin markers in one fluoroscopy recording, and this observed SMM was only 0-2 *mm*, having limited impact on the centroid displacement. In this experiment, except for the one excluded EU, the position of the model remained unchanged during all insertions. The negligible SMM values in this study imply that any local skin deformation caused by needle insertion is unlikely to be detected by the skin markers. This may be logical, as the size of the incisions made in the experiment was minimized, limiting major skin deformation. Furthermore, no skin markers were allowed in proximity of the insertion point, preventing any excessive individual skin marker motion. No studies reporting SMM values or maximum allowed SMM values during insertion in renal PNPs have been found, which complicates placing the results of this exploratory study in a broader context. To determine whether the range of SMM values is acceptable, the SMM results should be considered in combination with the TMM results and the required clinical accuracy of the PRA procedure.

3) TMM: When comparing Figure 14 and 15, an explanation for the predominantly negative TMM_z values could be that the tumor tends to move in the axial insertion direction. However, no trends can be seen in the overall overlap between the insertion direction and the TMM direction, presumably because of the lacking overlap in the TMM_x and Tip_x, and TMM_y and Tip_y. An explanation for this lacking overlap could be that the TMM in the lateral insertion direction tends to be more random due to the fact that the center of of approximately spherical tumors was targeted, causing the tumor to randomly displace when puncturing the tumor. The smaller Tip_y values also contributed to the lower overlap. Secondly, relatively small TMM values (mean TMM ED = 1.3 - 1.8 *mm*) compared to TMM values in for instance liver tumors (mean $\text{TMM}_{livertumor}$ ED in an ex-vivo porcine liver model: 4.06-6.79 *mm* [59]) can be explained by the superior average stiffness of the kidney [20, 45]. Thirdly, the results of the two-way ANOVA test imply that neither the IS nor the LPF impact the TMM. It was hypothesized that a higher LPF would allow the kidney to rotate during insertion, causing not only TMM of the targeted tumor, but also causing TMM of the non-target tumors. However, the TMM ED was significantly larger than the mean TMM $\text{ED}_{non-target}$ (1.5 *mm* vs. 0.35 *mm*, $p < 0.001$), which suggests that needle insertion does not necessarily lead to overall kidney rotation.

Fourthly, no correlation was found between the TMM ED and NTD (r = -0.203), which suggests that the insertion accuracy does not impact the TMM. Fourthly, it should be mentioned that 33% of the calculated TMM_x, TMM_y and TMM_z values were equal to the VMZ of 0.24 *mm* (or 0.25 *mm*, depending on the rounding) or equal to zero. Any TMM value of 0-0.25 *mm* can be caused by noise in the data collection, such as the small unavoidable bias in the manual coordinate selection or the limited VMZ value. As a result, an absence of TMM can be falsely classified as a TMM value of 0.24 *mm* . Therefore, any displacements smaller than the the VMZ should be interpreted with caution. Lastly, to determine whether the detected TMM values are acceptable, the TMM results should be considered in combination with the SMM results and the required clinical accuracy of the procedure.

4) Relation SMM and TMM: First, the SMM and the TMM were compared in order to explore any possible relation between the outcomes, in order to investigate if the skin markers can to some extent account for or predict the TMM. The mean SMM and TMM overlap values close to zero and large standard deviations (3.4 $\pm$ 22 %, -4.1 $\pm$ 36 % and 2.5 $\pm$ 16 % for the overlap in the x-, y- and z-direction, respectively, see Table IX), in combination with the negligible correlation between the SMM ED and TMM ED (r = -0.128), suggest that the SMM cannot predict the TMM. Furthermore, the total mean offset expressed in ED is 8.9 times larger than the overall mean SMM ED. Regardless of the limited validity of the small SMM ED values and TMM ED values, Figure 16 shows that the TMM ED is predominantly larger than the SMM ED in all ECs. This experiment implies, although any local skin deformation caused by needle insertions translated into negligible SMM, translating into negligible virtually detected change in the position of the patient in the navigation system, needle insertions cause TMM. However, the median TMM ED values range from 1.2 - 1.9 *mm* (see Table X, implying that the majority of the TMM ED values are acceptable, as those TMM ED values are within the required clinical insertion accuracy of range of 3-5 *mm*. Furthermore, the majority of the TMM values allow for a margin, of which the magnitude depends on the summation strategy of the error sources, for additional error sources: for instance, errors in the needle path planning, errors in the registration of the image-guided therapy system (see Section VII-A1), or errors in the virtual position of the patient caused by the needle insertion. Based on the Root Sum of Squares (RSS) method[12], the generally maximum allowed registration error (RE) of 2.0 *mm* [61] fits in the average allowed margin for additional error sources. Therefore, this study implies that, although the skin markers do not register tumor motion, skin markers can, regardless of the IS and LPF, still be used to track the position of the patient, facilitating accurate navigation in PRA, because the observed TMM values are acceptable.

B. Limitations

First, some limitations of this experiment regard to the used kidney model. In Section IV-E3, these limitations are elaborated. The main model limitation with regard to the TMM values is the fact that only one tumor type was simulated in the kidney model, while RCCs greatly differ in size, texture, shape and heterogeneity. Therefore, both the question how different tumors displace due to needle insertions and if skin markers can also be used in different tumors remain. Similarly, one average perirenal fat simulation was used. However, the perirenal fat varies per patient in elasticity and is usually less homogeneous than the gelatin. Therefore, the amount of TMM caused by needle insertion may be different in other perirenal fat simulations. Furthermore, the question if the LPF impacts the TMM caused by needle insertion for other perirenal fat simulations remains. Similarly, only one type of porcine skin flap (the softest available skin flaps) was used during the experiment, best approaching the elasticity of human skin. However, the elasticity of the skin greatly varies between patients. Therefore, both the question to what extent the local deformation caused by needle insertions is translated into SMM in more or less elastic skin types and if skin markers can be used to facilitate accurate navigation in PRA procedures in patients with other skin types remain.

Second, although the Azurion system, equipped with ClarifEye technology, was instrumental in performing the insertions and obtaining the positions of the skin markers and tumor markers, some limitations in this study regard to the system and technology used. For instance, the current software configuration of ClarifEye only allows planning needle paths up to 5 *mm* accuracy (path lengths of 5, 10, 15 *mm* etc.), which is lower than the desired path planning accuracy of 1 *mm*, resulting in less accurate needle insertions and an increased NTD values and possible under- and overshooting of the target. Furthermore, although CBCT-scans were performed immediately before and after insertion, Azurion's CBCT-scans cannot provide real-time imaging of the SMM and TMM. Therefore, 8 insertions were performed under fluoroscopy to exploratively observe real-time SMM and TMM during insertion. However, such fluoroscopy only provides imaging in one plane (in this case the transversal plane was chosen, because it was assumed that the TMM would be dominant in the insertion direction, which was the z-direction), complicating visualization of the SMM and TMM in the x-direction. Furthermore, performing insertions under fluoroscopy either required directing of KUKA from outside the lab, which is challenging due to limited visibility of the ablation needle from a distance, or decoupling the KUKA robot between aligning and inserting the ablation needle, which demanded restarting of KUKA, which is time consuming. An alternative imaging modality to overcome this limitation is using US. However, as described in Section I, US-guided insertions are also associated with limitations. Also, despite the re-calibration of the Azurion system before the experiment, a registration error, of which the magnitude is unknown, cannot be

[12]Assuming the TMM and RE are the only error sources and assuming independency of the error sources

avoided. Moreover, an unavoidable delay in tracking of approximately 0.5 seconds complicated directing KUKA to navigate the ablation needle to the desired insertion point and orientation, which may have impacted the accuracy of the positioning and alignment of the ablation needle, increasing the NTD. Third, performing robotic-assisted insertions allowed for regulation of the IS and insertion depth. However, some experimental limitations are indeed regarded to the use of KUKA. For instance, it was not possible at the time of performing the experiment for KUKA to measure the insertion forces, even though the detection of any possible force peaks in the insertion force may have been useful in assessing whether a tumor has been punctured and the insertion force is known to be related to soft-tissue deformation [30]. Moreover, even if force measurement was possible, the accuracy of the translation of the insertion force at the needle tip to the insertion force measured at KUKA's end-effector is limited due to possible wringing of the ablation needle in the needle holder and possible wringing between the needle holder and the end-effector. Furthermore, the robotic insertions disabled re-manoeuvring of the ablation needle during insertion to account for intermediate TMM, decreasing the NTD. Also, the use of KUKA, which contains metal components, resulted in the occurrence of beam hardening artefacts on the CBCT-scans, sometimes visually complicating the marker and needle tip segmentation. Fourth, while preparing the tumors it was observed that the fiducial was not moving while compressing the tumor and that it was challenging for a needle to move the fiducial. However, no contrast was used in this study, making the edges of the tumor invisible on the CBCT scans. As a result, the TMM caused by motion of the fiducial marker within the tumor or caused by TM could not be distinguished in this study. Therefore, it is recommended to enhance the tumors with contrast fluid in future studies. Fifth, the insertion angle was disregarded as an independent variable due to the limited reach of KUKA. However, it is recommended to also take the insertion angle into account in future studies, as a possible relation has been identified between the insertion direction and the axial TMM. Sixth, in the majority of the IC insertions, only the first, penultimate and last CBCT-scans were analyzed due to time restrictions. Lastly, despite the fact that the manual marker selection method appeared sufficiently accurate, some limitations regard the coordinate selection. For instance, the accuracy of the selection was the size of one VMZ, whereas the accuracy of the automated coordinate selection calculates the center of markers with a sub-voxel accuracy. Furthermore, in insertions with a greater accuracy (smaller NTD), it was more challenging to select the target tumor marker due to overlap of the fiducial with the blurry needle tip, which may have resulted in a less accurate NTD calculation in more accurate insertions.

C. Future research

First, four future research recommendations relate to the used kidney model: (1) it is recommended to vary the types of tumors in the kidney model in terms of size, homogeneity, hardness and location to see how the TMM varies per tumor type, because RCCs differ in characteristics [48, 53]; (2) as mentioned in Section VII-B, contrast should be added to the tumors; (3) it is recommended to vary the types of kidney fixation material in terms volume, simulating the LPF, homogeneity, as some patients have more nodular perirenal fat than others, and stiffness [53] [53]. However, to approach the real elasticity of perirenal fat, future research investigating the elasticity of perirenal fat is first required; (4) it is recommended to vary the types of skin in terms of stiffness, as the stiffness of skin greatly varies between patients [48]. Second, the possibilities for real-time 3D imaging to perform experiments with a similar set-up and design as described in Sections IV and V-A4 should be explored. For instance, the cameras integrated in the detector of the C-arm may be used to record real-time SMM. Third, although this study was only focused on the displacement of the centroid of the marker model, as the registration and tracking mechanisms in Philip's C-arm systems are partially based on centroid displacement, future research exploring the behavior of individual markers and the effect of adjustments in the marker model on the SMM during needle insertion could be used to define the optimal marker model configurations per insertion. Lastly, another recommended future research direction should be focused on the impact of navigation, facilitated by skin markers, on the accuracy of the needle insertion (NTD) in PRA. For instance, user experiments comparing the needle insertion accuracy of insertions in PRA with and without navigation with skin markers could be set-up. Consequently, if skin markers appear to improve the insertion accuracy, studies assessing the impact of navigation with skin markers on the workflow of the physician are desired in order to assess the chance of the technology to be implemented in clinical practice. Eventually, if skin markers are to be implemented in clinical practice in PRA procedures more often, studies comparing the clinical outcomes of PRA performed with skin marker navigation/tracking to the PRA performed with other navigation strategies are recommended.

VIII. Conclusion

The aim of this experiment was to explore the motion of both the skin marker model and kidney tumor caused by needle insertion, considering the IS and LPF, to evaluate the potential of skin markers to facilitate accurate navigation in PRA. First, any local skin deformations caused by the needle insertions translated into negligible SMM. However, needle insertions caused TMM in relation to the skin marker model. However, the range of observed TMM was acceptable, as the TMM values were smaller than the required clinical insertion accuracy. Therefore, based on this study's ex-vivo porcine kidney model and experiment, skin markers can be used to facilitate accurate navigation in PRA. Secondly, the IS and LPF do neither impact the amount of SMM nor the amount and of TMM in this experiment.

[1] Azurion 7 c12 azurion 7 f12.

[2] Encoris pcnl kidney training system model with case. https://anatomywarehouse.com/encoris-pcnl-kidney-training-system-model-with-case-a-112088.

[3] Philips expands augmented reality surgical navigation—clarifeye—to two new international sites with successful clinical outcomes.

[4] Research randomizer.

[5] Zenition 70: Mobile c-arm with flat detector.

[6] Kidney cancer statistics, 2020.

[7] Rakkunedeth H. Abhilash and Sunita Chauhan. Respiration-induced movement correlation for synchronous noninvasive renal cancer surgery. *IEEE Transactions on Ultrasonics, Ferroelectrics and Frequency Control*, 59:1478–1486, 7 2012. Web of Science.

[8] Fabian Adams, Tian Qiu, Andrew Mark, Benjamin Fritz, Lena Kramer, Daniel Schlager, Ulrich Wetterauer, Arkadiusz Miernik, and Peer Fischer. Soft 3d-printed phantom of the human kidney with collecting system. *Annals of Biomedical Engineering*, 45:963–972, 4 2017.

[9] Patrick M. Aubin Member Maarja Kruusmaa Rivo Öpik Andres Hunt, Asko Ristolainen. Development of high fidelity liver and kidney phantom organs for use with robotic surgical systems. *The Fourth IEEE RAS/EMBS International Conference on Biomedical Robotics and Biomechatronics*, pages 425–430, 6 2012.

[10] Elizabeth A Barnes, Brad R Murray, Donald M Robinson, Lori J Underwood, John Hanson, and Wilson H.Y Roa. Dosimetric evaluation of lung tumor immobilization using breath hold at deep inspiration. *International Journal of Radiation Oncology*Biology*Physics*, 50:1091–1098, 7 2001.

[11] Ranjit Barua, Surajit Das, Sudipto Datta, Pallab Datta, and Amit Roy Chowdhury. Study and experimental investigation of insertion force modeling and tissue deformation phenomenon during surgical needle-soft tissue interaction. *Proceedings of the Institution of Mechanical Engineers, Part C: Journal of Mechanical Engineering Science*, 237:1007–1014, 3 2023.

[12] M. Baumhauer, T. Simpfendörfer, B. P. Müller-Stich, D. Teber, C. N. Gutt, J. Rassweiler, H. P. Meinzer, and I. Wolf. Soft tissue navigation for laparoscopic partial nephrectomy. *International Journal of Computer Assisted Radiology and Surgery*, 3:307–314, 9 2008.

[13] Neil Bannister Broggio and John. Cancer survival by stage at diagnosis for england (experimental statistics): Adults diagnosed 2012, 2013 and 2014 and followed up to 2015, Jun 2016.

[14] Wong-Ho Chow. Rising incidence of renal cell cancer in the united states. *JAMA*, 281:1628, 5 1999.

[15] Thierry de Baere, Charles Roux, Guillaume Noel, Alexandre Delpla, Frederic Deschamps, Eloi Varin, and Lambros Tselikas. Robotic assistance for percutaneous needle insertion in the kidney: preclinical proof on a swine animal model. *European Radiology Experimental*, 6:13, 12 2022.

[16] Pedro P. de Sá Earp. Percutaneous renal surgery: new model for learning and training. *International braz j urol*, 29:151–154, 4 2003.

[17] G. Dedong, L. Yong, and Y. Bin. Dynamic soft tissue deformation estimation based on energy analysis. *Chinese Journal of Mechanical Engineering*, 6:1167–1175, 2016.

[18] N. Reed Dunnick. Renal cell carcinoma: staging and surveillance. *Abdominal Radiology*, 41:1079–1085, 6 2016.

[19] B. Escudier, C. Porta, M. Schmidinger, N. Rioux-Leclercq, A. Bex, V. Khoo, V. Grünwald, S. Gillessen, and A. Horwich. Renal cell carcinoma: Esmo clinical practice guidelines for diagnosis, treatment and follow-up. *Annals of Oncology*, 30:706–720, 5 2019.

[20] Douglas W. Evans, Emma C. Moran, Pedro M. Baptista, Shay Soker, and Jessica L. Sparks. Scale-dependent mechanical properties of native and decellularized liver tissue. *Biomechanics and Modeling in Mechanobiology*, 12:569–580, 6 2013.

[21] Irene Fuhrmann, Ute Probst, Philipp Wiggermann, and Lukas Beyer. Navigation systems for treatment planning and execution of percutaneous irreversible electroporation. *Technology in Cancer Research & Treatment*, 17:153303381879179, 1 2018.

[22] L. W. Goldman. Principles of ct: Radiation dose and image quality. *Journal of Nuclear Medicine Technology*, 35:213–225, 12 2007.

[23] João Gomes-Fonseca, Alice Miranda, Pedro Morais, Sandro Queirós, António C. M. Pinho, Jaime C. Fonseca, Jorge Correia-Pinto, Estêvão Lima, and João L. Vilaça. *A Dual-Modal CT/US Kidney Phantom Model for Image-Guided Percutaneous Renal Access*. 2018.

[24] Nobuhiko Hata, Sang-Eun Song, Olutayo Olubiyi, Yasumichi Arimitsu, Kosuke Fujimoto, Takahisa Kato, Kemal Tuncali, Soichiro Tani, and Junichi Tokuda. Body-mounted robotic instrument guide for image-guided cryotherapy of renal cancer. *Medical Physics*, 43:843–853, 1 2016. Web of Science¡br/¿.

[25] Takao Hiraki, Takayuki Matsuno, Tetsushi Kamegawa, Toshiyuki Komaki, Jun Sakurai, Ryutaro Matsuura, Takuya

Yamaguchi, Takanori Sasaki, Toshihiro Iguchi, Yusuke Matsui, Hideo Gobara, and Susumu Kanazawa. Robotic insertion of various ablation needles under computed tomography guidance: Accuracy in animal experiments. *European Journal of Radiology*, 105:162–167, 8 2018.

[26] John M. Hollingsworth, David C. Miller, Stephanie Daignault, and Brent K. Hollenbeck. Rising incidence of small renal masses: A need to reassess treatment effect. *JNCI: Journal of the National Cancer Institute*, 98:1331–1334, 9 2006.

[27] Andres Hunt, Asko Ristolainen, Peeter Ross, Rivo Öpik, Andres Krumme, and Maarja Kruusmaa. Low cost anatomically realistic renal biopsy phantoms for interventional radiology trainees. *European Journal of Radiology*, 82:594–600, 4 2013.

[28] Mary Jayson and Holt Sanders. Increased incidence of serendipitously discovered renal cell carcinoma. *Urology*, 51:203–205, 2 1998.

[29] Stephan Jutzi, Florian Imkamp, Markus A. Kuczyk, Ute Walcher, Udo Nagele, and Thomas R. W. Herrmann. New ex vivo organ model for percutaneous renal surgery using a laparoendoscopic training box: the sandwich model. *World Journal of Urology*, 32:783–789, 6 2014.

[30] Yo Kobayashi, Akinori Onishi, Hiroki Watanabe, Takeharu Hoshi, Kazuya Kawamura, Makoto Hashizume, and Masakatsu G. Fujie. Development of an integrated needle insertion system with image guidance and deformation simulation. *Computerized Medical Imaging and Graphics*, 34:9–18, 1 2010.

[31] Zhi-Cheng Li, Kai Li, Hai-Lun Zhan, Ken Chen, Jia Gu, and Lei Wang. Augmenting intraoperative ultrasound with preoperative magnetic resonance planning models for percutaneous renal access. *BioMedical Engineering OnLine*, 11:60, 2012. Pubmed.

[32] Chi-Lun Lin and Guan-Jhong Lan. A computational approach to investigate optimal cutting speed configurations in rotational needle biopsy cutting soft tissue. *Computer Methods in Biomechanics and Biomedical Engineering*, 22:84–93, 1 2019.

[33] Lena Maier-Hein, Aysun Tekbas, Alexander Seitel, Frank Pianka, Sascha A. Müller, Stefanie Satzl, Simone Schawo, Boris Radeleff, Ralf Tetzlaff, Alfred M. Franz, Beat P. Müller-Stich, I. Wolf, H.-U. Kauczor, B. M. Schmied, and H.-P. Meinzer. ¡i¿in vivo¡/i¿ accuracy assessment of a needle-based navigation system for ct-guided radiofrequency ablation of the liver. *Medical Physics*, 35:5385–5396, 11 2008.

[34] Kamran Mohiuddin and Scott J. Swanson. Maximizing the benefit of minimally invasive surgery. *Journal of Surgical Oncology*, 108:315–319, 10 2013.

[35] Pedro Moreira, Momen Abayazid, and Sarthak Misra. Towards physiological motion compensation for flexible needle interventions. In *2015 IEEE/RSJ International Conference on Intelligent Robots and Systems (IROS)*, pages 831–836, 2015.

[36] Michael Müller, Marie-Claire Rassweiler, Jan Klein, Alexander Seitel, Matthias Gondan, Matthias Baumhauer, Dogu Teber, Jens J. Rassweiler, Hans-Peter Meinzer, and Lena Maier-Hein. Mobile augmented reality for computer-assisted percutaneous nephrolithotomy. *International Journal of Computer Assisted Radiology and Surgery*, 8:663–675, 7 2013.

[37] Mike M. Nguyen, Inderbir S. Gill, and Lars M. Ellison. The evolving presentation of renal carcinoma in the united states: Trends from the surveillance, epidemiology, and end results program. *Journal of Urology*, 176:2397–2400, 12 2006.

[38] A. Tejo Otero, F. Fenollosa, and I. Buj. Mimicking soft living tissues for 3d printed surgical planning prototypes using different materials. 11 2019.

[39] Sandeep Anand Padala, Adam Barsouk, Krishna Chaitanya Thandra, Kalyan Saginala, Azeem Mohammed, Anusha Vakiti, Prashanth Rawla, and Alexander Barsouk. Epidemiology of renal cell carcinoma. *World Journal of Oncology*, 11:79–87, 2020.

[40] D. Pham, T. Kron, F. Foroudi, M. Schneider, and S. Siva. A review of kidney motion under free, deep and forced-shallow breathing conditions: Implications for stereotactic ablative body radiotherapy treatment. *Technology in Cancer Research & Treatment*, 13:315–323, 8 2014.

[41] Phillip M. Pierorazio, Michael H. Johnson, Hiten D. Patel, Stephen M. Sozio, Ritu Sharma, Emmanuel Iyoha, Eric B. Bass, and Mohamad E. Allaf. Management of renal masses and localized renal cancer: Systematic review and meta-analysis. *Journal of Urology*, 196:989–999, 10 2016.

[42] Ali Pirasteh, Laura Snyder, Nicholas Boncher, Matthew Passalacqua, David Rosenblum, and J. David Prologo. Cryoablation vs. radiofrequency ablation for small renal masses. *Academic Radiology*, 18:97–100, 1 2011.

[43] Lauren H. Poniatowski, Sneha S. Somani, Domenico Veneziano, Sean McAdams, and Robert M. Sweet. Characterizing and simulating needle insertion forces for percutaneous renal access. *Journal of Endourology*, 30:1049–1055, 10 2016.

[44] Tahir Qayyum, Grenville Oades, Paul Horgan, Michael Aitchison, and Joanne Edwards. The epidemiology and risk factors for renal cancer. *Current Urology*, 6:169–174, 2 2013.

[45] Daniela Radulescu, Ileana Peride, Lucian Cristian Petcu, Andrei Niculae, and Ionel Alexandru Checherita. Supersonic shear wave ultrasonography for assessing tissue stiffness in native kidney. *Ultrasound in Medicine Biology*, 44:2556–2568, 12 2018.

[46] Marc Regier and Felix Chun. Thermal ablation of renal tumors. *Deutsches Ärzteblatt international*, 6 2015.

[47] Asko Ristolainen, Peeter Ross, Juri Gavšin, Eero Semjonov, and Maarja Kruusmaa. Economically affordable anatomical kidney phantom with calyxes for puncture and drainage training in interventional urology and radiology. *Acta Radiologica Short Reports*, 3:204798161453423, 6 2014.

[48] Hester Scheffer. Interview with dr. h. scheffer, conducted by marlein vogels on 23 february 2023. *Interventional radiology, Amsterdam UMC, The Netherlands*, 2023.

[49] Weixin Si, Xiangyun Liao, Yinling Qian, and Qiong Wang. Mixed reality guided radiofrequency needle placement: A pilot study. *IEEE Access*, 6:31493–31502, 2018.

[50] Stephen B. Solomon and Stuart G. Silverman. Imaging in interventional oncology. *Radiology*, 257:624–640, 12 2010.

[51] Michael J. Stone, Aradhana M. Venkatesan, Julia Locklin, Peter Pinto, Marston Linehan, and Bradford J. Wood. Radiofrequency ablation of renal tumors. *Techniques in Vascular and Interventional Radiology*, 10:132–139, 6 2007.

[52] Walter Ludwig Strohmaier and Andreas Giese. Ex vivo training model for percutaneous renal surgery. *Urological Research*, 33:191–193, 6 2005.

[53] Otto Stroosma. Interview with dr. o. stroosma, conducted by marlein vogels on 23 february 2023. *Philips, Urology department*, 2023.

[54] Aitor Tejo-Otero, Felip Fenollosa-Artés, Isabel Achaerandio, Sergi Rey-Vinolas, Irene Buj-Corral, Miguel Ángel Mateos-Timoneda, and Elisabeth Engel. Soft-tissue-mimicking using hydrogels for the development of phantoms. *Gels*, 8:40, 1 2022.

[55] Junichi Tokuda, Laurent Chauvin, Brian Ninni, Takahisa Kato, Franklin King, Kemal Tuncali, and Nobuhiko Hata. Motion compensation for mri-compatible patient-mounted needle guide device: estimation of targeting accuracy in mri-guided kidney cryoablations. *Physics in Medicine & Biology*, 63:085010, 4 2018. Pubmed.

[56] Robert M. Turner, Todd M. Morgan, and Bruce L. Jacobs. Epidemiology of the small renal mass and the treatment disconnect phenomenon. *Urologic Clinics of North America*, 44:147–154, 5 2017.

[57] Juliet Usher-Smith, Rebecca K. Simmons, Sabrina H. Rossi, and Grant D. Stewart. Current evidence on screening for renal cancer. *Nature Reviews Urology*, 17:637–642, 11 2020.

[58] Marieke van Dommele. Narrative review on image-guided therapy and soft-tissue tracking during percutaneous needle procedures in the abdomen. 2021.

[59] Marieke van Dommele. Towards more continuous feedback on soft tissue anatomy during percutaneous needle placement in the liver. 2023.

[60] Adrienne van Randen, Wytze Laméris, H. Wouter van Es, Hans P. M. van Heesewijk, Bert van Ramshorst, Wim ten Hove, Willem H. Bouma, Maarten S. van Leeuwen, Esteban M. van Keulen, Patrick M. Bossuyt, Jaap Stoker, and Marja A. Boermeester. A comparison of the accuracy of ultrasound and computed tomography in common diagnoses causing acute abdominal pain. *European Radiology*, 21:1535–1545, 7 2011.

[61] Marco van Strijen. Interview with dr. m. van strijen (confidential), conducted by marlein vogels on 3 april 2023. *Jeroen Bosch Ziekenhuis, 's Hertogenbosch*, 2023.

[62] Marlein Vogels. Navigation strategies in percutaneous needle procedures in the kidney: A literature review. 2023.

[63] D. Wallach, G. Toporek, S. Weber, R. Bale, and G. Widmann. Comparison of freehand-navigated and aiming device-navigated targeting of liver lesions. *The International Journal of Medical Robotics and Computer Assisted Surgery*, 10:35–43, 3 2014.

[64] Wendong Wang, Yikai Shi, Andrew A. Goldenberg, Xiaoqing Yuan, Peng Zhang, Lijing He, and Yingjie Zou. Experimental analysis of robot-assisted needle insertion into porcine liver. *Bio-Medical Materials and Engineering*, 26:S375–S380, 8 2015.

[65] Yancheng Wang, Roland K. Chen, Bruce L. Tai, Patrick W. McLaughlin, and Albert J. Shih. Optimal needle design for minimal insertion force and bevel length. *Medical Engineering Physics*, 36:1093–1100, 9 2014.

[66] Lei Zhang, Feng Ju, Yanfei Cao, Yaoyao Wang, and Bai Chen. A tactile sensor for measuring hardness of soft tissue with applications to minimally invasive surgery. *Sensors and Actuators A: Physical*, 266:197–204, 10 2017.

[67] Yi Zhang, Tong wen Ou, Jian guo Jia, Wei Gao, Xin Cui, Jiang tao Wu, and Gang Wang. Novel biologic model for percutaneous renal surgery learning and training in the laboratory. *Urology*, 72:513–516, 9 2008.

[68] Renming Zhong, Jin Wang, Xiaoqin Jiang, Yinbo He, Hong Zhang, Nianyong Chen, Sen Bai, and Feng Xu. Hypofraction radiotherapy of liver tumor using cone beam computed tomography guidance combined with active breath control by long breath-holding. *Radiotherapy and Oncology*, 104:379–385, 9 2012.

[69] Ariana Znaor, Joannie Lortet-Tieulent, Mathieu Laversanne, Ahmedin Jemal, and Freddie Bray. International variations and trends in renal cell carcinoma incidence and mortality. *European Urology*, 67:519–530, 3 2015.

APPENDIX A
PROTOCOL

Disclaimer: This structure of this protocol is partially inspired by an experiment conducted by Van Dommele [59]

A. Protocol: Preparation kidney model

Materials

Researcher (MV) responsible: *These materials are based on making one kidney model. In case multiple models are required (in this thesis, eight models were required and prepared), the amount of materials may vary.*

- 1 x porcine kidney (must be used within 5 days after purchase)
- 3 spherical wine gums with a diameter of 8 *mm*
- 3 x metal fiducial marker (1.6 *mm*) (+ reserve)
- 1 x porcine skin flap 21 x 16 *cm* with subcutaneous fat preserved (the softest available skin flaps are preferred)
- 1 x gelatin powder (Dr. Oetker Professional Gelatinepoeder 1 *kg*, 250 bloom)
- 1 x measuring cup (measuring accuracy: *cL*, fits at least 1 *L*)
- 1 x plastic box to position the kidney model, size: 21 x 16 x 9 *cm* (length x width x height)
- 1 x bone marrow biopsy needle (Jamshidi, for fiducial insertion in tumor)
- 1 x surgical scalpel (for incisions on side of kidney)
- 1 x glue (on cyanoacrylate basis, 3 drops of glue per stitch)
- 1 x Thermometer (measuring accuracy: 0.1 $^{\circ}C$, measuring range: 1-100 $^{\circ}C$
- 4 x wooden nails to fixate the skin flap
- 1 x permanent marker
- 1 x scale (measuring accuracy: grams)
- 2 x gloves

Step by step approach

Surrounding tissue/kidney fixation preparation: gelatin base

1) Add 26 gr of gelatin to 500 *mL* of cold water and let it well for 10 minutes.
2) Warm the solution, keep stirring till the gelatin is dissolved and do not let the solution boil.
3) Pour the solution in the plastic box and store till the gelatin has set (approximately 3 hours). *In case of the low level perirenal fat model: only pour 100 mL of the solution in the plastic box.*

Surrounding tissue/kidney fixation preparation: gelatin top

4) Add 53 grams of gelatin to 1000 *mL* of cold water and let it well for 10 minutes
5) Warm the solution, keep stirring till the gelatin is dissolved and do not let the solution boil
6) Let the solution cool till $<$37 °C

Prepare tumors

7) Select three wine gums & three metal fiducial markers.
8) For each wine gum: shape the wine gum to an 8 *mm* diameter wine gum and push the metal fiducial marker slightly into the wine gum without puncturing the the wine gum.
9) For each wine gum: remove the metal fiducial marker and puncture the wine gum towards the center of the wine gum with the bone biopsy needle. Be careful not to damage the wine gum and keep the capsule of the wine gum as intact as possible.
10) For each wine gum: insert the metal fiducial marker into the wine gum through the previously defined path.
11) Gently close the wine gum's capsule once the metal fiducial marker is pushed in.
12) Repeat for all three wine gums.

Insert tumors

13) Make a lateral incision in the superior, middle and inferior region of the kidney (maximum width: 5 *mm*, depth: 10-20 *mm*).
14) Insert a wine gum (with metallic fiducial) into each incision.
15) Close the incisions and dry the incisions with kitchen paper.
16) Glue the incisions and let the glue dry.
17) Take a picture of the setup for documentation
18) Remove the skin markers again

Kidney fixation (gelatin top): Continued

19) Put the kidney on the gelatin base (100 *mL* for a low fat model and 500 *mL* for a high fat model) and slowly pour the cooled gelatin over the kidney until the kidney is fully covered in gelatin.
20) Store in the refrigerator overnight.

Skin flap attachment

21) Once the gelatin has set: remove the model from the refrigerator and place the skin flap over the kidney.
22) fixate this skin flap with 4 wooden nails at the corners of the skin flap (at least 2 cm from the edges of the box)
23) Take a picture of the setup for documentation.

Model preservation

24) Store the model in the refrigerator (at 6 °C) and remove from refrigerator at least one (preferably two) hours before the experiment. The experiment was performed at room temperature (ca. 19 °C).

When preparing multiple models, number the boxes with the permanent marker in desired order of use.

B. Protocol: Experiment

Step by step approach

Philips responsible:

- Azurion RAMI lab (with calibrated Azurion & ClarifEye)
- 1 x KUKA
- 1 x needle holder for KUKA
- 2 x 8 hybrid skin markers ClarifEye (equipped with double-sided tape on the bottom of the skin markers to attach the markers to the skin)
- ClarifEye system active on Azurion

Researcher (MV) responsible: *These materials are based on making one testing model. In case multiple models are required, the amount of materials may vary*

- 1 x kidney model (prepared according to the preparation protocol in Section A-A
- 1 x 13G ablation needle (Emprint™ Percutaneous, Antennas - 25cm, Medtronic-Covidien, Minneapolis, United States)
- 1 x surgical scalpel (for incisions on side of kidney)
- 1 x USB
- 1 x pen
- 2 x gloves for myself

Step by step approach

Before all insertions: KUKA preparation

Put the ablation needle in the needle holder.

Attach the needle holder to KUKA's end effector.

Per kidney model: Skin marker model construction

1) Place eight skin markers on the skin flap of the kidney model in a circular yet asymmetric configuration with a maximum diameter of 17 *cm*.
2) Take a picture of the setup for documentation.

Per tumor: Target tumors

3) Make new "patient"[13] in Review application on Azurion computer: e.g. M1_T1.
4) Put the kidney model with the marker model on the table in the RAMI lab (taped to an anti-slip table cover).
5) Take a picture of the setup for documentation.
6) Open the ClarifEye application and check if all skin markers are detected. Turn on "skin marker tracking".
7) Make an acquisition CBCT-scan.
8) Check that all the markers are visible in the CBCT scan. If not, move the table accordingly and remake the acquisition CBCT-scan.
9) Plan and save three needle trajectories to the tumor (maximum difference in insertion depth: 10 *mm*). Each tumor is targeted three times: once at low speed (2.5 *mm/s*), once at high speed (75 *mm/s*) and once in increments (depth 5 *mm* at 10 *mm/s*).

Per insertion: Target tumor continued

10) Go to the treatment step in ClarifEye and use the bulls eye view to manually direct KUKA (the ablation needle) to the desired insertion position.
11) Make a crosswise incision with the scalpel (maximum width and length: 3 *mm* and depth: 3 *mm*) at the insertion point.
12) Manually direct KUKA to align the ablation needle with the desired orientation matching the planned needle trajectory (once again in bulls eye view, in combination with the projection screens of the desired needle orientation).
13) Make a CBCT-scan.
14) Insert the needle at the appropriate depth and speed, using KUKAs insertion programs in acoordance with the EC.
15) Make a CBCTs after the insertion/after each increment.
16) In case of the insertion in increments: continue repeating the previous two steps until the tumor is reached.
17) Exert KUKA.
18) Repeat the previous eight steps for all three planned trajectories per tumor, inserting the ablation needle at the appropriate insertion depth and speed.

Repeat the steps for all three tumors. Make a new patient for each tumor.

[13]ClarifEye refers to one procedure as a patient. In this case, one procedure (one patient) refers to one tumor, targeted three times.

APPENDIX B
LIST OF EXPERIMENTAL UNITS

Below, the order of the performed insertions is listed, with indicated kidney model and insertion speed. M1_T1 = Model one, Tumor one

1) M1_T1 (LLPF): LS → HS → IC
2) M1_T2 (LLPF): HS → IC → LS **With fluoroscopy**
3) M1_T3 (LLPF): IC → LS → HS
4) M2_T1 (HLPF): LS → HS → IC
5) M2_T2 (HLPF): HS → IC → LS **With fluoroscopy**
6) M2_T3 (HLPF): IC → LS → HS
7) M3_T1 (LLPF): HS → IC → LS
8) M3_T2 (LLPF): IC → LS → HS
9) M3_T3 (LLPF): LS → HS → IC
10) M4_T1 (HLPF): HS → IC → LS
11) M4_T2 (HLPF): IC → LS → HS
12) M4_T3 (HLPF): LS → HS → IC
13) M5_T1 (LLPF): IC → LS → HS
14) M5_T2 (LLPF): LS → HS → IC
15) M5_T3 (LLPF): HS → IC → LS
16) M6_T1 (HLPF): IC → LS → HS
17) M6_T2 (HLPF): LS → HS → IC
18) M6_T3 (HLPF): HS → IC → LS
19) M7_T1 (LLPF): LS → HS → IC
20) M8_T1 (HLPF): LS → HS → IC
21) (M8_T2 (HLPF): HS → IC → LS) **With photos, CBCT-scans not analyzed**
22) (M8_T3 (HLPF): IC → LS → HS) **With fluoroscopy, CBCT-scans not analyzed**

APPENDIX C
HARDNESS SCALE

Below, the hardness scale used to evaluate the hardness of the gelatin simulating the perirenal fat, is elaborated. In this scale, the hardness of tissue types are related to specific human organs/body parts in terms of tactile feeling. The chosen body parts: tip of the nose, mouse of the hand, forehead and teeth are easy to reach. The hardness of other tissue can be classified by touching the tissue and comparing the feeling to the feeling of touching the tissues mentioned below, making this hardness scale a fast and practical tool to classify the hardness of other materials/tissues. Based on [59]:

1) Soft tissue: comparable to the tip of the nose [59]
2) Normal tissue: mouse on the hand [59]
3) Medium hard: forehead [59]
4) Hard tissue: teeth [59]

Alternative to this hardness scale: Shore hardness scale [38]. However, shore hardness values for tumor tissue and soft tissue are not commonly used. Furthermore, it is not possible to test the hardness of each component of the testing model - the tumors, the gelatin to mimic the tissue surrounding and fixating the kidney and the kidney itself - in the duration meter [38].

APPENDIX D
RAW DATA: SCATTER PLOTS

In this Appendix, scatter plots of the raw data of the SMM in the x-, y- and z-direction and ED (Figure 19, 20, 21, 22) and the TMM in the x-, y- and z-direction and ED (Figure 23, 24, 25, 26) are provided.

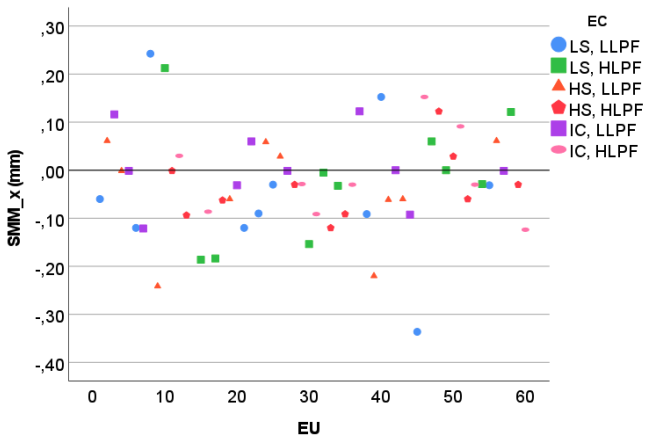

Fig. 19: Scatter plot of the SMM in the x-direction by EU and by EC.

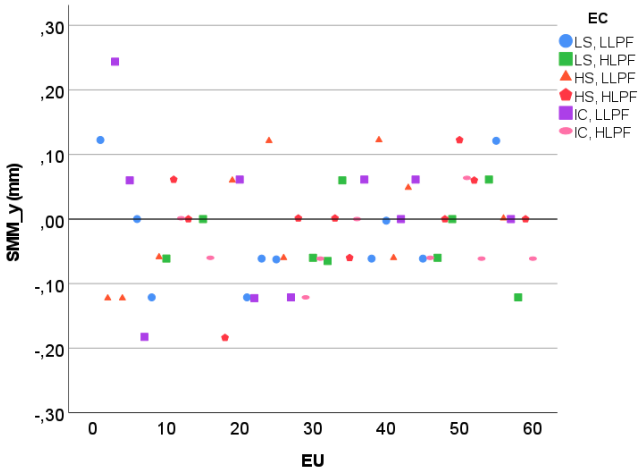

Fig. 20: Scatter plot of the SMM in the y-direction by EU and by EC.

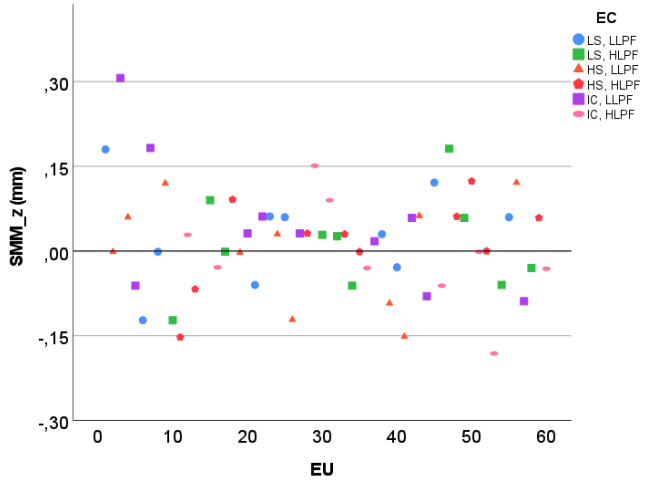

Fig. 21: Scatter plot of the SMM in the z-direction by EU and by EC.

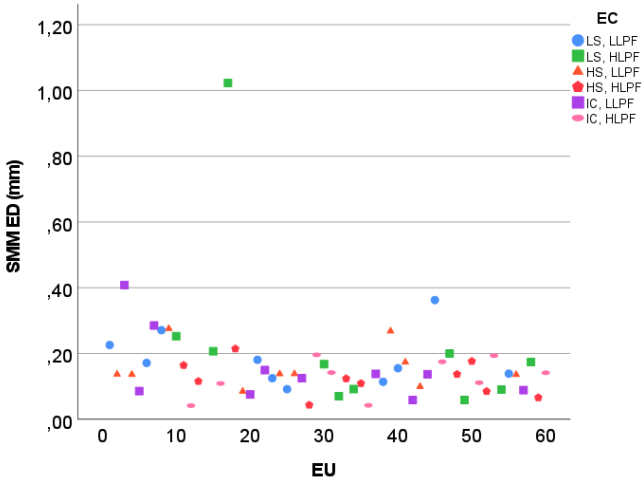

Fig. 22: Scatter plot of the SMM ED by EU and by EC.

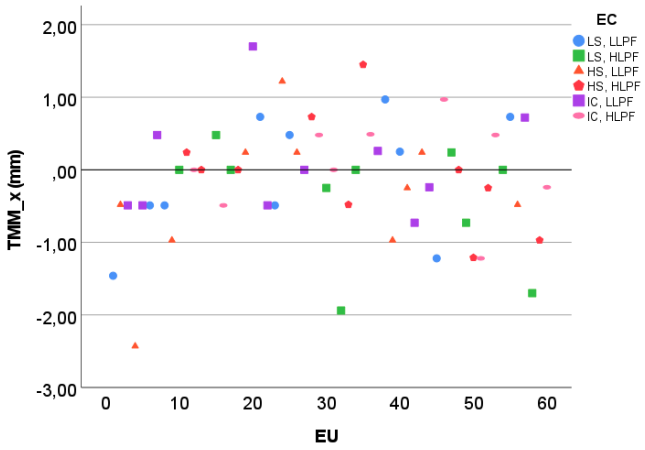

Fig. 23: Scatter plot of the TMM in the x-direction by EU and by EC.

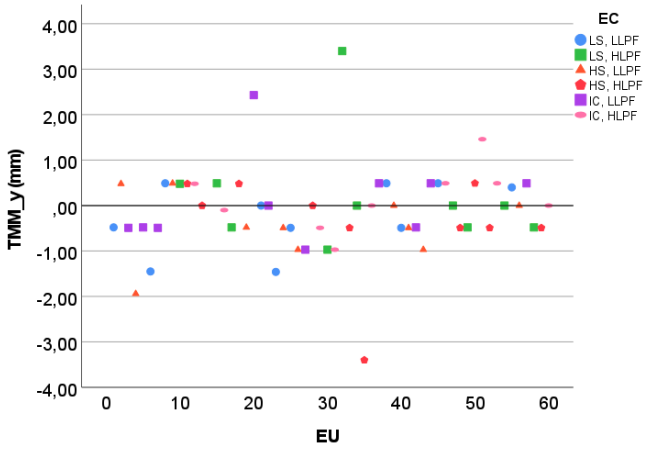

Fig. 24: Scatter plot of the TMM in the y-direction by EU and by EC.

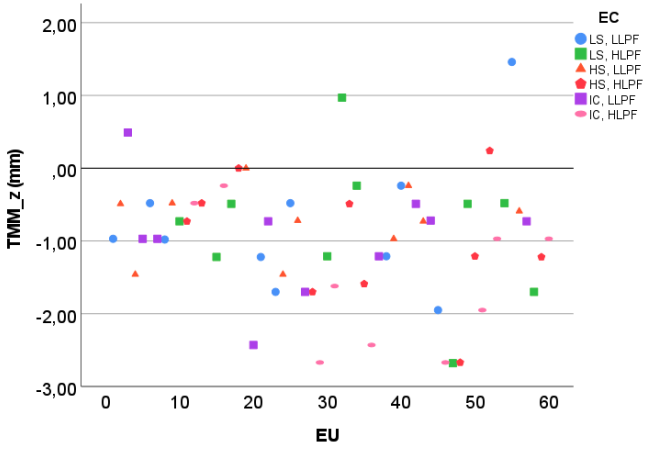

Fig. 25: Scatter plot of the TMM in the z-direction by EU and by EC.

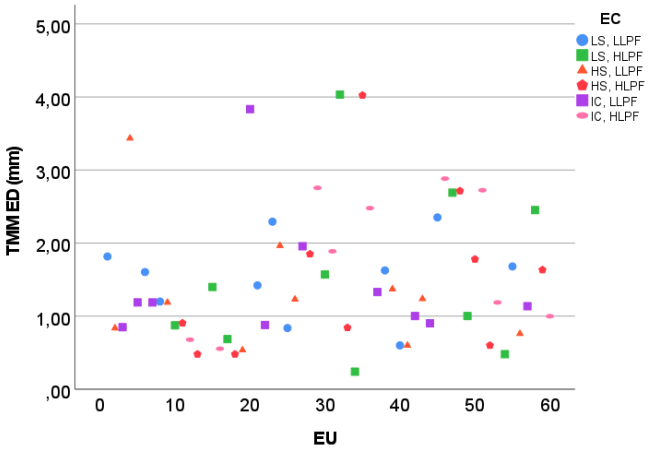

Fig. 26: Scatter plot of the TMM ED by EU and by EC.

APPENDIX E
RESULTS: STATISTICAL SUMMARY TABLE

TABLE X: Statistical summary of the results of the SMM ED, TMM ED, TMM in the z-direction (TMM_z) and NTD ED for each EC and multiple combinations of ECs. n = sample size, SD = standard deviation, SE = standard error.

Insertion speed	LPF	Statistic	SMM ED	TMM ED	TMM_z	NTD ED
LS	LLPF	Mean (mm)	0.18	1.5	-0.78	3.5
		Median (mm)	0,16	1.6	-0.98	4.4
		n	10	10	10	10
		SD (mm)	0.082	0.57	0.95	1.9
		SE (mm)	0.026	0.18	0.39	0.60
	HLPF	Mean (mm)	0.23	1.5	-0.83	2.50
		Median (mm)	0.17	1.2	-0.61	2.54
		n	10	10	10	10
		SD (mm)	0.28	1.2	0.97	2.0
		SE (mm)	0.090	0.38	0.31	0.63
	Total	Mean (mm)	0.21	1.5	-0.80	3.0
		Median (mm)	0.17	1.5	-0.85	3.1
		n	20	20	20	20
		SD (mm)	0.21	0.90	0.93	2.0
		SE (mm)	0.046	0.20	0.21	0.44
HS	LLPF	Mean (mm)	0.16	1.3	-0.71	4.3
		Median (mm)	0.14	1.2	-0.66	4.4
		n	10	10	10	10
		SD (mm)	0.064	0.86	0.47	1.9
		SE (mm)	0.020	0.27	0.15	0.60
	HLPF	Mean (mm)	0.12	1.5	-0.99	3.6
		Median (mm)	0.12	1.3	-0.97	3.4
		n	10	10	10	10
		SD (mm)	0.052	1.1	0.87	2.6
		SE (mm)	0.016	0.36	0.28	0.81
	Total	Mean (mm)	0.14	1.4	-0.85	4.0
		Median (mm)	0.14	1.2	-0.73	3.89
		n	20	20	20	20
		SD (mm)	0.060	0.99	0.70	2.2
		SE (mm)	0.013	0.22	0.16	0.50
IC	LLPF	Mean (mm)	0.16	1.4	-0.95	2.0
		Median (mm)	0.13	1.2	-0.85	1.4
		n	10	10	10	10
		SD (mm)	0.11	0.91	0.76	2.1
		SE (mm)	0.035	0.29	0.24	0.65
	HLPF	Mean (mm)	0.13	1.8	-1.6	3.3
		Median (mm)	0.14	1.9	-1.6	3.2
		n	9	9	9	9
		SD (mm)	0.058	0.95	0.93	1.7
		SE (mm)	0.019	0.32	0.31	0.44
	Total	Mean (mm)	0.14	1.6	-1.2	2.6
		Median (mm)	0.14	1.2	-0.97	2.7
		n	19	19	19	19
		SD (mm)	0.088	0.92	0.88	1.9
		SE (mm)	0.020	0.21	0.20	0.44
Total	LLPF	Mean (mm)	0.17	1.4	-0.81	3.3
		Median (mm)	0.14	1.2	-0.73	3.6
		n	30	30	30	30
		SD (mm)	0.085	0.77	0.74	2.1
		SE (mm)	0.016	0.14	0.13	0.39
	HLPF	Mean (mm)	0.16	1.6	-1.1	3.1
		Median (mm)	0.14	1.4	-0.73	3.1
		n	29	29	29	29
		SD (mm)	0.18	1.1	0.95	2.1
		SE (mm)	0.033	0.20	0.18	0.39
	Total	Mean (mm)	0.16	1.5	-0.96	3.2
		Median (mm)	0.14	1.2	-0.97	3.2
		n	59	59	59	59
		SD (mm)	0.14	0.93	0.85	2.1
		SE (mm)	0.018	0.12	0.11	0.27

APPENDIX F
PILOT EXPERIMENTS

To test the impact of the skin marker motion, insertion speed, insertion type and skin flap thickness on the SMM and TMM and consequently determine which of those variables is the main contributor to the SMM and TMM, four pilot experiments were conducted.

Secondary goals of performing the pilot experiments were:

- To get familiar with the ClarifEye software application and the Azurion system in general
- To practice steering and performing needle insertions with the KUKA robot
- To get experienced in making a porcine kidney model

The next section briefly elaborates the set-up and experimental design per pilot experiment.

A. Methods

1) General Study set-up: For each pilot experiment, a marker model consisting of 8 spherical fiducial skin markers (with a radio opaque diameter of 3.6 mm) was constructed. The initial plan for the marker construction was to position 8 spherical markers in a circular yet asymmetric configuration in a circle of 17 cm in diameter (this diameter was determined as maximal optimal resolution field of view in spine surgery in Nav4Mos study), fitting over the entire surface of the kidney. As a result, the kidney was in the field of view after registering the optical scan over the pre-operative C-arm scan. Furthermore, a metal fiducial marker (1.6 mm diameter) was placed at the center of each tumor so that the position of the tumor can be tracked. The Azurion (fixed C-arm) system was used in all pilot experiments, accomodating the ClarifEye application and providing superior image quality. The position of the model in the system was be validated by one supervisor right before performing any needle insertions. In all (pilot) experiments, the needle insertions were performed with a 13-G ablation needle (Emprint™ Percutaneous, Antennas - 25cm, Medtronic-Covidien, Minneapolis, United States) by the KUKA robot to perform insertions in a standardized way, limiting the noise in the performed insertions.

2) Experimental design and corresponding kidney models: **Marker test:** this test is performed to explore the relation between the distance between the skin marker and the needle insertion point and the motion of that skin marker. This experiment was performed on a PCNL box (Encoris PCNL Kidney Training System Model iwth Case, Anatomy Warehouse, Evanston, IL, USA) [2], see Figure 30. Although the procedure of interest for my final experiment is PRA and not stone removal, this PCNL box was considered appropriate for the marker test, as this marker test only focused on SMM and not on TMM. First, a needle trajectory was planned towards a stone in the kidney (in the PCNL box). Consequently, the KUKA robot was be navigated towards the insertion point (bulls-eye view). Once the insertion point was reached by the KUKA in the appropriate needle orientation (matching planned trajectory, visualized in the bulls-eye view), two skin markers (8 skin markers are already placed on the PCNL box to facilitate the needle path planning) were placed: one skin marker was placed 2 cm away from the insertion point (SMM_close), the other skin marker is placed 8.5 cm (SMM_far, maximum radius possible within the 17 cm diameter circle approximation) away from the insertion point. Consequently, the insertion was performed in increments of 5 mm with an average speed of 0.01 m/s.

Skin flap test: this test was performed to explore the difference in SMM and TMM between a porcine kidney model with a thin and thick skin flap. This test was performed on the porcine kidney model, schematically displayed in Figures 27 and 28. Due to the fact that the pilot experiments were planned in the beginning of the project to get acquanted with the navigation system quickly, this kidney model was developed before completing the kidney phantom research and differs from the actual kidney model. Therefore, this kidney model is only schematically presented and not explained in detail. First, a needle trajectory was planned towards the tumor marker. Consequently, the KUKA robot was be navigated towards the insertion point (bulls-eye view). One CBCT-scan is obtained. Consequently, the needle insertion was performed to reach the target in increments of 5 mm with a target average speed of 0.01 m/s. These steps were performed twice: once on the kidney model with a thick (3-4 cm) skin flap, once on the kidney model with a thin (0.5-1 cm) skin flap. In both tests, the target was be the same.

Insertion speed test: this test was performed to explore the relation between insertion speed and SMM and TMM. This test was performed on the kidney model (see Figures 27 and 28) with a thin (0.5-1 cm) skin flap. The insertion steps are similar to the skin flap test. However, once the insertion point is reached, the KUKA will perform continuous needle insertions with varying speed (2.5 mm/s and 60 mm/s, respectively). Before and after each insertion, a CBCT scan was be made and saved to a USB-stick.

Insertion increment test: this test was performed to explore the difference in SMM and TMM between continuous needle insertions and insertions in increments. This test was performed on the kidney model (see Figure 27 and 28) with a thin (0.5-1 cm) skin flap and consists of the same planning steps as the Insertion speed test. One insertion was performed continuously at 2.5 mm/s and one insertion was performed in 5 mm increments of 1 mm/s. In all tests, CBCT-scans were obtained before and after each insertion. Lastly, as the pilot experiments were performed at the beginning of the graduation internship, the porcine kidney model differs from the porcine kidney model in the final experiment. Therefore, the kidney model in the pilot experiments is not elaborated in detail.

3) Data collection: The CBCT-scans were imported to dViewX (dicom-view software, Philips Healthcare, Best, The Netherlands). Consequently, the centers of the skin markers

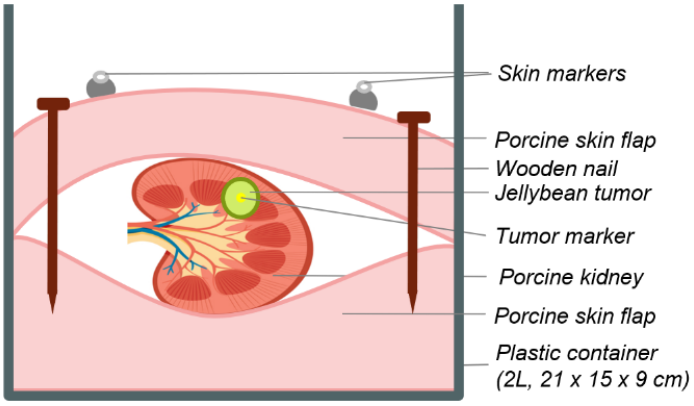

Fig. 27: Schematic sideview of the set-up

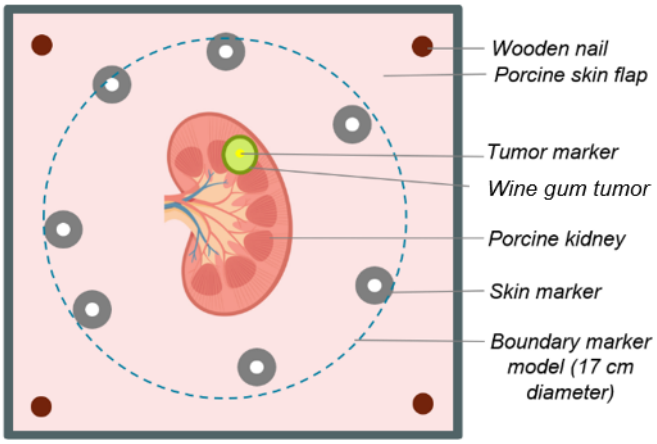

Fig. 28: Schematic topview of the set-up

Fig. 29: A schematic overview of the test set-up; In both views, the exact orientation of the kidney and the location of the agar tumors in the experiments may differ from the test set-up figure.

and tumor markers were manually selected. All coordinates were inserted in a run-table in Excel.

4) Data processing: First, for each CBCT-scan, the centroid of the marker model was calculated according to the formula mentioned in Section V-C. Consequently, for the the displacement of the centroid, the SMM, was calculated in the x-, y- and z-direction. For the marker test, the displacement of the marker closest to the insertion point and the most distant marker were calculated in the x-, y- and z-direction. Similarly, for the skin flap test, speed test and increment test, the displacement of the tumor marker, the TMM was calculated in the x-, y- and z-direction.

5) Data analysis: First, all data regarding SMM and TMM was analyzed generally. Second, the SMM and TMM were be analyzed per test. Due to the limited amount of samples per test due to time restrictions, the SMM and TMM per test were only analyzed qualitatively. No statistical analysis were be performed.

Fig. 30: Top: the interior of the PCNL box, containing a kidney with eight calyces with several embedded kidney stones and tissue surrounding the kidney (simulating the perirenal fat)[2]; Middle: the exterior of the PCNL box, including the skin flap and tube simulating the ureter [2]; Bottom: the test set up of the PCNL box in the C-arm system with the KUKA insertion robot, please note that this picture was taken of the set up in the Zenition system, whereas the actual pilot will be performed on the Azurion system.

TABLE XI: The results of the marker test, skin flap test, speed test and increment test, expressed in SMM (for the marker test, the SMM of the close and distant marker are also indicated) and TMM in the x- (dx), y- (dy) and z-direction (dz). FoV = Field of view.

Marker test	**SMM (mm)**			**M_close (mm)**			**M_far (mm)**		
	dx	**dy**	**dz**	**dx**	**dy**	**dz**	**dx**	**dy**	**dz**
Test 1	0	-0.061	-1.1	-0.49	0.49	-0.97	0	0.49	-2.92
Test 2	0.14	0.21	-0.79	0	0	-1.9	Not in FoV		
Skin flap test	**SMM (mm)**			**TMM (mm)**					
	dx	**dy**	**dz**	**dx**	**dy**	**dz**			
Thick skinflap	0	-0.12	0.39	0.49	0	0			
Thin skinflap	-0.18	0.18	0.39	0.97	1.9	-1.46			
Speed test	**SMM (mm)**			**TMM (mm)**					
	dx	**dy**	**dz**	**dx**	**dy**	**dz**			
Low speed	-0.061	0.01	0.18	1.5	-0.97	1.29			
Medium speed	0	-0.12	-0.17	-1.9	-1.9	-0.97			
High speed	-0.24	0.12	-0.24	1.46	2.43	0			
Increment test	**SMM (mm)**			**TMM (mm)**					
	dx	**dy**	**dz**	**dx**	**dy**	**dz**			
Continuous insertion	0.23	-0.19	0.49	0	0.48	-1.94			
Increment insertion	0.12	-0.12	-0.0013	1.46	-0.49	-1.46			

B. Results

In Figure 27 and 28, schematic drawings of the sideview and topview of the model which was used in the skin flap test, speed test and insertion test are presented. However, this model differs from the initially intended model. The initial plan was to inject agar gel to simulate the tumors, similar to the model developed by Baumhauer (2008) [12]. However, despite following the agar preparation protocol, the agar gel oozed out of the kidney immediately after injection, presumably due to the rigidity and dense tissue organization of the kidney. Instead of the agar tumor injection, jelly beans were used to simulate the tumor. Furthermore, the initial plan was to also fixate the tumor in agar gel, simulating the perirenal fat. However, the gel did not solidify and the gel was not homogeneous: many lumps of high agar concentrations formed and other parts of the gel were more fluid. Furthermore, a lot of agar powder had not been dissolved and had sunk to the bottom of the plastic box. Therefore, the solution was to fit a 4 *cm* thick skin flap underneath the kidney and tightly encapuslate the kidney with this skin flap, resulting in the eventual set-up. In Table XI, the results of the marker test, skin flap test, speed test and insertion test are provided. The distant marker in marker test 2 was outside the field of view of the CBCT-scan detector, disabling marker selection in dViewX, resulting in no calculated SMM for this skin marker.

C. Discussion

1) Findings: From generally analyzing the data obtained in all four pilot tests, it can be observed that in 28 cases, the calculated SMM and TMM was smaller than the size of one pixel. Therefore, it cannot be said with certainty whether the calculated displacements or lack of any displacement in those cases was due to the needle insertion or due to the limited accuracy of the selection method. Furthermore, for the marker test, it cannot be said from this one test whether the distance of the skin marker to the insertion point impacts the motion of the skin marker. Regarding the skin flap test, no dominant direction of SMM nor TMM can be distinguished. Furthermore, the differences in SMM in all directions between the thick and the thin skin flap tests are smaller than the size of a pixel, making assumptions that the skin flap thickness does not impact the SMM plausible. However, additional insertions for both skin flaps are required to confirm this assumption. A similar assumption is plausible when analyzing the SMM for the speed test and the Increment test. Lastly, although no dominant direction of motion can be distinguished for the TMM in any test, it can be seen that in the majority of the insertions, the TMM is greater than the SMM. This may be due to the fact that no large incisions are made, limiting the skin deformation.

2) Limitations: First, although the thick skin flap at the bottom of the plastic box was the best available alternative for the agar gel at the time of the pilot tests, the fixation of the kidney was sub-optimal, which may have caused the kidney to move between the skin flaps, impacting the amount of SMM and TMM. Secondly, although the jelly bean was once again the best available alternative the the agar tumors at the time of the pilot tests, the stiffness of the jelly bean tumors was relatively high, which may have over-complicated puncturing

the the jelly bean, causing the jelly bean to displace instead of being punctured, resulting in noise in the observed TMM. Third, the skin flap used at the time of the experiment was relatively stiff, requiring a deep incision at the insertion point, pre-defining the needle trajectory too much, which may have decreased the required insertion force, resulting in decreased TMM. Therefore, it is recommended to use softer skin flaps, possibly without the subcutaneous muscle layer, in future experiments. Fourth, although the skin flap in the PCNL box used in the marker test was less stiff than the porcine skin flap, the skin flap was not well fitted over the spine, resulting in the skin flap to spring back in the marker test, which may have caused the relatively high SMM in the z-direction in both marker test 1 and 2. Furthermore, the skin of the PCNL box was so elastic that the skin visibly deformed during insertion, but almost immediately moved back after insertion, causing the skin to have moved back at the time of the post-insertion CBCT-scan, despite scanning as fast as possible after the insertion. Fifth, due to the limited time resulting in a limited amount of samples, statistical analysis was not possible for the pilot experiments. An increase in samples would overcome such a limitation. Sixth, as described in Section VII-B, the selection method has both advantages and disadvantages. Lastly, the coordinates were obtained manually by one researcher, the author (MV) of this thesis, which may have resulted in bias in the calculated SMM and TMM. Furthermore, the researcher neither had prior experience with dViewX nor with manually selecting the markers. To overcome this limitation, it is recommended to let an additional independent researcher perform the data collection protocol.

D. Conclusion

Due to the limited sample size, it cannot be concluded which variable has the most impact on the SMM and/or TMM. Lastly, in most insertions, the TMM was greater than the SMM.

APPENDIX G
ARTICLE BASED ON FINAL EXPERIMENT

See next page.

The effect of needle insertion speed and level of perirenal fat on soft-tissue deformation of the kidney and skin in an ex-vivo porcine kidney model

Marlein Vogels, Master Thesis Biomedical Engineering
Faculty of 3mE, Technical University Delft, the Netherlands
Department of IGT-S Mobile Surgery Advanced Development, Philips Best, the Netherlands

Abstract*—*Purpose: **To determine the if skin markers can facilitate navigation by tracking the position of the patient in percutaneous renal ablation (PRA), information about the impact of the insertion speed (IS) and level of perirenal fat (LPF) on both the skin marker motion (SMM) and tumor marker motion (TMM) is required. Therefore, this study is aimed at investigating the effect of the IS and LPF on both the SMM and the TMM.**
Methods: **60 robotic-assisted needle insertions were planned with ClarifEye (Philips Healthcare, Best, The Netherlands) navigation and performed on 8 ex-vivo porcine kidney models with skin marker models (4 with low perirenal fat level (LLPF), 4 with high perirenal fat level (HLPF)), targeting 20 tumors at varying ISs: continuous insertions of 2.5 mm/s, 75 mm/s and consecutive 5 mm increments of 10 mm/s. Cone beam computed tomography (CBCT-)scans were made before and after insertion to analyze the SMM and TMM. A two-way ANOVA test was performed to assess the main effects of the IS and LPF and the interaction effect between the IS and LPF.**
Results: **No significant differences were found in both the mean SMM euclidean distance (SMM ED), mean TMM euclidian distance (TMM ED) and TMM in the z-direction (TMM_z) regarding both the IS and the LPF ($p_{SMM\ ED\ IS}$ = 0.211, $p_{SMM\ ED\ LPF}$ = 0.907, $p_{TMM\ ED\ IS}$ = 0.826, $p_{TMM\ ED\ LPF}$ = 0.440, $p_{TMM_z IS}$ = 0.202, $p_{TMM_z\ LPF}$ = 0.164). Furthermore, in both the mean SMM ED, TMM ED and TMM_z, no significant interaction effects were observed in the two-way ANOVA (p = 0.559, p = 0.833 and p = 0.585, respectively).**
Conclusion: **The results suggest that the IS and LPF do not impact the SMM and TMM.**

***Index Terms*—Ablation, fiducial markers, insertion speed, navigation, perirenal fat, skin markers**

I. Introduction

A. Rationale

1) Percutaneous renal ablation as a non-invasive RCC treatment: Renal Cell Carcinoma (RCC) accounts for over 80% of all renal malignancies with a worldwide incidence of 431288 (Worldwide cancer statistics, 2020) [1], [9], [23], [24], [30] and is the most lethal urological malignancy with a mortality rate of 35-50% [4], [20], [21], [30]. Due to the increased detection of small, localised, early-stage RCCs [5], [9], [12], [13], [19], [23], [29], [30] (over 50% of the RCC detections are incidental [9], [30]), which can be curable [9], [24], [30], and recurrence rate of RCC [9], [23], [24], [30], [39], more resource efficient and less invasive (nephron sparing) treatments are required. Therefore, PRA is applied more and more, as the best clinical outcomes of PRA are reported in tumors with a diameter smaller than 30 to 40 mm [8], [20], [24], [26]. However, a PRA procedure is not without challenges: is essential that the needle is inserted so that the tumor is reached successfully, while preventing complications such as bleeding or touching critical structures. Ablating too much healthy tissue and missing any tumor tissue should be avoided. However, target motion is known to be a dominant factor of disturbance in accurate targeting and successful PRA [18], especially since the target is not directly visible to the technician, as opposed to open surgical procedures. The limited high resolution real-time visualization possibilities of the target (and surrounding critical structures) in combination with the target motion require a suitable navigation strategy, overcoming the challenges in PRA. Four studies [2], [10], [15], [28] have used external (skin) markers to track the patient and/or probe motion in renal percutaneoous needle procedures (PNPs). However, it was found that, in order to determine the suitability of a skin markers to track patient motion in PRA, fundamental research about the tissue motion due to needle insertion is desired [34].

Needle insertions are known to cause skin deformation [22], which may result in skin marker motion (SMM) without changes in the position of the patient. Furthermore, the needle insertions may cause tumor motion (TM). Needle insertion speed (IS) is known to be related to the needle insertion forces and insertion accuracy [36] and can be controlled by the physician. Although the relation between needle IS and soft tissue deformation has been identified [33], [35], no research specifically exploring the relationship between needle IS and TM has been performed. Furthermore, perirenal fat is assumed to have a mobilizing effect on the kidney, causing TM in patients with a higher level of perirenal fat (LPF). However, no research exploring this relationship has been performed.

B. Research questions

This thesis is aimed at investigating the effect of the IS and LPF on both the SMM and the TMM. Therefore, the overarching research question of this thesis is: *what is the effect of the insertion speed and level of perirenal fat on both the skin marker motion and the tumor motion?*

II. Methods

A. Study set-up: ex-vivo kidney preparation

Needle insertions were performed on an ex-vivo porcine kidney model in the Rami Nachabé lab (a non-clinical lab at Philips Medical Systems B.V., Best, The Netherlands) on the 19-20 of April 2023. An ex-vivo porcine kidney was used (weighing approximately 200 grams) to simulate the human kidney, because porcine kidneys are most similar in size and texture, both elasticity and tissue feeling, to human tissue [7], [38]. The collecting system of the kidney was preserved to assure representative encapuslation of the to be inserted tumors. The renal capsule was also preserved, as puncturing the renal capsule is assumed to cause kidney displacement and therefore cause TM. Second, to simulate and explore TM during needle insertion, three approximately spherical wine gum tumors (average diameter: 8 *mm*) were inserted into the porcine kidney. Wine gum tumors are assumed suitable to simulate kidney tumors, as wine gums approximate the hardness of real tumor tissue, which is significantly harder than healthy kidney tissue [27], [33], [37]. To track the position of the tumor, a metal fiducial marker (1.6 *mm* in diameter) was inserted into the center of the tumor with a 16-G Jamshidi needle (ClarifEye Needle, Philips Healthcare, Best, The Netherlands), while avoiding tumor rupturing. As a result, the position of the tumor center can be deduced from X-ray/CBCT- images without using contrast fluid. The displacement of the tumor marker will be referred to as tumor marker motion (TMM). Each tumor was inserted through a lateral kidney incision (maximum width: 5 *mm*, depth: 10-20 *mm*) to preserve the kidney's ventral and dorsal surface. The three tumors were inserted in the superior, middle and inferior region of the renal cortex. To enclose the tumors, the incisions were glued, while avoiding glue to stick to the tumors. Third, to represent the perirenal fat, the kidney was fixated in a gelatin gel (5% weight), approximating the hardness of the perirenal fat surrounding the kidney. Fourth, to simulate skin deformation and explore SMM during insertion, a porcine skin flap, including subcutaneous fat of 3-4 *mm* in thickness and 21-16 *cm* in size was pressed over the fixated kidney and secured by wooden nails, resembling the human skin, serving as the basis for the skin marker model. The most elastic porcine skin flaps available were selected to best approximate the stiffness of in-vivo human skin. The porcine kidney model was tightly fitted in a plastic basket of 21x16x9 (length x width x height) *cm* in size.

To track the position of the kidney model and possibly detect skin deformations caused by the needle insertions, a marker model consisting of 8 spherical fiducial hybrid skin markers (which are recognized by the navigation system and visible on X-Ray/CBCT-images, radio-opaque diameter: 3.16 *mm*) was constructed (see Figure 2). A circular yet asymmetric configuration of the markers was pursued with a maximum diameter of 17 *cm* fitting over the entire kidney surface, ensuring both the marker model and entire kidney are fit in the field of view (FoV) of the C-arm.

To gain information about the position of both the tumors and skin markers, the experiment was conducted in the Azurion C-arm system (Philips Healthcare, Best, The Netherlands). The Azurion C-arm system acquires 3D CBCT-images and is equipped with the desired ClarifEye navigation technology (Philips Healthcare, Best, The Netherlands): an AR surgical navigation system, which tracks the skin marker model to track the position of the patient [31]. The Azurion C-arm system was re-calibrated before the start of the experiment and the position of the model in the system was validated by one supervisor, as the detector should be free to move around the insertion equipment and the kidney model (and the kidney model, with all skin markers, must be within the FoV). A robotic 7-degrees-of-freedom arm (LBR iiwa, KUKA GmbH, Germanny; referred to as KUKA) was used to perform insertions at predefined IS levels, depths and direction and to position the ablation needle at the planned position and in the planned orientation. The used settings of KUKA will be elaborated below. All insertions were performed with a 13-G ablation needle (Emprint™ Percutaneous, Antennas - 25 *cm*, Medtronic-Covidien, Minneapolis, United States). In Figure 1, an overview of the study set-up is provided. The experiment was performed at room temperature.

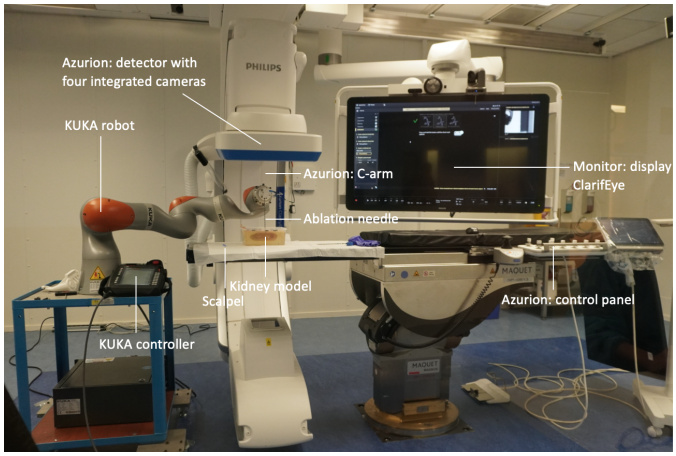

Fig. 1: An overview of the study set-up. The kidney model is taped onto an anti-slip cover, which is taped to the table of the Azurion system.

B. Experimental design

1) Experimental Conditions (ECs): To test the impact of IS on the SMM and TMM, insertions were performed at low speed (LS: 2.5 *mm/s*), high speed (HS: 75 *mm/s*) and 5 *mm* increments (IC) of 10 *mm/s*) (see Table I). The LS level was defined based on Barua et al. [3], Van Dommele [32], Lin and Lan [16], Wang et al. [36], reporting IS values in PNPs in soft tissue of respectively (3 *mm/s*), (2.5 *mm/s*), (2 *mm/s*) and (1.5 *mm/s*). The HS level was based on an estimation of the maximum feasible ISs that can be reached in clinical practice in especially manually performed PNPs. Insertion in IC was added as third IS level, because RCCs are often targeted in IC in clinical practice. Although the IS in the increment level was

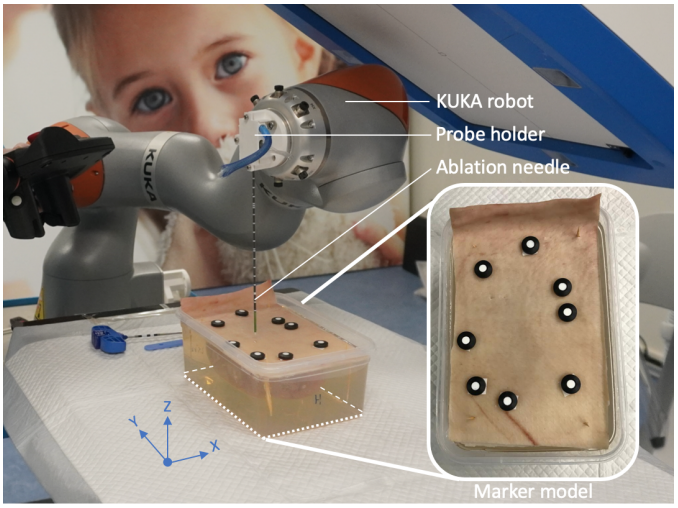

Fig. 2: A close-up of the study set-up, including a close-up picture of the marker model. The markers are taped to the porcine skin to prevent slipping. The coordinate system is based on the coordinate system from the y-plane of dViewX (the dicom-viewer software that was used for the CBCT-analysis).

defined, this speed was never reached within the 5 *mm*, due to KUKA's limited acceleration. In all levels, the acceleration to reach the IS was at KUKA's maximum level. To test the impact of the amount of perirenal fat on the SMM and TMM, insertions were performed in both kidney models with a LLPF, in which the kidney is fixated on a base of 100 *mL* of gelatin, and kidney models with a HLPF, in which the kidney is fixated on a base of 750 *mL* of gelatin, representing a professional athlete and an obese person [27] (see Table I and Figure 3).

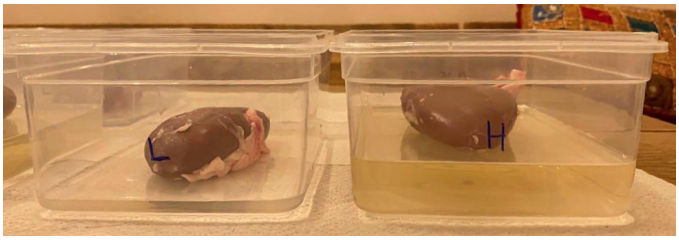

Fig. 3: Left: the gelatin base for an LLPF kidney model; right: the gelatin base for an HLPF kidney model. The gelatin fixating the sides and top of the kidney and the porcine skin are not displayed in this figure.

TABLE I: Condition Matrix displaying the six Experimental Conditions (ECs).

		LPF	
	$N_{total} = 60$	LLPF	HLPF
IS	Low speed (2.5 *mm/s*)	EC_{11}	EC_{12}
	High speed (75 *mm/s*)	EC_{21}	EC_{22}
	Increments (5 *mm* at 10 *mm/s*)	EC_{31}	EC_{32}

To estimate the experimental error (EE), a sample size of 10 was intended for each EC, resulting in a total of 60 experimental units (EU). Instead of randomly assigning the ECs to the 60 EUs, which was too labor-intensive and required an unworkable file-saving strategy, insertions were alternately (after targeting three lesions, the model was replaced) performed in the low fat and high fat models. Furthermore, each lesion was targeted once at LS, HS and in IC in alternating order to cope with any possible SMM and/or TMM caused by previous insertions. Therefore, eight kidney models were prepared (four LLPF models for EC_{11} - EC_{31} and four HLPF models for EC_{12} - EC_{32}), each with three[1] tumors. Targeting multiple tumors per EC instead of performing many insertions on one lesion is assumed to increase the reliability of the results and prevent "over puncturing" of both the skin and the tumor.

2) Phases per EU: To identify the tumor's location, a CBCT-scan was made. Based on this CBCT-scan, the shortest possible needle trajectory was planned in ClarifEye (Philips Healthcare, Best, The Netherlands). Interference of the path with any previously performed insertions was avoided, as interference is assumed to influence the SMM and TMM due to a decrease in friction in previously formed paths. Furthermore, the insertion point was always within the area of the marker model, ensuring the insertion path is in the field of view. Lastly, the minimal distance between any skin marker and the insertion point was 2 *cm*, preventing obstruction of the insertion by the markers and allowing working space for making any incisions without touching the markers. For consequent insertions targeting the same lesion, the insertion depth must be: primary insertion depth $\pm$ 10 *mm*. The insertion angle was disregarded, as the KUKA robot limits the insertion angle range. After positioning the ablation needle at the planned entry point assisted by the bullseye view projected on the target in the ClarifEye application, an incision of 0-3 *mm* wide and 0-3 *mm* deep was made with a scalpel to prepare the insertion. Consequently, the ablation needle was aligned, matching the orientation with the planned path. A CBCT-scan was made to identify the initial position of both the skin markers and the tumor marker right before insertion. Consequently, the needle was inserted at the appropriate insertion depth and speed, considering the assigned EC. Lastly, a CBCT-scan was made after insertion/per increment to determine SMM and TMM. In this experiment, the skin markers are only used to determine the SMM based on the CBCT-scans.

C. Data collection and data exportation

The CBCT-scans were imported to dViewX (dicom-view software, Philips Healthcare, Best, The Netherlands). Consequently the center of the skin markers, tumor markers and the needle tip were manually selected in 'zoomed in mode'. The voxel measurement of the CBCT-scans is 0.485 *mm* (in the x-, y- and z-direction), the voxel measurement of the 'zoom in mode' (VMZ) of dViewX is 0.2425 *mm* (in the x-, y-, and z-direction), allowing selecting a position within the CBCT-voxel. dViewX provided Cartesian coordinates of the selected

[1]A margin of two tumors was used in case a tumor insertion failed

dViewX voxels with an accuracy of 0.01 *mm*. In most cases, the coordinates were obtained in the y-plane of dViewX. If the visibility of a tumor marker was limited, for instance due to overlap with the needle tip, an additional plane was used as a check. All coordinates were inserted a run-table in Excel.

D. Data processing

As elaborated in Section I, the dependent variables in this experiment are the SMM and TM (in this study expressed in TMM). In this study, SMM was expressed in *the displacement vector of the centroid of the marker model*.

For each CBCT-scan the centroid (C) of the obtained skin marker coordinates was calculated with:

$$C = \left(\frac{x_1 + ... + x_n}{n}, \frac{y_1 + ... + y_n}{n}, \frac{z_1 + ... + z_n}{n} \right),$$

where n stands for the total amount of segmented skin markers. Consequently, the SMM was calculated with:

$$SMM = [(x_{C_{end}} - x_{C_{start}}), (y_{C_{end}} - y_{C_{start}}), (z_{C_{end}} - z_{C_{start}})]$$

Lastly, the Euclidean distance (ED) of the SMM (SMM ED) was calculated. Similarly, the TMM and ED of the TMM (TMM ED) and $\text{TMM}_{non-target}$ ED were calculated. To further interpret the SMM and TMM values: the displacement of the needle tip in the x-, y-, and z-direction was obtained via: $N = [(x_{N_{end}} - x_{N_{start}}), (y_{N_{end}} - y_{N_{start}}), (z_{N_{end}} - z_{N_{start}})]$. To examine the accuracy of the insertion, the needle to target distance (NTD) was obtained via: $NTD = \sqrt{(x_n - x_{tumor})^2 + (y_n - y_{tumor})^2 + (n_C - z_{tumor})^2}$.

All outcomes were calculated in the run-table in Excel.

E. Data analysis

The run-table was imported to SPSS for data-analysis. First, the mean, median, standard deviation (SD) and standard error (SE) were calculated for the SMM ED, TMM ED, TMM in the z-direction (TMM_z), and NTD ED per EC and combinations of ECs. Consequently, normality of the datasets was checked by plotting a histogram of the data and visually comparing the histogram with a standard bell curve. A two-way ANOVA (factorial design analysis of variance) was performed to assess the effect of each independent variable (IS and LPF) on one continuous dependent variable (SMM ED, TMM ED, TMM in the z-direction, and NTD ED) and to check possible interactions between the IS and LPF. The predetermined significance level was 0.05. To account for inequalities in sample size per EC, the two-way ANOVA in SPSS was set to add unweighted harmonic total averages to the ECs with smaller sample sizes. Lastly, the correlations between the TMM ED and SMM ED, TMM ED and NTD ED, and TMM in the z-direction and NTD ED were obtained via bivariate correlation analysis. All figures displayed in this study were created in SPSS.

III. Results

A. Raw data

Regarding the sample size, one sample (EU: 14) was excluded from data analysis, because the table of the Azurion system has moved during the insertion. A histogram of all measurements regarding SMM ED, TMM ED, TMM_z and NTD ED showed an almost normal distribution.

B. Processed data

1) SMM: In Figure 4, a boxplot of the the SMM in the x-, y- and z-direction (SMM_x, SMM_y and SMM_z) is provided for all ECs. The mean SMM in all directions is close to zero and all standard deviations (SD) values (except the LS, HLPF SD of 0.28 *mm*) are smaller than the VMZ. Visually, no dominant insertion direction can be distinguished. Furthermore, most SMM vales are smaller than the VMZ. One cross-over and no parallel lines can be seen in Figure 5, displaying the effect plot of the SMM ED for all ECs.

2) TMM: Figure 6 presents an overlay of a CBCT-slice in the x-plane (imported in dViewX) before and after insertion, showing typical TMM predominantly in the z-direction. Additionally, the NTD (in the x-plane) is indicated. Figure 7 shows a boxplot of of the TMM in the x-, y- and z-directin (TMM_x, TMM_y and TMM_z) for all ECs. In Figure 9, a boxplot of the TMM ED is presented for all ECs. Whereas the mean TMM_x and TMM_y are close to zero in all ECs, the mean TMM_z is predominantly negative (mean TMM_z = -0.96 *mm* $\pm$ 0.85 *mm*). Secondarily, the boxplot of the displacement of the needle tip in the x-, y- and z-direction (Tip_x, Tip_y and Tip_z) for all ECs shows that the dominant insertion direction is the z-direction and all Tip_z values are negative (see Figure 8). All Tip_y values are around zero, as all insertions were planned in the transversal plane. The boxplot of the SMM ED and TMM ED for all ECs shows that the mean TMM ED is larger than the mean SMM ED for all ECs (see Figure 9). Lastly, Figure 10 and 11 display the effect plots of TMM ED and and TMM_z for all ECs.

C. Statistical tests and correlations

No significant differences in mean SMM ED were observed regarding IS (p = 0.211) and LPF fat (p = 0.907). The two-way ANOVA showed that the observed interaction effect in Figure 5 is not significant (p = 0.559). Similarly, no significant differences in mean TMM ED regarding the IS (p = 0.826) and the LPF fat (p = 0.440) and TMM in the z-direction regarding IS (p = 0.202) and LPF fat (p = 0.164) were observed. Furthermore, the two-way ANOVA showed that the observed interaction effects in Figure 10 and 11 are not significant (p = 0.833 and p = 0.585, respectively). Secondly, the mean TMM ED was significantly larger than the mean $\text{TMM}_{non-target}$ ED (1.5 *mm* vs. 0.35 *mm*, $p < 0.001$). Negligible, insignificant correlations were found between the SMM ED and TMM ED (r = -0.128), TMM ED and NTD ED (r = -0.203) and TMM_z and NTD ED (r = -0.029).

D. Remarkable observations

First, for the insertion in increments, most TMM was observed in in the last increments, approaching the tumor.

Second, between most insertions targeting the same tumor (e.g. EU 43-45, 46-48, 49-52, 57-60) it was observed in the

CBCT-analysis that the tumor returned to its position before insertion. In some insertions (e.g EU 28-30), on the other hand, the tumor systemically moved in the direction of the insertion and did not fully return to its initial position.

Third, in insertions with an NTD smaller than approximately two voxel distances, it was noticed that the needle tip and tumor could not be distinguished on during the CBCT-analysis in dViewX. As a result, the NTD ED after 9 insertions (EU: 15, 20, 22, 29, 32, 35, 52, 55 and 57) is 0 *mm*.

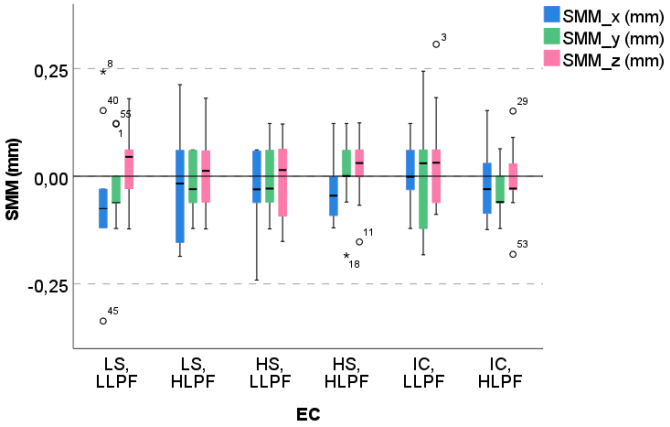

Fig. 4: Boxplot of the SMM in the x-, y- and z-direction (*mm*) by EC. LS = low speed, HS = high speed, IC = increments, LPF = low level of perirenal fat, HPF = high level of perirenal fat. The dotted lines indicate the accuracy of the coordinate selection in dViewX (0.2425 *mm* rounded up to 0.25 *mm*).

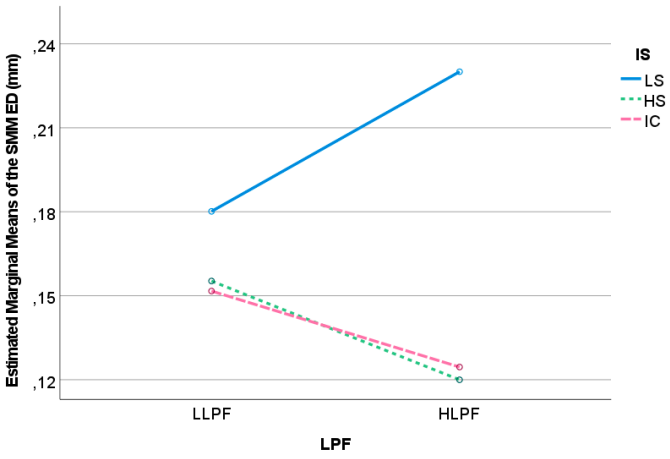

Fig. 5: Effect plot of the SMM ED (*mm*).

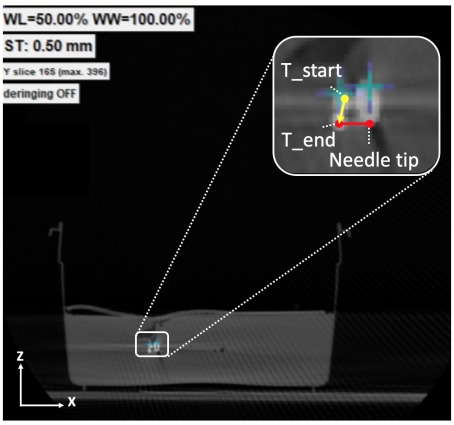

Fig. 6: An overlap of a CBCT-slice in the x-plane (in dViewX) before and after insertion. The dominance of the overlap of both CBCT-slices is 50%. The yellow arrow indicates the target TMM. In this EU, the TMM in the y-direction was 0.00 mm. Therefore, in each CBCT, the same slice was used. The red line indicates the NTD in the x-plane.

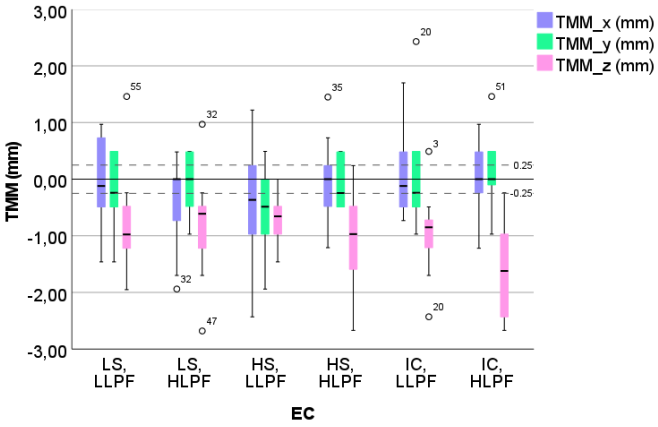

Fig. 7: Boxplot of the target TMM in the x-, y- and z-direction (*mm*) (TMM$_x$, TMM$_y$, TMM$_z$, respectively) by EC. The dotted lines indicate the accuracy of the coordinate selection in dViewX (0.2425 *mm* rounded up to 0.25 *mm*).

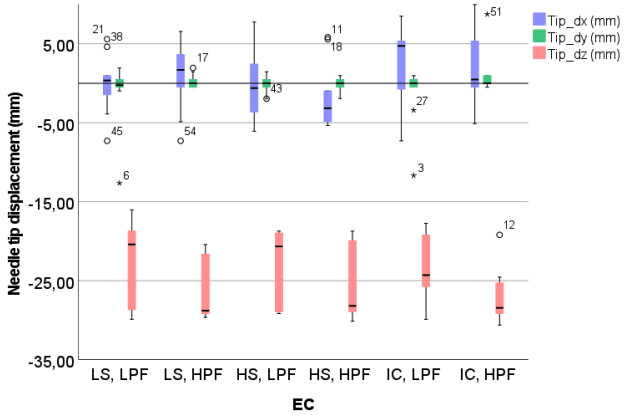

Fig. 8: Boxplot of the needle tip displacement in the x-, y- and z-direction (*mm*) (Tip$_x$, Tip$_y$, Tip$_z$, respectively) by EC.

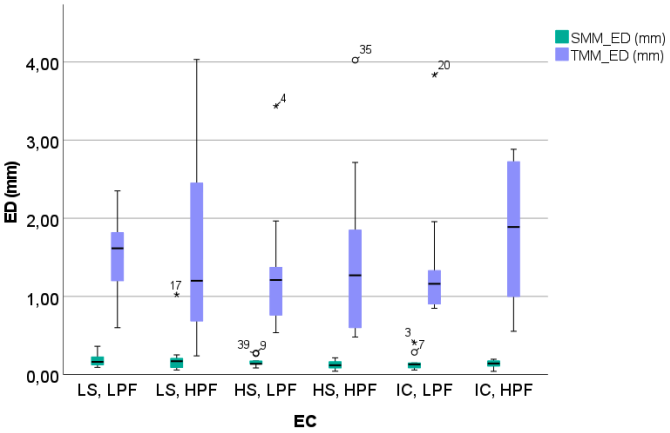

Fig. 9: Boxplot of the SMM ED (*mm*) and the target TMM ED (*mm*) by EC.

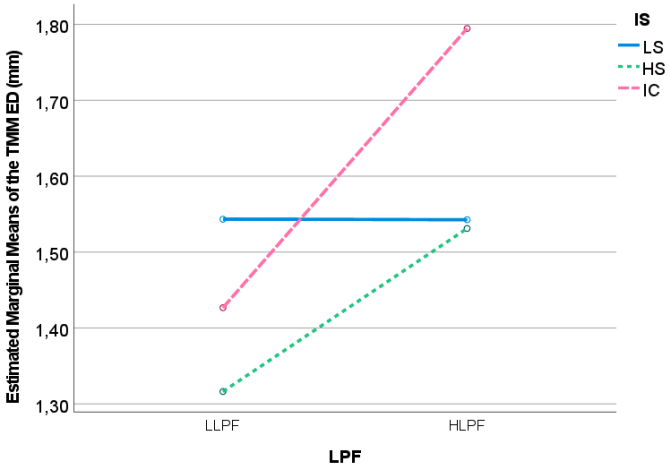

Fig. 10: Effect plot of the target TMM ED (*mm*).

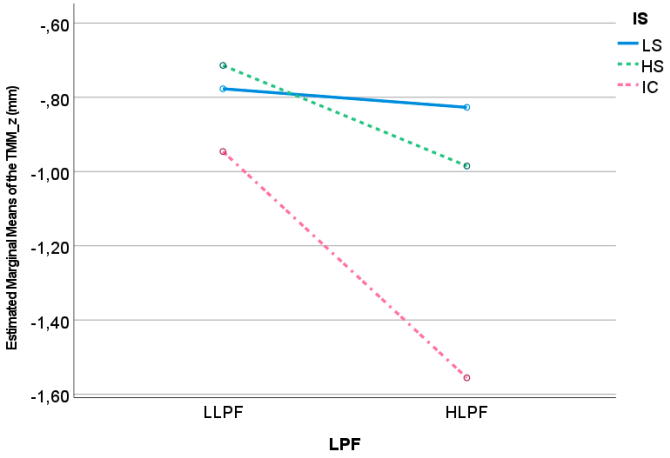

Fig. 11: Effect plot of the TMM in the z-direction (*mm*).

IV. Discussion

A. Findings

This aim of this research was to investigate the effect of the IS and LPF during needle insertion on both the SMM and the SMM. No significant differences in both the SMM ED and TMM ED regarding both the IS and LPF. Additionally, no significant interaction effects between the IS and LPF were found in both the SMM and TM.

1) Insertion accuracy: Although the objective of the insertions was to observe the SMM and TMM caused by needle insertions and not to minimize the NTD, for instance by re-manoeuvring the ablation needle, clinically representative NTD values are desired for representative SMM and TMM values. Furthermore, the TMM may be influenced when the ablation needle punctures the tumor, corresponding with smaller NTD values. In this experiment, the insertion accuracy (NTD) in robotic insertions is influenced by: the accuracy of the planning of the needle path, the accuracy of the navigation towards the planned insertion point, the accuracy of the alignment with the planned needle orientation and the accuracy of the KUKA's insertion precision, and any possible needle deflection occurring during needle insertion (KUKA cannot control the needle deflection). The accumulation of all factors resulted in a mean NTD of 2.0 - 4.3 *mm* (SD = 1.7 - 2.6 *mm*), depending on the EC, and an overall mean NTD of 3.2 $\pm$ 2.1 *mm*. However, the two-way ANOVA results imply that neither the IS nor the LPF has had a significant impact on the NTD. The insertion accuracy reached in this experiment was comparable to reported insertion accuracy values in Maier-Hein et al. [17] (mean NTD = 2.8 - 4.5 *mm*, SD = 1.4 - 2.7 *mm*), in which both novices and experts performed manual CT-guided needle insertions in liver tumors. De Baere et al. [6] performed CT-guided robotic insertions on a fiducial in the kidney of an in-vivo swine, resulting in an mean NTD of 2.8 *mm* (SD = 1.8 *mm*). Hiraki et al. [11] reported a comparable mean NTD of 2.8 mm (SD = 0.8 *mm*) for a comparable experiment, targeting a fiducial in the kidney, performed with the same ablation needle as this thesis' ablation probe. Although the NTD values in this experiment resonate with the reported insertion accuracies above, no studies reporting insertion accuracy values in renal ablation were found. However, the majority of the NTD values in this experiment is within both the ablation zone margin of 5 *mm* around the tumor and the usual required clinical insertion accuracy margin of 3-5 *mm* [33], implying clinically representative NTD values.

2) SMM: For all ECs, the mean SMM values close to zero in all directions is close to zero implying no dominant positive or negative displacements. The results from the two-way ANOVA test imply that the IS and LPF do not impact the SMM. However, with the exception of three SMM values, all SMM values are smaller than the VMZ, 0.25 *mm*. Therefore, the results of the SMM must be interpreted with caution. On the other hand, as 98% of the SMM values are $<$ 0.25

mm, it is plausible that the general SMM motion caused by needle insertion forces has been negligible in this experiment. Furthermore, this study observed the motion of the marker model based on the centroid displacement. Therefore, the fact that the calculated SMM in this study is close to 0 *mm* does not necessarily imply that none of the skin markers has displaced individually during needle insertion.

3) TMM: The boxplot in Figure 7 shows that, as opposed to the TMM_x and TMM_y values, the observed TMM_z values were predominantly negative (mean TMM_z = -0.96 *mm* $\pm$ 0.85 *mm*). An explanation for the downward TMM could be that the tumor tends to move in the axial insertion direction. The results of the two-way ANOVA test imply that neither the IS nor the LPF impact the TMM. It was hypothesized that a higher LPF would allow the kidney to rotate during insertion, causing not only TMM of the target tumor, but also causing TMM of the non-target tumors. However, the mean TMM ED of the target tumor was significantly larger than the mean TMM ED of the non-target tumors (1.5 *mm* vs. 0.35 *mm*, $p < 0.001$), supporting the results of the two-way ANOVA test that the LPF has not influenced the TMM. Thirdly, no correlation was found between the TMM ED and NTD ED (r = -0.203), implying that the insertion accuracy does not impact the TMM. Fourthly, it should be mentioned that 33% of the calculated TMM values in the x-, y-, and z-direction were equal to the VMZ of 0.2425 *mm* or equal to zero. TMM values of zero can be caused by a small unavoidable bias in the manual coordinate selection or by the limited measuring accuracy, if the actual TMM was between 0 and 0.2425 *mm*. Due to the bias in manual marker selection, a TMM of 0 *mm* can be falsely classified as a TMM value of 0.24 *mm* (or 0.25 *mm*, depending on the rounding). Therefore, any displacements smaller than the size of one pixel should be interpreted with caution.

B. Limitations

First, some limitations regard to the used kidney model. The main model limitation regarding the TMM values and the consequent relevance of the two-way ANOVA results is the fact that only one tumor type was simulated in the kidney model, whereas RCCs greatly differ in size, texture, shape and heterogeneity. Therefore, the question if the IS and LPF impact the TMM of different tumors remains. Similarly, one average perirenal fat simulation was used. However, the perirenal fat differs per patient in elasticity and is usually less homogeneous than the gelatin. Therefore, the TMM caused by needle insertion may be different in other perirenal fat simulations. Furthermore, the questions if the LPF impacts the TMM caused by needle insertion for other perirenal fat simulations remains. Similarly, only one type of porcine skin flaps (the softest available skin flaps) was used during the experiment, best approaching the elasticity of human skin. However, the stiffness of the skin greatly differs between patients. Therefore, the questions to what extent the local deformation caused by needle insertions is translated into SMM in more or less elastic skin types and if skin markers can be used in other skin types remains.

Second, although the Azurion system, equipped with ClarifEye technology, was instrumental in performing the insertions and obtaining the positions of the skin markers and tumor markers, some limitations in this study regard to the system and technology used. For instance, the current software configuration of ClarifEye only allows planning needle paths up to 5 *mm* accuracy (path lengths of 5, 10, 15 *mm* etc.), which is lower than the desired path planning accuracy of 1 *mm*, resulting in less accurate needle insertions and an increased NTD values and possible under- and overshooting of the target. Furthermore, although CBCT-scans were performed immediately before and after insertion, Azurion's CBCT-scans cannot provide real-time imaging of SMM and TMM. Also, despite the re-calibration of the Azurion system before the experiment, a registration error, of which the magnitude is unknown, cannot be avoided. Moreover, an unavoidable delay in tracking of approximately 0.5 seconds complicated directing KUKA to navigate the ablation needle to the desired insertion point and orientation, which may have impacted the accuracy of the positioning and alignment of the ablation needle, increasing the NTD. Third, performing robotic-assisted insertions allowed for regulation of the IS and insertion depth. However, some experimental limitations are indeed regarded to the use of KUKA. For instance, it was not possible at the time of performing the experiment for KUKA to measure the insertion forces, even though the detection of any possible force peaks in the insertion force may have been useful in assessing whether a tumor has been punctured and the insertion force is known to be related to soft-tissue deformation [14]. Furthermore, the robotic insertions disabled re-manoeuvring of the ablation needle during insertion to account for intermediate TMM, decreasing the NTD ED. Also, the use of KUKA, which contains metal components, resulted in the occurrence of beam hardening artefacts on the CBCT-scans, sometimes visually complicating the marker and needle tip segmentation. Fourth, while preparing the tumors it was observed that the fiducial was not moving while compressing the tumor and that it was challenging for a needle to move the fiducial. However, no contrast was used in this study, making the edges of the tumor invisible on the CBCT scans. As a result, the TMM caused by motion of the fiducial marker within the tumor or caused by actual TM could not be distinguished in this study. Therefore, it is recommended to enhance the tumors with contrast fluid in future studies. Lastly, despite the fact that the manual selection control supported used marker selection method, some limitations regard the coordinate selection. For instance, the accuracy of the selection was the size of one dVievX voxel, whereas the accuracy of the automated coordinate selection calculates the center of markers with a sub-voxel accuracy. Furthermore, in insertions with a greater accuracy (smaller NTD), it was more challenging to select the target tumor marker due to overlap of the fiducial with the blurry needle tip, which may have resulted in a less accurate NTD ED calculation in more accurate insertions.

C. Future research

First, several future research recommendations regard the used kidney model. First, due to the varying RCC characteristics [25], [27], it is recommended to vary the types of tumors in the kidney model in terms of size, homogeneity, hardness and location to see how the impact of the IS and LFP on the TMM varies per tumor type. Moreover, as mentioned in Section IV-B, contrast should be added to the tumors. Furthermore, due to the varying perirenal fat characteristics [27], it is recommended to vary the types of kidney fixation material in terms volume, simulating the LPF, homogeneity, as some patients have more nodular perirenal fat than others, and stiffness [27]. However, to approach the real elasticity of perirenal fat, future research investigating the elasticity of perirenal fat is first required. Lastly, as the stiffness of skin greatly varies between patients [25], it is recommended to vary the types of skin in terms of stiffness to see how the IS impacts different types of skin. Second, the possibilities for real-time 3D imaging to perform experiments with a similar set-up and design should be explored. For instance, the cameras integrated in the detector of the C-arm may be used to record real-time SMM.

V. Conclusion

This experiment suggests that neither the IS nor the LPF impact the SMM. Similarly, this experiment suggests that neither the IS nor the LPF impact the TMM. Furthermore, this study suggests that the IS and LPF do not interact with each other, considering both the SMM and TMM.

References

[1] Kidney cancer statistics, 2020.

[2] Rakkunedeth H. Abhilash and Sunita Chauhan. Respiration-induced movement correlation for synchronous noninvasive renal cancer surgery. *IEEE Transactions on Ultrasonics, Ferroelectrics and Frequency Control*, 59:1478–1486, 7 2012. Web of Science.

[3] Ranjit Barua, Surajit Das, Sudipto Datta, Pallab Datta, and Amit Roy Chowdhury. Study and experimental investigation of insertion force modeling and tissue deformation phenomenon during surgical needle-soft tissue interaction. *Proceedings of the Institution of Mechanical Engineers, Part C: Journal of Mechanical Engineering Science*, 237:1007–1014, 3 2023.

[4] Neil Bannister Broggio and John. Cancer survival by stage at diagnosis for england (experimental statistics): Adults diagnosed 2012, 2013 and 2014 and followed up to 2015, Jun 2016.

[5] Wong-Ho Chow. Rising incidence of renal cell cancer in the united states. *JAMA*, 281:1628, 5 1999.

[6] Thierry de Baere, Charles Roux, Guillaume Noel, Alexandre Delpla, Frederic Deschamps, Eloi Varin, and Lambros Tselikas. Robotic assistance for percutaneous needle insertion in the kidney: preclinical proof on a swine animal model. *European Radiology Experimental*, 6:13, 12 2022.

[7] Pedro P. de Sá Earp. Percutaneous renal surgery: new model for learning and training. *International braz j urol*, 29:151–154, 4 2003.

[8] N. Reed Dunnick. Renal cell carcinoma: staging and surveillance. *Abdominal Radiology*, 41:1079–1085, 6 2016.

[9] B. Escudier, C. Porta, M. Schmidinger, N. Rioux-Leclercq, A. Bex, V. Khoo, V. Grünwald, S. Gillessen, and A. Horwich. Renal cell carcinoma: Esmo clinical practice guidelines for diagnosis, treatment and follow-up. *Annals of Oncology*, 30:706–720, 5 2019.

[10] Nobuhiko Hata, Sang-Eun Song, Olutayo Olubiyi, Yasumichi Arimitsu, Kosuke Fujimoto, Takahisa Kato, Kemal Tuncali, Soichiro Tani, and Junichi Tokuda. Body-mounted robotic instrument guide for image-guided cryotherapy of renal cancer. *Medical Physics*, 43:843–853, 1 2016. Web of Science¡br/¿.

[11] Takao Hiraki, Takayuki Matsuno, Tetsushi Kamegawa, Toshiyuki Komaki, Jun Sakurai, Ryutaro Matsuura, Takuya Yamaguchi, Takanori Sasaki, Toshihiro Iguchi, Yusuke Matsui, Hideo Gobara, and Susumu Kanazawa. Robotic insertion of various ablation needles under computed tomography guidance: Accuracy in animal experiments. *European Journal of Radiology*, 105:162–167, 8 2018.

[12] John M. Hollingsworth, David C. Miller, Stephanie Daignault, and Brent K. Hollenbeck. Rising incidence of small renal masses: A need to reassess treatment effect. *JNCI: Journal of the National Cancer Institute*, 98:1331–1334, 9 2006.

[13] Mary Jayson and Holt Sanders. Increased incidence of serendipitously discovered renal cell carcinoma. *Urology*, 51:203–205, 2 1998.

[14] Yo Kobayashi, Akinori Onishi, Hiroki Watanabe, Takeharu Hoshi, Kazuya Kawamura, Makoto Hashizume, and Masakatsu G. Fujie. Development of an integrated needle insertion system with image guidance and deformation simulation. *Computerized Medical Imaging and Graphics*, 34:9–18, 1 2010.

[15] Zhi-Cheng Li, Kai Li, Hai-Lun Zhan, Ken Chen, Jia Gu, and Lei Wang. Augmenting intraoperative ultrasound with preoperative magnetic resonance planning models for percutaneous renal access. *BioMedical Engineering OnLine*, 11:60, 2012. Pubmed.

[16] Chi-Lun Lin and Guan-Jhong Lan. A computational approach to investigate optimal cutting speed configurations in rotational needle biopsy cutting soft tissue. *Computer Methods in Biomechanics and Biomedical Engineering*, 22:84–93, 1 2019.

[17] Lena Maier-Hein, Aysun Tekbas, Alexander Seitel, Frank Pianka, Sascha A. Müller, Stefanie Satzl, Simone Schawo, Boris Radeleff, Ralf Tetzlaff, Alfred M. Franz, Beat P. Müller-Stich, I. Wolf, H.-U. Kauczor, B. M. Schmied, and H.-P. Meinzer. ¡i¿in vivo¡/i¿ accuracy assessment of a needle-based navigation system for ct-guided radiofrequency ablation of the liver. *Medical Physics*, 35:5385–5396, 11 2008.

[18] Pedro Moreira, Momen Abayazid, and Sarthak Misra. Towards physiological motion compensation for flexible needle interventions. In *2015 IEEE/RSJ International Conference on Intelligent Robots and Systems (IROS)*, pages 831–836, 2015.

[19] Mike M. Nguyen, Inderbir S. Gill, and Lars M. Ellison. The evolving presentation of renal carcinoma in the united states: Trends from the surveillance, epidemiology, and end results program. *Journal of Urology*, 176:2397–2400, 12 2006.

[20] Phillip M. Pierorazio, Michael H. Johnson, Hiten D. Patel, Stephen M. Sozio, Ritu Sharma, Emmanuel Iyoha, Eric B. Bass, and Mohamad E. Allaf. Management of renal masses and localized renal cancer: Systematic review and meta-analysis. *Journal of Urology*, 196:989–999, 10 2016.

[21] Ali Pirasteh, Laura Snyder, Nicholas Boncher, Matthew Passalacqua, David Rosenblum, and J. David Prologo. Cryoablation vs. radiofrequency ablation for small renal masses. *Academic Radiology*, 18:97–100, 1 2011.

[22] Lauren H. Poniatowski, Sneha S. Somani, Domenico Veneziano, Sean McAdams, and Robert M. Sweet. Characterizing and simulating needle insertion forces for percutaneous renal access. *Journal of Endourology*, 30:1049–1055, 10 2016.

[23] Tahir Qayyum, Grenville Oades, Paul Horgan, Michael Aitchison, and Joanne Edwards. The epidemiology and risk factors for renal cancer. *Current Urology*, 6:169–174, 2 2013.

[24] Marc Regier and Felix Chun. Thermal ablation of renal tumors. *Deutsches Ärzteblatt international*, 6 2015.

[25] Hester Scheffer. Interview with dr. h. scheffer, conducted by marlein vogels on 23 february 2023. *Interventional radiology, Amsterdam UMC, The Netherlands*, 2023.

[26] Michael J. Stone, Aradhana M. Venkatesan, Julia Locklin, Peter Pinto, Marston Linehan, and Bradford J. Wood. Radiofrequency ablation of renal tumors. *Techniques in Vascular and Interventional Radiology*, 10:132–139, 6 2007.

[27] Otto Stroosma. Interview with dr. o. stroosma, conducted by marlein vogels on 23 february 2023. *Philips, Urology department*, 2023.

[28] Junichi Tokuda, Laurent Chauvin, Brian Ninni, Takahisa Kato, Franklin King, Kemal Tuncali, and Nobuhiko Hata. Motion compensation for mri-compatible patient-mounted needle guide device: estimation of targeting

accuracy in mri-guided kidney cryoablations. *Physics in Medicine & Biology*, 63:085010, 4 2018. Pubmed.

[29] Robert M. Turner, Todd M. Morgan, and Bruce L. Jacobs. Epidemiology of the small renal mass and the treatment disconnect phenomenon. *Urologic Clinics of North America*, 44:147–154, 5 2017.

[30] Juliet Usher-Smith, Rebecca K. Simmons, Sabrina H. Rossi, and Grant D. Stewart. Current evidence on screening for renal cancer. *Nature Reviews Urology*, 17:637–642, 11 2020.

[31] Marieke van Dommele. Narrative review on image-guided therapy and soft-tissue tracking during percutaneous needle procedures in the abdomen. 2021.

[32] Marieke van Dommele. Towards more continuous feedback on soft tissue anatomy during percutaneous needle placement in the liver. 2023.

[33] Marco van Strijen. Interview with dr. m. van strijen, conducted by marlein vogels on 3 april 2023. *Jeroen Bosch Ziekenhuis, 's Hertogenbosch*, 2023.

[34] Marlein Vogels. Navigation strategies in percutaneous needle procedures in the kidney: A literature review. 2023.

[35] Wendong Wang, Yikai Shi, Andrew A. Goldenberg, Xiaoqing Yuan, Peng Zhang, Lijing He, and Yingjie Zou. Experimental analysis of robot-assisted needle insertion into porcine liver. *Bio-Medical Materials and Engineering*, 26:S375–S380, 8 2015.

[36] Yancheng Wang, Roland K. Chen, Bruce L. Tai, Patrick W. McLaughlin, and Albert J. Shih. Optimal needle design for minimal insertion force and bevel length. *Medical Engineering Physics*, 36:1093–1100, 9 2014.

[37] Lei Zhang, Feng Ju, Yanfei Cao, Yaoyao Wang, and Bai Chen. A tactile sensor for measuring hardness of soft tissue with applications to minimally invasive surgery. *Sensors and Actuators A: Physical*, 266:197–204, 10 2017.

[38] Yi Zhang, Tong wen Ou, Jian guo Jia, Wei Gao, Xin Cui, Jiang tao Wu, and Gang Wang. Novel biologic model for percutaneous renal surgery learning and training in the laboratory. *Urology*, 72:513–516, 9 2008.

[39] Ariana Znaor, Joannie Lortet-Tieulent, Mathieu Laversanne, Ahmedin Jemal, and Freddie Bray. International variations and trends in renal cell carcinoma incidence and mortality. *European Urology*, 67:519–530, 3 2015.

APPENDIX H
MODEL PREPARATION: PHOTO REPORT

In this section, a photo report is provided of the preparation of the kidney models. Please refer to Appendix A for details about the gelatin preparation, tumor preparation, tumor insertion, kidney fixation and marker model construction.

Fig. 31: Preparation fiducial insertion in tumor

Fig. 32: Fiducial insertion in the tumor

Fig. 33: Lateral kidney incisions were made with a scalpel. In total, three lateral incisions were made for three tumor insertions: one in the superior region, one in the middle region and one in the inferior region.

Fig. 34: Tumor insertion.

Fig. 35: The incisions were manually closed.

Fig. 36: The incisions were glued.

Fig. 37: Finished preparation of 6/8 kidneys.

Fig. 38: Preparation of the gelatin base (the perirenal fat)

Fig. 39: The kidneys are positioned on the gelatin base. To simulate the low level of perirenal fat, the low base was prepared (left), to simulate the high level of perirenal fat, the high base was prepared (right).

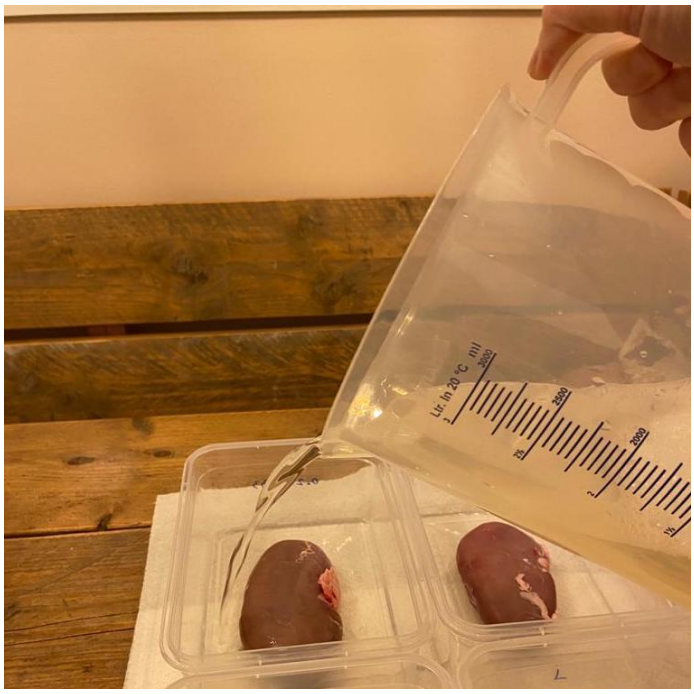

Fig. 40: The additional gelatin to fixate the kidney was cooled below 37°C and poured over the kidney.

Fig. 41: All kidneys were fixated in the gelatin.

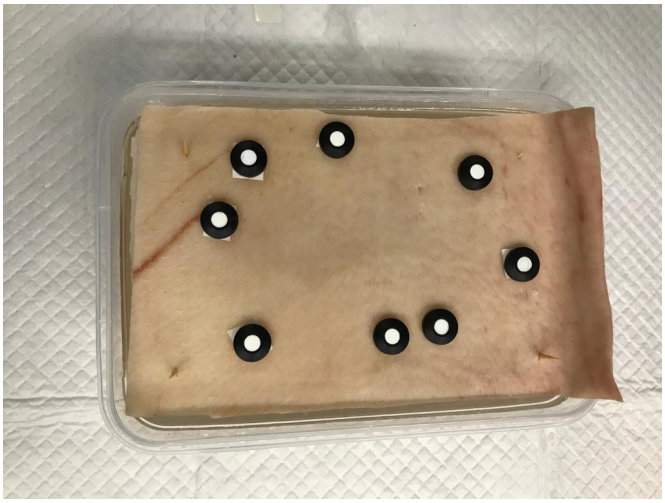

Fig. 42: Per target tumor, a skin marker model was constructed.

Fig. 43: The entire kidney model, including the skin marker model.

APPENDIX I
WORKFLOW: PHOTO REPORT

In this section, a photo report of the workflow of one needle insertion is provided. Although the insertion phases are generally the same for all ECs, lease refer to Appendix A-A for detailed information on the differences per EC.

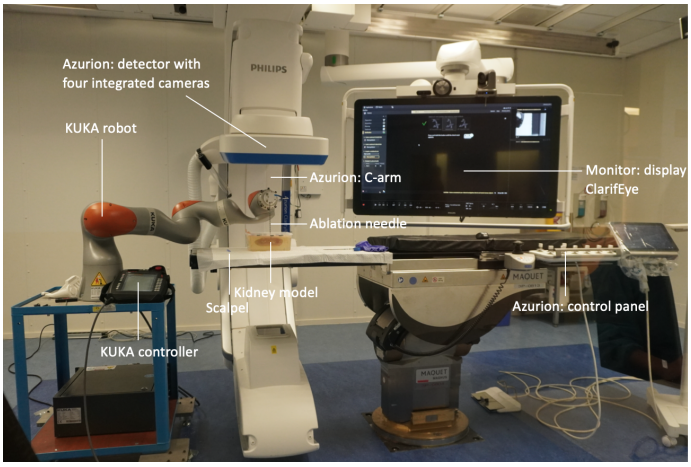

Fig. 44: An overview of the set-up for the research experiment.

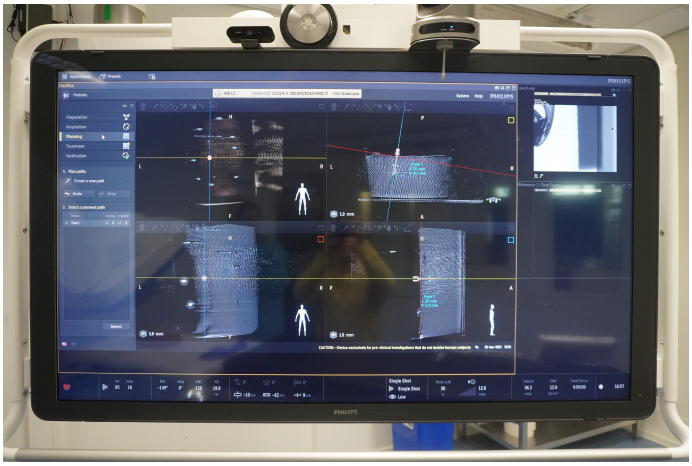

Fig. 45: Planning the needle trajectory in ClarifEye. In Section V-A4, the requirements concerning the planning are provided.

Fig. 46: KUKA was directed to guide the ablation needle to the insertion point.

Fig. 47: According to ClarifEye, the needle tip matches the desired insertion point. However, the orientation does not match the planning yet.

Fig. 48: An incision was made at the insertion point. In Section V-A4, requirements regarding the incision are provided.

Fig. 49: Consequently, the ablation needle is guided by KUKA to match the desired orientation.

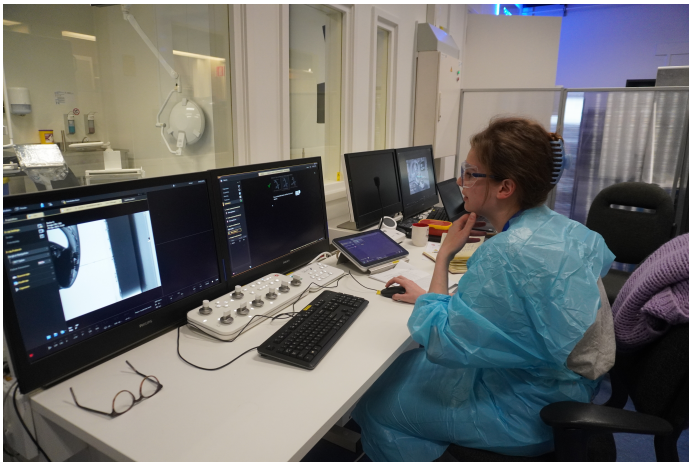

Fig. 50: Before and after insertion, a CBCT-scan is obtained.

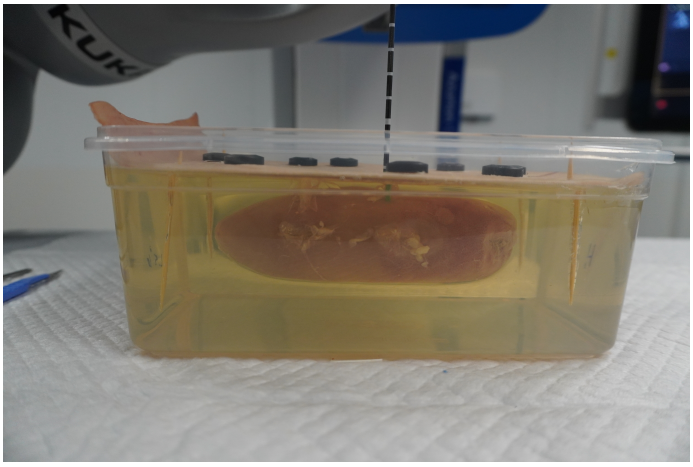

Fig. 52: After insertion image.

Fig. 51: Select the corect insertion program, depending on the appropriate EC, and start insertion